The Dissertation Committee for Han Liu
certifies that this is the approved version of the following dissertation:

Quantification of the Effects of Fracture Properties on Seismic Data

Committee:

Mrinal K. Sen, Co-Supervisor

Kyle T. Spikes, Co-Supervisor

Sergey B. Fomel

Hugh C. Daigle

Nicholas W. Hayman

Quantification of the Effects of Fracture Properties on Seismic Data

by

Han Liu, B.S.; B.S.

DISSERTATION

Presented to the Faculty of the Graduate School of

The University of Texas at Austin

in Partial Fulfillment

of the Requirements

for the Degree of

DOCTOR OF PHILOSOPHY

THE UNIVERSITY OF TEXAS AT AUSTIN

May 2017

Dedicated to my family.

Acknowledgments

I would like to express my most sincere gratitude and appreciation to my supervisors, professor Kyle Spikes and professor Mrinal Sen, without whose support and guidance this work would not have been possible. Their insightful suggestions and great encouragement have been critical during the difficult times in my research and personal life. I am truly grateful for the experience gained during my time in their research groups.

I am grateful to my committee members, professor Sergey Fomel for sharing his deep knowledge in exploration geophysics, professor Hugh Daigle for giving me the most wonderful lectures on formation evaluation, professor Nicholas Hayman for his advice in understanding fractures in geological point of view. I sincerely thank them for serving on my dissertation committee. I would like to thank them for their valuable time, advice, and effort in reviewing my dissertation.

I would like to thank all the faculties whose courses I have taken over my time at the University of Texas at Austin. They have been inspiring and helpful to broaden my knowledge in Geophysics and Petroleum Engineering. These courses will serve as the corner stone of my future researches.

My sincere gratitude goes to our technical staff Tom Hess, who consistently supported me the entire time. Without him, my numerical program could not run correctly. I would like to thank Mark Wiederspahn, especially for his effort in opti-

mizing my research codes. Without his help, the numerical simulations could not have been accomplished in a timely manner. I feel fortunate to have such great research group members for their constant interest and helpful discussions. I would also like to thank Philip Guerrero for his consistent assistance during my entire five years of doctoral program in Jackson School of Geosciences. I would also like to thank the Department of Geological Sciences for providing me a teaching assistantship during my time here. I would like to thank the Texas Advanced Computing Center (TACC) for teaching me parallel computing skills.

I would like to extend my gratitude to my friends and colleagues at UT-Austin: Meijuan Jiang, Russell carter, Qi Ren, Zeyu Zhao, Sarah Coyle, Lauren Becker, Jacqueline Maleski, Chris Linick, Patrick Gustie, Debanjay Datta, Elliot Dahl, Janaki Vamaraju, David Tang, Reetam Biswas, Anthony Barone, Badr Alulaiw, Junzhe Sun, Zhiguang Xue, Yanadet Sripanich.

Quantification of the Effects of Fracture Properties on Seismic Data

Publication No. _____

Han Liu, Ph.D.
The University of Texas at Austin, 2017

Co-Supervisors: Mrinal K. Sen
Kyle T. Spikes

Fractures have significant impact on hydrocarbon production planning and management. Their properties directly determine the well location selection, drilling design and oil/gas productivity. The goal of this research is twofold. The first part is to explore and find an efficient modeling method that can describe fractures explicitly embedded in elastic media under for wave propagation modeling. The second part is to establish correlations between fracture properties and seismic response quantitatively using the modeling results. The results will provide essential information for developing a systematic characterization procedures for fractures.

In the first part, the discontinuous Galerkin method (DG) is first explored for fracture modeling. Within this method, the displacement discontinuity is incorporated by using a jump function included within the shape functions commonly used in the finite element method. A single fracture model is explored using the

DG method. The results are compared with the analytical solutions and found to be in close agreement. From the displacement fields, it is observed that the wave scattering is the main effect of fractures observed in seismic data. However, the expensive computational effort gives rise to challenges in conducting parametric study for several realistic models using DG methods. This poses problems in systematically understanding the effect of fractures on seismic waves.

In the second part, an integral based method is implemented for the parametric studies to investigate the effect of fractures on seismic waves in elastic media. This integral based method ensures accuracy at the nodes of the elements and has greater computational efficiency. Using this algorithm, the effects of fracture spacing, density, and azimuth are investigated in a three-dimensional setting. The scattering index is used to evaluate the extent of wave scattering induced by fractures. The quantitative relationships between fracture spacing, azimuth and scattering index are established. These results provide valuable information for future fracture characterization procedures.

Table of Contents

List of Tables

List of Figures

Chapter 1

Introduction

1.1 Motivation

Subsurface fracture detection has been an active area of research in geophysics during the past 30 years. This is because, first, fractures are the most abundant visible structural features in Earth′s upper crust. Second, precise identification of fracture properties (such as orientations, length, height and filling material) is crucial for new oil/gas reservoir discoveries, oil/gas productivity, well design and risk assessment. Fractures can play an important role in hydrocarbon fluid transportation within the reservoir and heavy drilling mud leakage loss. However, precise identification of fracture properties is extremely challenging due to their complexity and heterogeneity. In this chapter, a few fracture characterization methods will be described briefly and compared. Fractures can be characterized from cores, boreholes, outcrops and seismic data. Fracture investigations of surface outcrops can help to understand the geological processes and evolution history within the whole region, but these studies are also subject to large uncertainty when used as analogs for subsurface formations. Borehole imaging provides a direct description of fractures that intersect the borehole wall but is valid only in the vicinity of the well. Seismic data provides the only way to characterize the spatial variation of fractures in the subsurface but at lower resolution.

We can identify two major trends in the previous work on fracture chatacterization. One involves the development of improved equivalent medium theories for anisotropic homogeneous media, which account for a wider range of properties of fractured rocks and their effects on seismic waves. The other focuses on inversion algorithm development and applications, being applied to invert for fracture parameters from subsurface seismic data. Although several efforts have been made to reveal the mechanisms and principles in fractured reservoir exploration and characterization, many problems still remain unsolved.

The way fractures affect seismic wave propagation depends on the fracture′s geometrical and mechanical properties, such as fracture height, length, orientation, spacing, density, compliance and infill fluid. The conventional seismic fracture characterization methods, such as velocity anisotropy and amplitude variation of offset and azimuth angle (AVOAZ), can only be a proxy for detecting fracture orientation and density. On the other hand, with current technological improvement in seismic acquisition, such as wide-azimuth, full-azimuth, multicomponent, ocean bottom nodes, and in seismic data processing, such as reverse time migration and full waveform inversion, we need better methods that are capable of detecting more fracture properties from seismic data.

Seismic modeling is a procedure to simulate the seismic response from an earth model with given parameters. The objective is to predict seismic responses that a set of sensors would record, given an assumed geological model of the subsurface and the physics included in the wave propagation algorithm. Seismic modeling is an effective way to study the seismic responses of a fracture system and to compare with real data

acquired in the field (such as 3D images of oil and gas reservoirs). Seismic modeling can be used to generate seismic responses in various fractured media which can be used to validate existing fracture inversion schemes. It can be used recursively to evaluate the medium parameters during inversion of real field data.

For general seismic modeling, many approaches are available, which are classified into three categories: direct methods, integration methods, and ray tracing. Carcione et al. (2002) gave a detailed review of these three methods. Integration methods (Cruse and Rizzo, 1968; Carcione et al., 2002) are based on integral representations of the wavefield in terms of waves originating from point sources. These methods are efficient and accurate for specific geometries, such as a bounded object in a homogeneous background. However, they involve high computational cost for complex geometries. Ray tracing methods are based on high frequency asymptotic solutions to the wave equation; therefore, they do not take the complete wavefield into account.

Direct methods solve the wave equation at a finite number of nodes by discretizing the geological model to a numerical mesh. It does not have restrictions on the material variability and can be very accurate when a sufficiently fine grid is used. Direct methods are most commonly used in full wavefield simulation because they are able to handle many complex constitutive equations that cannot be solved by integration methods or ray tracing without simplifying assumptions. However, direct methods are certainly computationally costly than the other two methods.

There are many implementation algorithms of direct methods, such as finite difference (Saenger and Shapiro, 2002), pseudo-spectral (Fornberg, 1998; Vlastos et

al., 2003) and finite element (Lysmer and Drake, 1972) methods. However, very few techniques have been applied to 3D fracture modeling due to various limitations. In 3D cases, high computation more expensive is the main reason.

In 2D seismic modeling, discrete fractures are simulated as finite segments (horizontal, vertical or dipping) with vanishing thickness (Vlastos, 2005; Rao and Wang, 2009), whilst in 3D cases, fractures behave as 3D planes, which makes it possible to characterize individual fractures or fractured media at different azimuths (Xu, 2011). Understanding seismic responses from realistic 3D fracture models would help to extract more useful information from seismic data acquired from fractured targets. Attempting 3D implementation, Willis et al. (2006) and Xu (2011) used finite difference modeling of regularly spaced, discrete vertical fractures systems. However, there are two major problems associated with the finite difference method. The first one is applying the finite difference method to a differential equation involves replacing all derivatives with difference formulas on the mesh. Therefore, when the geometry becomes complicated, a particular mesh scheme is needed to deal with boundary conditions. Another problem is the finite differences are generally implemented using regular grid cells. The regular grid cells give rise to difficulties in incorporating fractures with arbitrary geometries. Staircase approximations introduce artificial diffractions. To avoid this problem, the finite element method is used instead of the finite difference method (DeBasabe et al., 2008). The discontinuous Galerkin finite element method (DGM) overcomes the key disadvantages of finite difference and deals with arbitrary shapes more easily with improved accuracy (Cockburn et al., 2000). However, the finite element method is computationally expensive, especially in 3D cases.

In this work, we implemented a 3D explicit interface scheme with a geometrically irregular mesh following Zhang and Gao (2009). Arbitrarily shaped fractures can be accurately modeled with this discretization. This approach can provide detailed wave propagation phenomena resulting from spatially heterogeneous fractures. The 2D fractures are modeled using discretization with tetrahedral grid cells. Arbitrarily shaped 2D non-planar fractures can then be represented in the numerical mesh.

Throughout this work, we seek a better understanding of scattering from different types of fractures with different geometrical properties from synthetic seismograms generated with an accurate numerical simulation of elastic wave propagation. Scattering effects will be analyzed using transfer functions and a scattering index. The procedure developed for the research lays the foundation for future inversion algorithms to quantify fracture properties.

1.2 Seismic anisotropy in seismic fracture characterization

Anisotropy is variation of a physical property depending on the direction in which it is measured (Sheriff, 2002). Seismic anisotropy, especially, refers to the seismic wave responses varying with propagation angle. The most common seismic responses include velocity and amplitude of seismic waves. The angle refers to the direction including polar or incident angle (offset) and source-receiver azimuth.

Seismic anisotropy may be caused by several factors, such as (1) fine layering of sedimentary rocks, (2) shale lithology, (3) preferred orientations of cracks, fractures or faults, (4) intrinsic preferential alignment of mineral or crystals or grains.

The most popular methods of seismic fracture characterization make uses of azimuthal variation of velocity and amplitude, caused by fracture networks. If major subsurface fractures are mainly aligned vertically, we expect the velocity and amplitude to vary with source-receiver azimuth.

Thomsen (1986) analyzed explicit expressions for velocities in weak anisotropic models. Of all the categories, two types of seismic anisotropy are most common: transverse isotropy with a vertical symmetric axis (VTI), and transverse isotropy with a horizontal symmetric axis (HTI). A fine layered sedimentary sequence in the Earth′s upper crust may cause layer-induced anisotropy, which has the same behavior as that of an equivalent homogeneous VTI medium when the seismic wavelength is larger than the thickness of each sequential fine layer. This concept has been widely used in application of estimating seismic velocity (Backus, 1962).

Small fractures or cracks at the reservoir depth, tend to align in a vertical orientation, causing a fracture induced azimuthal anisotropy (Champin, 1981, 1983, and 1985). As a result, the periodic azimuthal variation of seismic attributes, such as NMO velocity, traveltime, reflected wave amplitude, attenuation and scattering. can all be used to describe certain fracture properties.

1.2.1 Velocity/traveltime method

Normal moveout correction (NMO) is a basic seismic data processing step that corrects for the offset (source-receiver distance) dependent effect by stretching travel time variation in all seismograms to align with the zero-offset trace. For a constant

velocity medium and a flat reflector, the NMO equation is given by,

$$t^2 = t_0^2 + \frac{x^2}{v^2}, \tag{1.1}$$

where t_0 is two way traveltime at zero-offset, x is offset, v is NMO velocity.

Based on the moveout analysis, Grechka and Tsvankin (1998) and Grechka et al. (1999) showed that the azimuthal variation in the P wave NMO velocity for arbitrary anisotropic and heterogeneous media can be generally described as an ellipse in the horizontal plane. Li (1999) and Wang and Li (2006) further proved that, in anisotropic media, the P wave normal moveout (NMO) equation can be generally written in following form:

$$t^2(\phi, x) = t_0^2 + x^2((\frac{cos(\phi - \phi_0)}{V_{fast}})^2 + (\frac{sin(\phi - \phi_0)}{V_{slow}})^2), \tag{1.2}$$

where t_0 is zero-offset two way traveltime, x is the offset (source-receiver distance), ϕ is the source receiver azimuth, ϕ_0 is the azimuth of the major axis of the NMO velocity ellipse, V_{fast} is the fastest NMO velocity and V_{slow} is the slowest NMO velocity.

The seismic response of vertically aligned fractured media behave the same as in a homogeneous HTI medium. This concept can be used to approximately link the fast NMO velocity direction in an HTI medium to the fracture strike orientation, while the slow NMO velocity direction in HTI medium points to the fracture normal direction. The fracture density, under the HTI medium concept, is related to the degree of anisotropy, which is the ratio between the fast velocity and slow velocity.

1.2.2 Amplitude method

The angle-dependent reflection coefficient from an interface contains valuable information on the local properties of the layers in an isotropic medium (Shuey, 1985). Therefore, an Amplitude Versus Offset (AVO) analysis is commonly used in seismic reservoir characterization. The amplitudes are also influenced by the elastic properties averaged on the scale of a seismic wavelength. In isotropic media, the P wave reflection coefficient R as a function of incidence angle θ is approximated as

$$R(\theta) \approx A + Bsin^2\theta + Csin^2\theta tan^2\theta, \tag{1.3}$$

where A, B, C are AVO intercept, gradient, and curvature, respectively, and they are related to the velocities and densities of the two sides of the interface. For small incidence angles, we may ignore the third term in equation 1.3. The small angle P wave reflection coefficient can then be expressed as

$$R(\theta) \approx A + Bsin^2\theta. \tag{1.4}$$

The AVO analysis measures local properties on the interface between two half spaces. In anisotropic media, amplitude variations are observed not only as a function of incidence angle but also as a function of source receiver azimuth. These observations are used in AVOAZ analysis. For AVOAZ, the AVO parameters B and C are functions of velocities and densities of the two sides of the interface, as well as azimuth. The two-term P wave reflection coefficient can by approximated by

$$R(\theta, \phi) \approx A + B(\phi)sin^2\theta. \tag{1.5}$$

where ϕ refers to azimuth. The AVO gradient $B(\phi)$ can, in general, be written as $B(\phi) = B_0 + B_1 cos^2(\phi - \phi_0)$, where B_0 is the conventional AVO gradient in isotropic media, B_1 is the anisotropic AVO gradient, and ϕ_0 is the angle between the chosen zero-azimuth direction and the symmetry axis plane. An AVO analysis on the interface of an equivalent fracture-induced anisotrpic medium (HTI medium) normally displays an elliptical variation with azimuth, which can also be used to determine the fracture strike orientation and fracture density (R$\ddot{u}$ger, 1997; Xia et al., 2006; Varela et al., 2007). It is worth noting that there exist a 90° ambiguity in determining fracture orientation. For a class I AVO, such as a shale formation above a fractured reservoir, the trough in equation of $B(\phi)$ corresponds to the fracture parallel orientation, while the peak corresponds to the fracture normal orientation. On the contrary, for a class III AVO, such as a fractured reservoir above the shale formation, the peak corresponds to the fracture parallel orientation and the trough corresponds to the fracture normal orientation. However, this 90° ambiguity does not exist in the aforementioned velocity/traveltime method. Therefore, R$\ddot{u}$ger (2002) and Holmes and Thomsen (2002) suggested that combined AVOAZ and azimuthal NMO velocity or interval traveltimes should resolve this ambiguity. Hall and Kendall (2003) suggested that synthetic AVO modeling may resolve this ambiguity.

1.2.3 Fracture scales and seismic resolution

There is an assumption used in the current NMO velocity/traveltime and AVOAZ methods that the fracture media is equivalent to an anisotropic medium. Indeed, seismic anisotropy provides an opportunity to extract fracture properties that

are below seismic resolution. There is another concept to consider when defining a geophysical model-heterogeneity, which is closely related to anisotropy. A medium is anisotropic if a property measured at the same location varies with orientation. A medium is heterogeneous if a property measured along one direction varies with location (Winterstein, 1990). A heterogeneous material can be treated as a homogeneous, anisotropic or not, material when the wavelength of the seismic wave propagating through it is much larger than the scale of heterogeneity. For example, a model consisting of many thin horizontal homogeneous layers with varying properties, is heterogeneous when the wavelength is comparable or smaller than the thickness; however, it may be considered homogeneous and anisotropic when the wavelength is much larger than the thickness.

Similarly, whether a seismic wave "sees" a fractured medium and a seismic wave "sees" a fractured medium depends on the scale of fractures and the seismic wavelength. If the scale of fracture that we would like to detect is a large scale fault, it can show up as an abrupt lateral discontinuity on seismic gathers. If the fractures of interest are those in a shale formation, which are smaller than a seismic wavelength and aligned in specific orientations, we can treat the overall population of the fractures in a reservoir as an equivalent homogeneous and anisotropic medium. Methods with homogeneous and anisotropic synthetic modeling, NMO velocity/traveltime, AVOAZ are commonly used in fracture characterization for this scale. However, the technique for discrete fracture detection with scales comparable to the seismic wavelength are still under-development.

1.3 Review of simulation algorithms of elastic wave propagation in fractured media

Studying seismic wave propagation in fractured media has been of great interest in seismology and exploration geophysics. Simulation in 3D is necessary for comprehensive understanding of azimuth-dependent seismic wave propagation across fractures. When the fracture size and spacing are substantially smaller than the seismic wavelength, wave propagation in such fractured media can be described in terms of an equivalent anisotropic medium. Various equivalent medium theories (e.g., Hudson 1980, 1981; Schoenberg 1980; Thomsen 1995; Liu et al. 2000) are available for estimating the parameters of physical fracture properties. However, fracture swarms with varying fracture parameters cannot be represented by any equivalent medium theory. This is because the equivalent medium theories consider the general effects of all the small fractures. Therefore, in order to obtain detailed seismic characteristics, fractures should be modeled as local inclusions.

Numerical schemes that treat the fractures as discrete localizations have been developed. Examples of these include (1) local effective-medium scheme, (2) weak-inclusion scheme, (3) and explicit-interface scheme. The local effective-medium scheme (Coates and Schoenberg, 1995; Vlastos et al., 2003) expresses the effective compliance of a fractured layer with the sum of compliances from each fracture and the host rock (background medium) within each discretized cell. This results in a local fractured medium that has a smaller velocity than the background medium. Thus, small grid spacing and time-sampling intervals are required (Zhu and Snieder, 2003) to satisfy the stability condition. The weak-inclusion scheme (Saenger and Bohlen, 2004)

describes fractures/cracks as low-velocity and low-density ellipsoidal inclusions. However, this scheme requires much smaller grid spacing than the local effective-medium scheme in order to adequately model the thickness of cracks. The explicit schemes directly treat fractures as displacement discontinuities using the linear slip model (Schoenberg and Douma, 1988; Slawinski and Krebes, 2002; Zhu and Snieder, 2003). In this scheme, fractures are non-welded interfaces with vanishing widths. Therefore, no low-velocity medium or small-size grid spacing is introduced. This significantly reduces the computational cost and memory requirements, especially in 3D simulation compared to the local effective medium scheme and weak inclusion scheme.

1.3.1 Linear Slip Model

In accordance with the linear slip model of Schoenberg (1980), fractures are considered as interfaces with negligible mass and thickness relative to the seismic wavelength. With the linear slip model, we can simulate seismic wave behavior across an unwelded contact or slip interface, representing a fracture. Across a slip interface the particle displacement is considered to be discontinuous whereas the stress field is continuous, and the discontinuity is assumed to be linearly related to the local stress traction by the fracture compliance:

$$\Delta u = \eta t_n, \tag{1.6}$$

where Δu is the jump of the displacement field at the discontinuous fracture interface, and t is the traction vector at the fracture interface, t_n=$\{T_1, T_2, T_3\}^T$ with T_3 pointing in the downward verical direction, η is the fracture compliance matrix, given by

Schoenberg and Sayers (1995) as,

$$\eta_{ij} = \eta_N n_i n_j + n_T(\delta_{ij} - n_i n_j), \tag{1.7}$$

where η_N and η_T are the normal and tangential compliances respectively, n is the component of a vector normal to the fracture, and δ_{ij} is the Kronecker delta. For a rotationally invariant fracture normal to the x_2 axis, the fracture compliance matrix is diagonal and is given by (Schoenberg, 1980)

$$\eta = \begin{bmatrix} \eta_T & 0 & 0 \\ 0 & \eta_T & 0 \\ 0 & 0 & \eta_N \end{bmatrix}. \tag{1.8}$$

The linear slip model has been validated by experiments reported in Hsu and Schoenberg (1993). It describes the applicability of the linear slip assumption in modeling long and small wavelengths.

The Δu in Equation 1.3 denotes the jump of the displacement vector across an interface in a Cartesian coordinate system (x_1, x_2, x_3) with the x_3-axis pointing vertically downward. If a fracture has an arbitrary geometry, then the x_3-axis is not consistent with the downward vertical direction. Accordingly, the linear slip model in Equation 1.3 can be expressed as

$$T\Delta u = \eta t_n, \tag{1.9}$$

where T denotes the transform matrix for the Cartesian system (x_1, x_2, x_3) to a system that has one axis pointing to the normal n direction. For a fracture with horizontal

symmetry and rotational symmetry about the normal, η is diagonal and characterized in terms of η_N and η_T (Haugen and Schoenberg, 2000). The matrix T can be expressed using directional cosines of the normal vecter n as:

$$T = \begin{bmatrix} \frac{n_3 n_1}{\sqrt{n_1^2+n_2^2}} & \frac{n_3 n_2}{\sqrt{n_1^2+n_2^2}} & -\sqrt{n_1^2+n_2^2} \\ -\frac{n_2}{\sqrt{n_1^2+n_2^2}} & -\frac{n_1}{\sqrt{n_1^2+n_2^2}} & 0 \\ n_1 & n_2 & n_3 \end{bmatrix}, \tag{1.10}$$

1.3.2 Modeling of Linear Slip Model with finite difference

The procedure for implementing the linear slip model with a finite difference algorithm is to model the seismic response of single or multiple fractures or faults was proposed by Coates and Schoenberg (1995). They assume a horizontal fracture with a length of Δl enclosed in a 2D cell with an area of ΔA. Based on the group theory mentioned in Schoenberg and Muir (1989), when fracture thickness is close to zero, the effective compliance for the cell surrounding the fracture S is

$$S = S_b + S_f = S_b + \frac{\Delta l}{\Delta A} \begin{bmatrix} 0 & 0 & 0 \\ 0 & 0 & 0 \\ 1 & 0 & 0 \\ 0 & 1 & 0 \\ 0 & 0 & 1 \\ 0 & 0 & 0 \end{bmatrix} \underline{Z} \begin{bmatrix} 0 & 0 & 1 & 0 & 0 & 0 \\ 0 & 0 & 0 & 1 & 0 & 0 \\ 0 & 0 & 0 & 0 & 1 & 0 \end{bmatrix}, \tag{1.11}$$

where S_b is the compliance matrix for the unfractured background medium, S_f is the fracture compliance matrix. The S matrix is a 6x6 matrix. The inverse of the overall effective compliance matrix S is the stiffness matrix that can be used for a finite difference algorithm. In this case, the thickness of the fracture at least equals the

size of the unit grid. The fracture thickness used in Willis et al. (2006) is 5 meters, and 10 meters by Xu (2011). These are much larger than realistic fracture thickness. This is caused by the nature of the finite differences that computes the derivatives of displacement using the differences among surrounding unit grids. Therefore, the explicit displacement discontinuity across the slip interface cannot be resolved. Instead, the inverse of the local effective compliance matrix is needed for a finite difference algorithm to treat a discrete fracture.

1.4 Objectives

Fracture reservoir characterization becomes more and more challenging and difficult as we march into unknown frontiers. Comprehensive understanding and new technology applications have proved to indispensable for new discoveries and successful production. Among the technologies we heavily rely on, seismic inversion is indisputably a critical constituent that we must advance with the best of our efforts. One vital step of a successful seismic inversion relies on our profound understanding of wave propagation in the Earth and, therefore, an accurate and efficient wave propagation method is the key. In this dissertation, I will show two forward modeling algorithms for wave propagation in fractured media. One is a finite element based Discontinuous Galerkin method, the other one is a finite element based integral method. I will further explain their advantages in the following chapters. The main objective of this dissertation is to assess the effects of fracture properties on seismic wave propagation and to build relationship between fracture properties and seismic data for inversion purposes.

In Chapter 1, I review the literature on popular fracture characterization methods. Based on the review, it is clear that the existing methods can only be used as a proxy for detecting fracture orientation and fracture density distributions. The commonly used equivalent medium theories are not applicable in heterogeneous fractured media. More detailed fracture properties that we are interested in, require a novel approach to characterize. I then justify the importance of forward modeling in understanding the basic principles of wave propagation and a powerful tool to tackle the challenging inverse problems we are facing. The review of current popular numerical modeling algorithms on simulating fractures reveals that the finite element method is more flexible and efficient for simulating complex fracture geometries. I provide detail descriptions of special configurations of the finite element method, Discontinuous Galerkin method and integral method in Chapters 2 and 3.

In Chapter 2, I first introduce the finite element based Discontinuous Galerkin (DG) method for seismic modeling, including DG formulation of elastic wave equation and the advantages of DG on simulation of displacement discontinuity. For a simple plane wave propagation across a horizontal fracture, the analytical solutions for reflection and transmission coefficients are available. I then compare the 2D DG numerical solutions to the analytical solutions. I use a series of fracture compliance values to compare the amplitude and phase of reflected and transmitted signals. However, applying DG in 3D requires high memory cost because of large number of degree of freedoms required in DG algorithm.

In Chapter 3, I first introduce the integral formulations, linear slip model and numerical implementation of the integral method. I describe the implementation

of point source and explosive source in the integral method. I perform the model validation and report a few case studies on different fracture properties. The results show different scattering patterns for different fracture geometries.

In Chapter 4, I focus on studying the effect of fracture properties on wave scattering. I introduce the scattering index method as a way of quantifying the extent of scattering. To study the effect of fracture spacing, density and height, I keep the incident angle constant and study the effect of fracture properties on the scattering index. I also investigate the effect of incident angles on different types of fractures including a single fracture, multiple parallel aligned fractures, single intersecting fracture, and multiple intersecting fractures. The effect of incidence angle is evaluated using the scattering index. l correlate the fracture properties and incident angles with the scattering index to provide sufficient information for future inversion research.

In Chapter 5, I summarize this dissertation and discuss future research directions.

1.5 Contributions

The main contributions of this dissertation are summarized as follows:

- I investigated the effect of fractures on seismic wave scattering using the Discontinuous Galerkin method. DG can achieve a much higher accuracy in simulating displacement field discontinuity in an elastic medium with a high computational cost due to the high degree of freedom. (Chapter 2)
- I implemented the integral based method in 3D to explicitly simulate elas-

tic wave propagation in fracture media. The integral method can achieve high accuracy and much lower computational cost than DG. The code is written using C language and parallelized using MPI (Message Passing Interface). The numerical mesh is assembled by tetrahedral elements. Discrete fractures can be modeled on any facet of the tetrahedral element. I explicitly model the displacement discontinuity across a fracture using a pair of nodes assigned at the position along the fracture interface. (Chapter 3)

- I investigated the effect of fracture properties, including fracture spacing, densities, and height variations, on seismic wave propagation in elastic media. The analyses cover shot gather results for both azimuthal variation and lateral variation. (Chapter 3 and 4)

- I investigated the effect of both azimuth and source to fracture center azimuth of four types of fractures, including single fracture, multiple parallel aligned fractures, single intersecting fracture, and multiple intersecting fractures. (Chapter 4)

- I applied scattering index methods to quantify the effect of fracture properties on seismic wave scattering. This may contribute to better understanding of fracture-induced scattering. (Chapter 4)

- I provided an insight in the correlation between fractures and seismic wave scattering, which, in turn, lays the foundation for future inversion algo-

rithm to quantify fracture properties from real surface seismic data. (Chapter 4)

Chapter 2

Application of DGM in simulating elastic wave propagation in fractured media

2.1 Introduction

Seismic modeling is a procedure to simulate the seismic response from an earth model with given parameters. It can be used recursively to evaluate the medium parameters during inversion of real field data. I perform numerical simulations of elastic wave propagation in models with realistic fractures using the discontinuous Galerkin method (DGM). Compared to finite difference methods, the main advantages of DGM are its flexibility to handle discontinuities and complicated geometries in fractured reservoir models. It also involves an extremely simple treatment of the boundary conditions to achieve high-order accuracy. Therefore, DGM is particularly well suited to incorporate fractures because these are simulated as discontinuities in the displacement field (De Basabe et al., 2011, 2016). A practical representation of a discrete fracture is the fracture corridors (Singh et al., 2008). The linear slip model, also called the discrete fracture model, represents the fracture by assuming the displacements caused by a seismic wave are discontinuous while the tractions remain continuous. Coates and Schoenberg (1995) introduced the linear slip model in a finite difference algorithm.

In this chapter, I validate the 1D linear slip condition by comparing phase shift and amplitude of reflection and transmission waveforms between DG numerical results and the analytical solution. Because DG is a numerical method, its accuracy is highly dependent on mesh size in this simulation. One can keep decreasing the size of the element to approach the analytical solution; however, it may not be computationally efficient. Therefore, one needs to validate the DG method in solving the wave equation by comparing it with an analytical solution when certain accuracy has been achieved in the one-dimensional problem, it can be assumed to be accurate within the same level of tolerance in higher dimensional problems (such as 2D and 3D). Following this, I perform 3D elastic wave propagation in a one-layer model with a set of vertical aligned fractures, and I analyze the effects of multiple slip conditions to represent a fracture network in three dimensions. I also simulate wave propagation in a three-layer model with a set of vertical aligned fractures inserted in the middle layer and analyze the reflection response of the fractured layer.

2.1.1 DG formulation of the elastic wave propagation

The elastic wave equation describes the propagation of compressional and shear waves. The elastic form of the wave equation is an accurate approximation to the propagation of waves in the earth. However, it is also difficult to solve and is computationally expensive because it needs to be solved for the displacement, which is a vector field. Different versions of the elastic wave equation exist for isotropic, anisotropic, homogeneous, and heterogeneous media.

Wave propagation phenomena are modeled by the equation of motion, which

is given by

$$\rho\partial_{tt}u_i = \partial_i\sigma ij + f_i \quad in \quad \Omega \times (0,T) \quad i,j = 1,...,d, \tag{2.1}$$

where d is the number of physical dimensions (2 or 3), $\Omega \subset \mathbb{R}^d$ is the physical domain, $(0,t)$ is the time domain, u_i is the displacement vector, σ_{ij} is the stress tensor, and the source is described by the force vector f_i. The stress tensor can be written as a function of the displacement using the generalized Hooke′s Law, also known as the stress-strain relation. In an elastic medium, the stress (σ) is linearly related to the strain (ε) and the stiffness tensor (C_{ijkl}):

$$\sigma_{ij}(\boldsymbol{u}) = C_{ijkl}\varepsilon_{kl}. \tag{2.2}$$

The elastic wave equation in an isotropic heterogeneous medium is obtained by substituting Hooke′s Law in the equation of motion and is given by

$$\rho\partial_{tt}u_i - \partial_i\lambda\partial_j u_j - \partial_j\mu(\partial_j u_i + \partial_i u_j) = f_i \quad in \quad \Omega. \tag{2.3}$$

However, using elastic theory to study seismic waves cannot fully explain all the physical mechanisms during wave propagation, e.g., attenuation. In real seismic data, seismic waves attenuate when they propagate through the Earth. The fluctuating stresses in a rock caused by a passing seismic wave can induce global flow of filled fluid in the rock (Biots mechanism) or local flow between connected pores (squirt flow) (Mavko et al., 2009). Patchy saturation may also dissipate energy due to a

passing wave when part of the energy leads to oscillatory liquid cross-flow between fully liquid-saturated patches and the surrounding rock with gas. The attenuation effects are not included in this research.

The discontinuous Galerkin finite element method (DGM) provides a numerical solution to simulate elastic wave propagation in models with fractures (De Basabe et al., 2011). The DGM considers a subdivision of Ω, $\Omega_h = E_1, E_2, ..., E_{Nh}$, where E_i is an element partitioned in the discretized mesh. In a finite element partition of the domain Ω_h, Γ_h denotes the set of all the faces between the elements in Ω_h. The weak form of the elastic wave equation is obtained by multiplying a test function v, summing over an arbitrary element E_i and using the Gauss divergence theorem. The weak form is given as (De Basabe et al., 2008; De Basabe and Sen, 2009; 2010)

$$\sum_{E\in\Omega_h} (\rho\partial_{tt}\boldsymbol{u},\boldsymbol{v})_E + \sum_{E\in\Omega_h} B_E(\boldsymbol{u},\boldsymbol{v}) + \sum_{\gamma\in\Gamma_h} J_\gamma(\boldsymbol{u},\boldsymbol{v};S,R) = \sum_{E\in\Omega_h} (\boldsymbol{f},\boldsymbol{v})_E, \tag{2.4}$$

where $\boldsymbol{u} \in \boldsymbol{X}^D = \{\varphi | \varphi \in \boldsymbol{H}^1(E) \quad \forall \quad E \in \Omega_h, \varphi = 0 \quad on \quad \Gamma_D\}$, such that for vector test function $\boldsymbol{v} \in \boldsymbol{X}^D$,

$$(u,v)_E = \int_E \boldsymbol{u}\cdot\boldsymbol{v}dxdz, \tag{2.5}$$

$$B_E(u,v) = \int_E \left(\lambda \bigtriangledown\cdot u \bigtriangledown\cdot v + \mu(\bigtriangledown u + \bigtriangledown u^T) : \bigtriangledown v\right) dxdz, \tag{2.6}$$

$$J_\gamma(\boldsymbol{u},\boldsymbol{v};S,R) = -\int_\gamma \{\tau_i(\boldsymbol{u})\}\,[v_i]\,d\gamma + S\int_\gamma \{\tau_i(\boldsymbol{v})\}\,[u_i]\,d\gamma + R\int_\gamma \{\lambda+2\mu\}\,[\boldsymbol{u}]\cdot[\boldsymbol{v}]\,d\gamma, \tag{2.7}$$

and τ_i is the traction vector, given in the isotropic case by

$$\tau_i(u) = \sigma_{ij}(u)n_j = \lambda u_{k,k}n_i + \mu(u_{i,j}+u_{j,i})n_j, \tag{2.8}$$

and n_j is a unit vector normal to the element edge γ. Let γ be the edge between element E_1 and E_2, then the average of a vector function $\boldsymbol{u}$ on can be expressed as

$$\{\boldsymbol{u}\} = \frac{1}{2}\left(\boldsymbol{u}|E_1 + \boldsymbol{u}|E_2\right). \tag{2.9}$$

The jump function can be expressed as

$$[\boldsymbol{u}] = \boldsymbol{u}|E_1 + \boldsymbol{u}|E_2. \tag{2.10}$$

The weak form of the wave equation is called weak because the solution is no longer required to have second order derivatives, so only first order space derivatives appear (De Basabe and Sen, 2009). The weak form indicates that the integrals are only performed element wise. In the DGM, each element in the physical domain is mapped into a master element coordinate with interval [-1, 1] (Carcione et al., 2002). The nodal basis function defines the master element by a set of Legendre polynomials on [-1, 1]. The basis function determines the interpolation over a set of nodes inside a given interval.

For a rotationally invariant fracture normal to x_2 axis, the fracture compliance matrix is diagonal and is given in Equation 1.8. In order to properly simulate the discontinuity, it is assumed that fractures are located at the element interface in the discretized mesh. Therefore, the additional linear slip model boundary condition can be imposed at the element-wise surface integral J_γ^f term. The weak form of the wave equation including a fracture represented by the linear slip model is:

$$\sum_{E\in\Omega_h}\left((\rho\partial_{tt}\boldsymbol{u},\boldsymbol{v})_E + B_E(\boldsymbol{u},\boldsymbol{v})\right) + \sum_{\gamma\in\Gamma_c} J_\gamma^c(\boldsymbol{u},\boldsymbol{v}) + \sum_{\gamma\in\Gamma_f} J_\gamma^f(\boldsymbol{u},\boldsymbol{v}) = \sum_{E\in\Omega_h}(\boldsymbol{f},\boldsymbol{v})_E, \quad (2.11)$$

where

$$J_\gamma^f(\boldsymbol{u},\boldsymbol{v}) = \int_\gamma Z_{ij}^{-1}\,[u_j]\,[v_i]\,d\gamma, \quad (2.12)$$

Z represents the previously mentioned fracture compliance matrix, which includes the normal and tangential compliances for a rotationally invariant fracture.

2.1.2 Advantages of DG on simulating displacement discontinuity

In DG, the integrals are performed element-wise on the Gauss-Lobatto-Legendre (GLL) element with shape functions. The shape functions include a series of Legendre polynomials that are a set of orthogonal functions on $[-1, 1]$. The nonuniform distribution of integration points within a GLL element provides an accurate solution at each discretized grid. Figure 2.1 shows schematic of simple mesh. The left element and right element have a shared boundary. Let us assume the fracture is placed on the shared boundary. In DG, the left element and right element do not share the degree of freedom, which means they can have different values. This satisfies the

element discontinuity at the fracture interface. The reason for this comes from when using divergence theorem where the surface integral of the weak equation is equal to zero, which satisfying the element continuity for CG (Figure 2.2). For DG, the surface integral is not equal to zero (Figure 2.2), and this term gives us the jump function shown in Equation 2.10 to handle the element discontinuity at the fracture interface. Both the non uniform distribution of integration points with GLL elements and discontinuity across element boundary are the key advantages for using DG on simulation of displacement discontinuity.

2.2 Model validation and calibration in 2D

The analytical solution of the linear slip condition for a single fracture inserted into a medium is derived by Schoenberg (1980). The fracture cuts the entire medium into medium 1 and medium 2. I assume all displacements of coupled P-SV waves lie in the (x_1, x_2) plane. The incident P wave field in medium 1 is

$$\begin{bmatrix} u_1 \\ u_2 \end{bmatrix} = \begin{bmatrix} sin\theta_1 \\ cos\theta_1 \end{bmatrix} e^{iwx_2 cos\theta_1/\alpha_1}. \tag{2.13}$$

The reflected field in medium 1 is

$$\begin{bmatrix} u_1 \\ u_2 \end{bmatrix} = R_P \begin{bmatrix} sin\theta_1 \\ -cos\theta_1 \end{bmatrix} e^{-iwx_2 cos\theta_1/\alpha_1} + R_S \begin{bmatrix} cos\phi_1 \\ sin\phi_1 \end{bmatrix} e^{-iwx_2 cos\phi_1/\beta_1} \tag{2.14}$$

and the transmitted field in medium 2 is

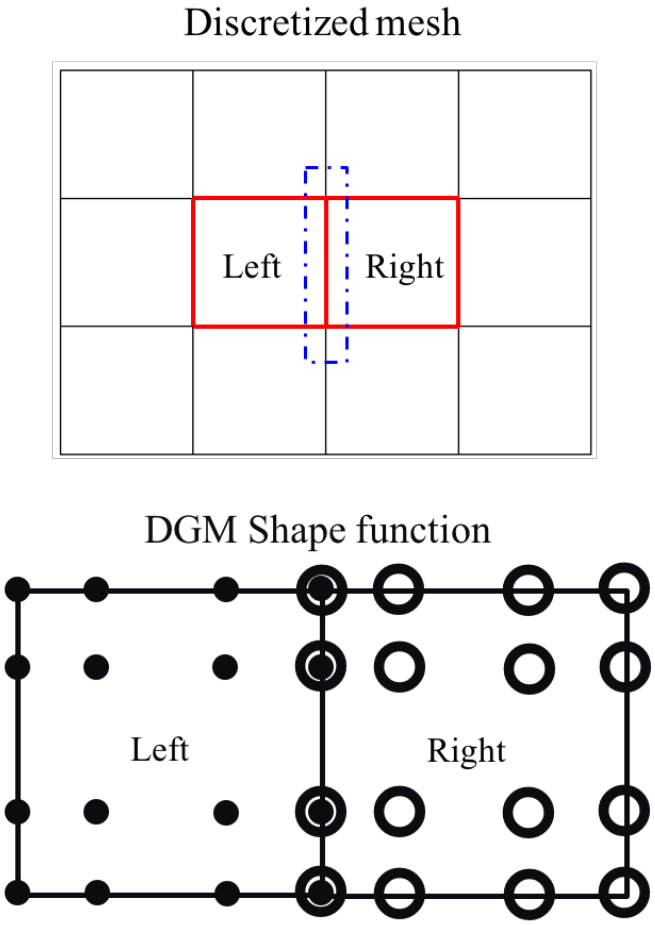

Figure 2.1: Schematic of an simple mesh with third order Gauss-Lobatto-Legendre (GLL) element. The left element and right element have a shared boundary. The non-uniform distribution of integration points within both left and right GLL element.

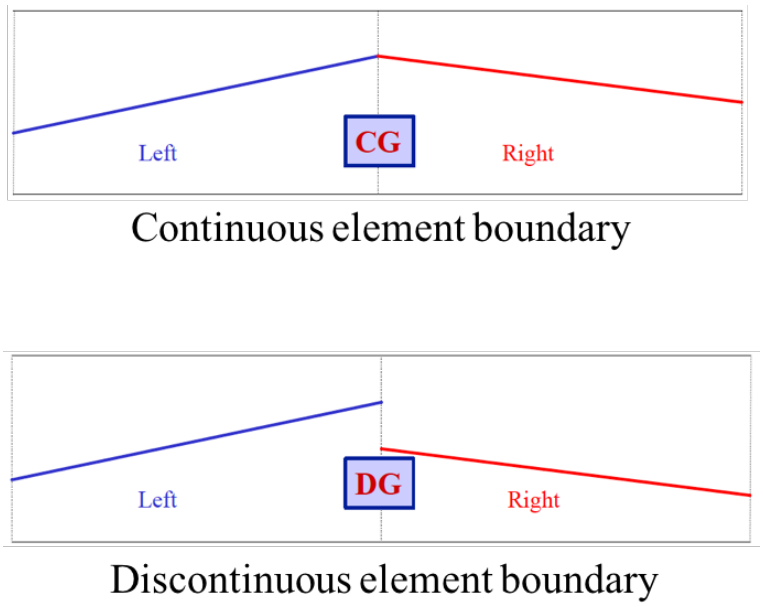

Figure 2.2: Schematic of element boundaries for the Continuous Galerkin method and Discontinuous Galerkin method. Across the element boundary, the values are continuous for the Continuous Galerkin while discontinuous for the Discontinuous Galerkin method.

$$\begin{bmatrix} u_1 \\ u_2 \end{bmatrix} = T_P \begin{bmatrix} sin\theta_2 \\ cos\theta_2 \end{bmatrix} e^{iwx_2 cos\theta_2/\alpha_2} + R_S \begin{bmatrix} -cos\phi_2 \\ sin\phi_2 \end{bmatrix} e^{-iwx_2 cos\phi_2/\beta_2}, \tag{2.15}$$

where R_P, R_S, T_P, T_S denote the reflection and transmission coefficients of P and SV waves; θ and ϕ represent the angles of P and SV waves and their subscripts 1, 2 indicate the medium 1 and 2. α, β, and ρ denote compressional wave velocity, shear wave velocity and density. Equations (2.14) and (2.15) show that the displacements at the fracture interface between medium 1 and 2 are different. However, the stresses τ_{22} and τ_{21} are continuous across the interface and are given by

$$\tau_{22} = \rho \left[\alpha^2 \left(\frac{\partial u_1}{\partial x_1} + \frac{\partial u_2}{\partial x_2} \right) - 2\beta^2 \frac{\partial u_1}{\partial x_1} \right], \tag{2.16}$$

$$\tau_{21} = \rho\beta^2 \left(\frac{\partial u_1}{\partial x_2} + \frac{\partial u_2}{\partial x_1} \right). \tag{2.17}$$

With the linear slip boundary condition, the reflection and transmission coefficients can be expressed as

$$R = -\frac{Z_1 - Z_2 - iw\eta Z_1 Z_2}{Z_1 + Z_2 - iw\eta Z_1 Z_2}, \tag{2.18}$$

$$T = -\frac{2Z_1}{Z_1 + Z_2 - iw\eta Z_1 Z_2}, \tag{2.19}$$

where $Z_i = \rho_i \alpha_i$ and $\eta = \eta_N$ for a normal incidence compressional wave.

To examine the effect of DGM on modeling the seismic response of fractures, validation of reflection and transmission coefficients across the linear slip boundary

condition is necessary. I simulate a wave field in a homogeneous, isotropic, linear elastic space containing a single horizontal fracture denoted by $x_2 = 1km$. The elastic medium, with density $2200g/cm^3$, compressional wave velocity $3000m/s$, and shear wave velocity $1765m/s$, occupies the entire region. The normal and tangential compliances for the single fracture are both $1.8 \times 10^{-9} m/Pa$. The normal incidence compressional wave propagates towards the fracture. The 2D wave fields are shown in Figure 2.3a, 2.3b. The dashed lines denote the fracture location.

A receiver was placed $200m$ above and one at $200m$ below the fracture at $x = 1000m$. Figure 2.4a shows the waveforms extracted from the receiver above the fracture. The first waveform indicates the incident wave, and the second waveform indicates the reflected waveform. Figure 2.4b shows the transmitted waveform extracted from the receiver below the fracture.

I convolved the incident wave with the analytical reflection and transmission coefficients calculated from Equations 2.18 and 2.19. The convolved reflection response and the DG simulated reflection response are shown in Figure 2.5a. The convolved transmission response and the DG simulated response are shown in Figure 2.5b. The DG numerical response is consistent with the analytical responses on phase and amplitude. The inconsistent response of the DG result in the left side of Figure 2.5a comes from the incident wave. However, the analytical result shows the reflection response only and shows zero amplitude elsewhere. On the other hand, the discretization achieved by DG yields progressively more accurate solutions as the mesh size becomes finer. Therefore a perfect match of the DG solution and analytical solution can be obtained by decreasing the element size. I reduce the element size by

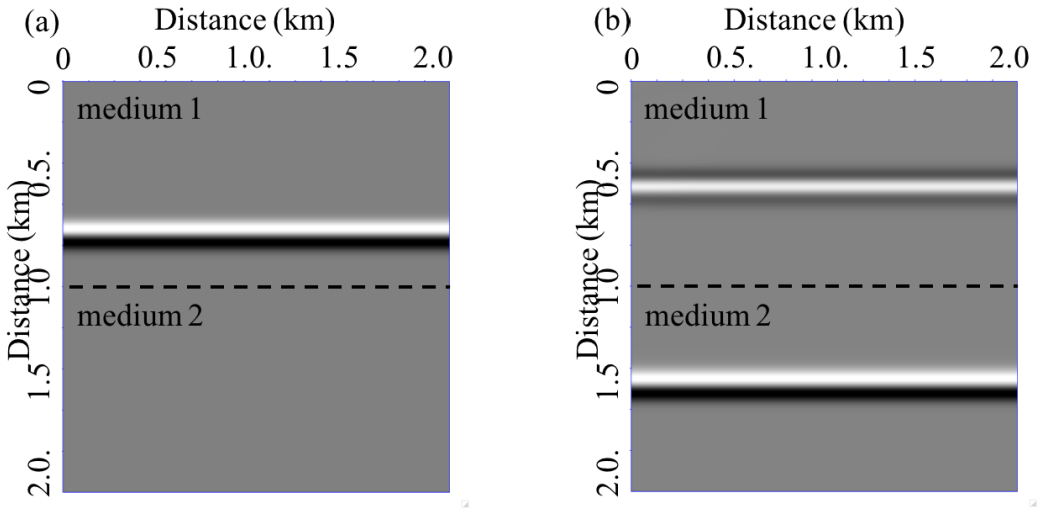

Figure 2.3: a). Normal Incident compressional wave field. b). Reflection and transmission wave field across the fracture. The dashed line denotes the fracture location.

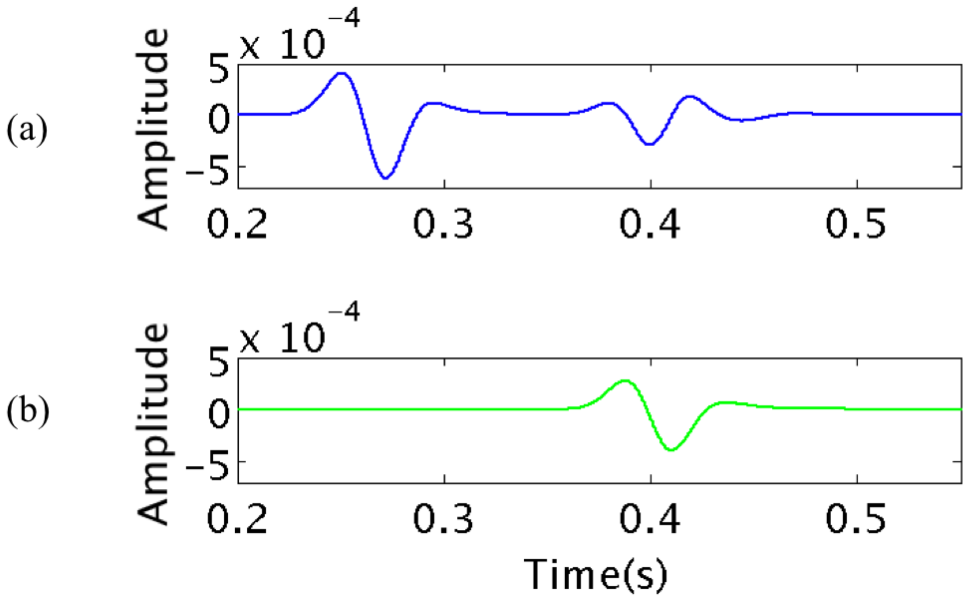

Figure 2.4: a). Incident wave and reflected wave recorded from the receiver above the fracture. b) Transmitted wave recorded from the receiver below the fracture.

increasing the number of elements in the $2km^2$ region. The correlation coefficients of different DG solutions with different element size and analytical solution are shown in Figure 2.6. The correlation coefficient curve begins as flat and approaches 1 if the number of elements greater is than 20. The comparisons of DG results and analytical solutions demonstrate the accuracy of the DGM. The linear slip condition describes a non-welded interface consistent with the reflection and transmission coefficients at the fracture interface.

I also compare the reflection and transmission coefficients with different fracture compliance values. In Figure 2.7a, the blue line denotes the incident wave and reflected wave for a fracture compliance of $1.8 \times 10^{-9} m/Pa$, and the red line denotes the incident wave and reflected wave for fracture compliance of $1.8 \times 10^{-10} m/Pa$. In Figure 2.7b, the blue line denotes the transmitted wave for a fracture with compliance of $1.8 \times 10^{-9} m/Pa$; the red line denotes the corresponding transmitted wave. The phases and amplitudes of the two incident waves are exactly overlapped. However, reducing the fracture compliance causes a decrease in the reflection coefficient and increase in the transmission coefficient. This DGM simulation illustrated that the reflection and transmission coefficients depend on the fracture compliance value. Thus, I validated the wave equation solution in 1D using the DG method.

2.3 Effect of fracture properties: Numerical investigation

Travel times and scattering patterns are two main azimuthal attributes of the reflected and scattered seismic waves often used to characterize discrete systems of vertical fractures. These seismic attributes could imply directional dependence of

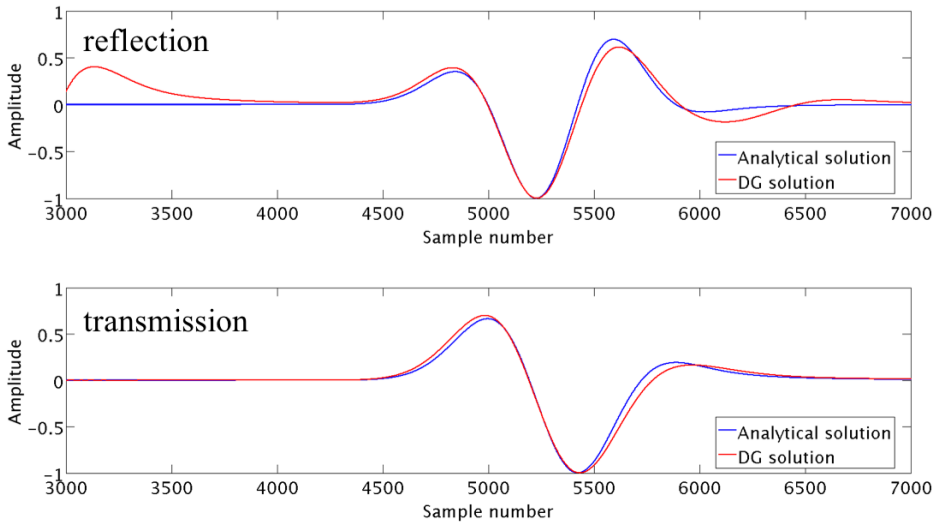

Figure 2.5: a). Blue line denotes the analytical solution of a reflected waveform derived from the linear slip condition. Red line denotes the DG simulated reflected waveform across the fracture represented by the linear slip boundary condition. b). Blue line denotes the analytical solution of transmitted waveform derived from the linear slip condition. Red line denotes the DG simulated transmitted waveform across the fracture represented by the linear slip boundary condition.

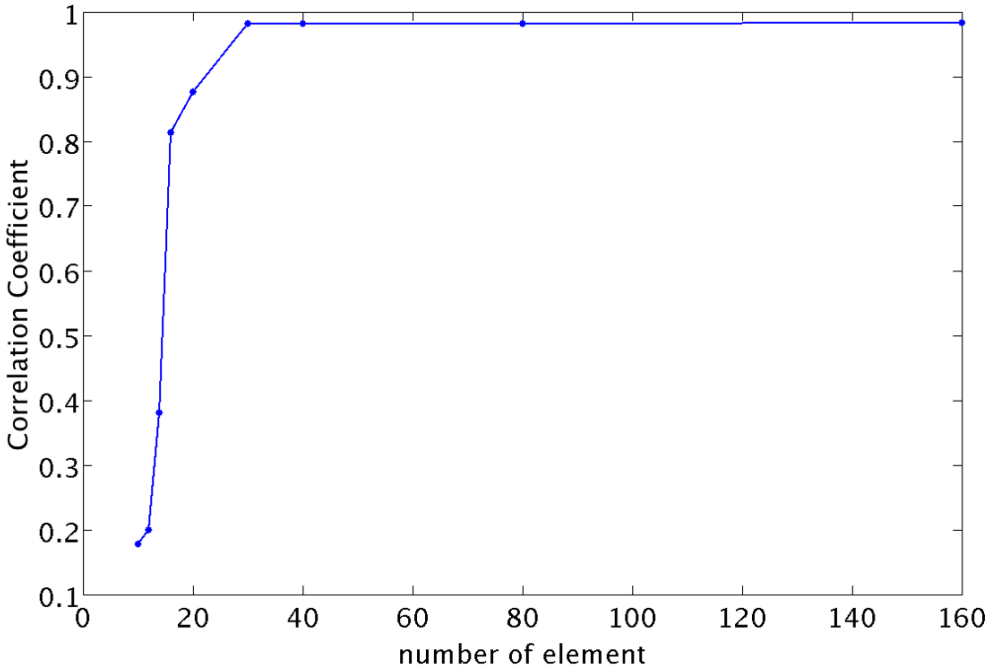

Figure 2.6: Correlation coefficients of DG solutions with different number of element in the 2km2 region and analytical solutions.

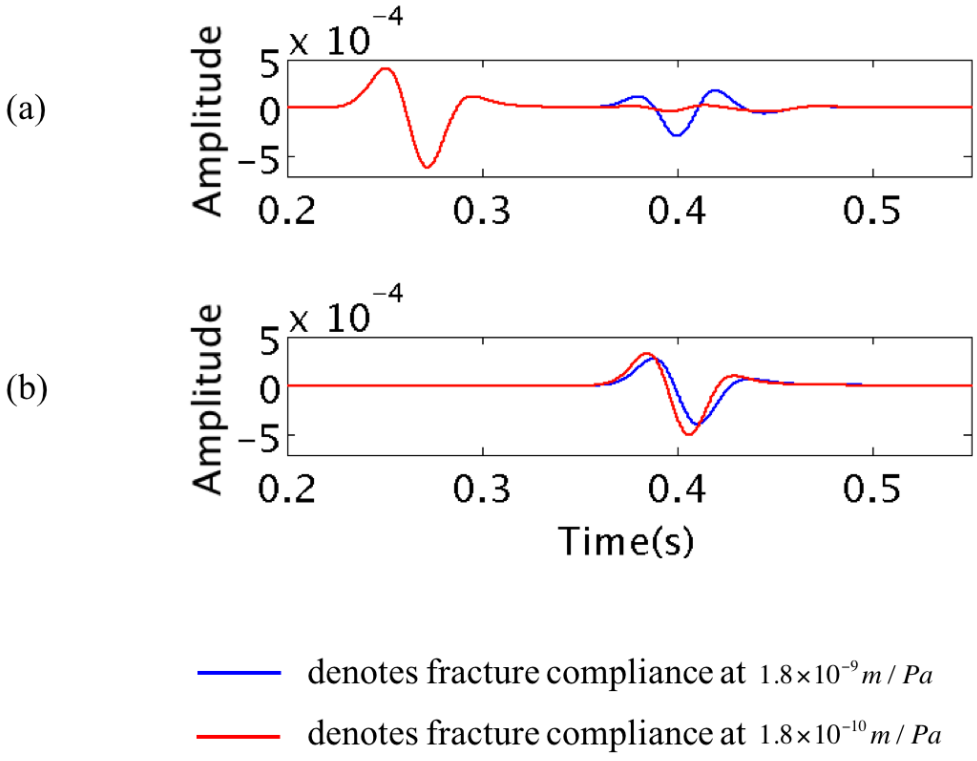

Figure 2.7: a) The blue line denotes the incidence wave and reflection wave for fracture compliance at $1.8 \times 10^{-9} m/Pa$; the red line denotes the incidence wave and reflection wave for fracture compliance at $1.8 \times 10^{-10} m/Pa$. b). The blue line denotes the transmission wave for fracture compliance at $1.8 \times 10^{-9} m/Pa$; the red line denotes the transmission wave for fracture compliance at $1.8 \times 10^{-10} m/Pa$.

fracture-induced anisotropy (Tsvankin et al., 2010). Therefore, they are valuable attributes associated with natural fracture systems.

Fracture-induced azimuthal anisotropy results in elliptical variations of the P- wavefront relative to the fracture strike direction. This is because the vertical fractures do not affect the P-wave along the fracture strike but do reduce the velocity perpendicular to the strike (Xu, 2011). The snapshots of wavefields explain the change of the wavefronts with regard to the fracture orientation (Figure 2.8). In an isotropic medium, the wavefront is circular with the source at the center because the wave travels in every direction with the same velocity (Figure 2.8, left). In the fracture-induced anisotropic medium, the wavefront has a non-circular shape. The shape of wavefront also depends on the fracture spacing (Figure 2.8, middle and right).

Fractures can scatter the P- and converted S- wave energy causing complex, reverberating seismic signatures (Figure 2.8, middle) when the fracture spacing is close in size to the seismic wavelength (Fang et al., 2014). This scattered seismic signature varies as a function of azimuth (Willis et al., 2006). Analytical solutions for scattering from realistic fractures are not available. Scattering from a system of fractures involves the scattering from individual fractures and the interaction of the scattered wavefield with other fractures in the system. Here, I study the scattering pattern in three planes perpendicular to each other in a 3D model.

To simulate the azimuthal effects of a wavefield using DGM in a 3D vertical fractured medium, a one-layer model with $2km \times 2km \times 2km$ dimensions and a set of parallel fractures are used. Because the fractures are modeled by the linear slip model boundary condition, the fracture is massless with zero opening. Fractures are chosen

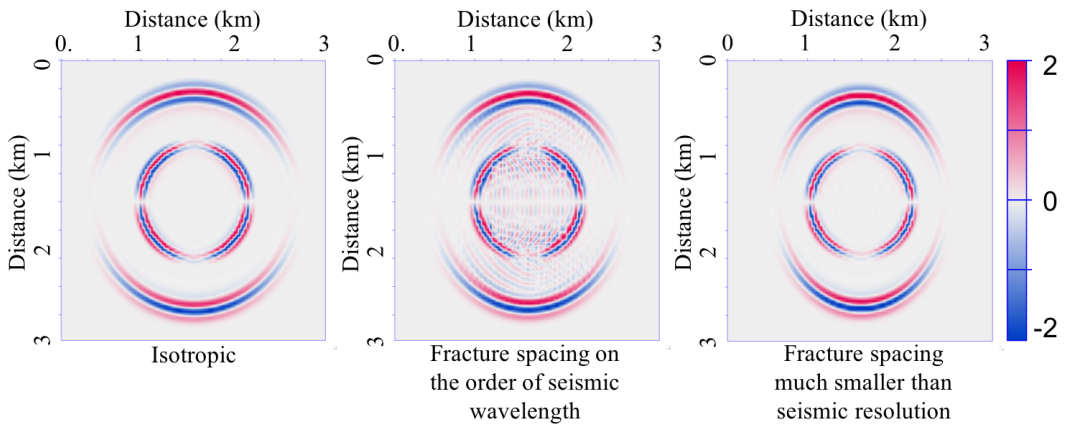

Figure 2.8: (Left) The snapshot of the wavefield for an isotropic medium. (Middle) The wavefield for vertical aligned fractures (fractures modeled as linear-slip discontinuities) with spacing on the order of a seismic wavelength. (Right) The wavefield for vertical aligned fractures (fractures modeled as linear-slip discontinuities) with spacing smaller than the seismic resolution.

Layer	Thickness (m)	$V_P(m/s)$	$V_S(m/s)$	$Density(g/cm^3)$	Fracture spacing (m)
1	2000	3000	1765	2200	200

Table 2.1: Parameters for a one-layer model

to be in vertical planes normal to the Y direction. I use a Ricker wavelet source with a peak frequency of $15Hz$ and causal time delay of $0.1s$. The point source is located at the center of the cubic model and polarized in the z direction. The normal and tangential compliances are set as $1.8 \times 10^{-10} m/Pa$. The model geometry and parameters used are shown in Table 1. Three planes (Figure 2.9, X-Z, Y-Z, X-Y plane) are extracted from the 3D wavefield. I obtained obvious scattering energy within the P wavefront and the S wavefront. These scattering effects are caused by the interaction of the reflected and transmitted waves among the fractures represented by the linear slip condition.

To observe detailed scattering effects, Figure 2.10 shows the z component for each plane. Figure 2.10a shows the X-Z plane, which is in the plane with fractures; and Figure 2.10b shows the Y-Z plane, which is orthogonal to all the fractures. For Figures 2.10a and 2.10b, the outer circles with small amplitude are the P wavefronts; the inner circles with large amplitude are the S wavefronts. The opposite phases indicate the reversed particle motions. The X-Y plane intersects the center of the model, and the particle motions of the P wave are in the X-Y plane. Therefore, the z component in the X-Y plane (Figure 2.10c) does not record the P wavefront; however, the scattered P waves still can be observed outside of S wavefront.

When I examine the X-Z plane, the scattered waves appear to be in spherical.

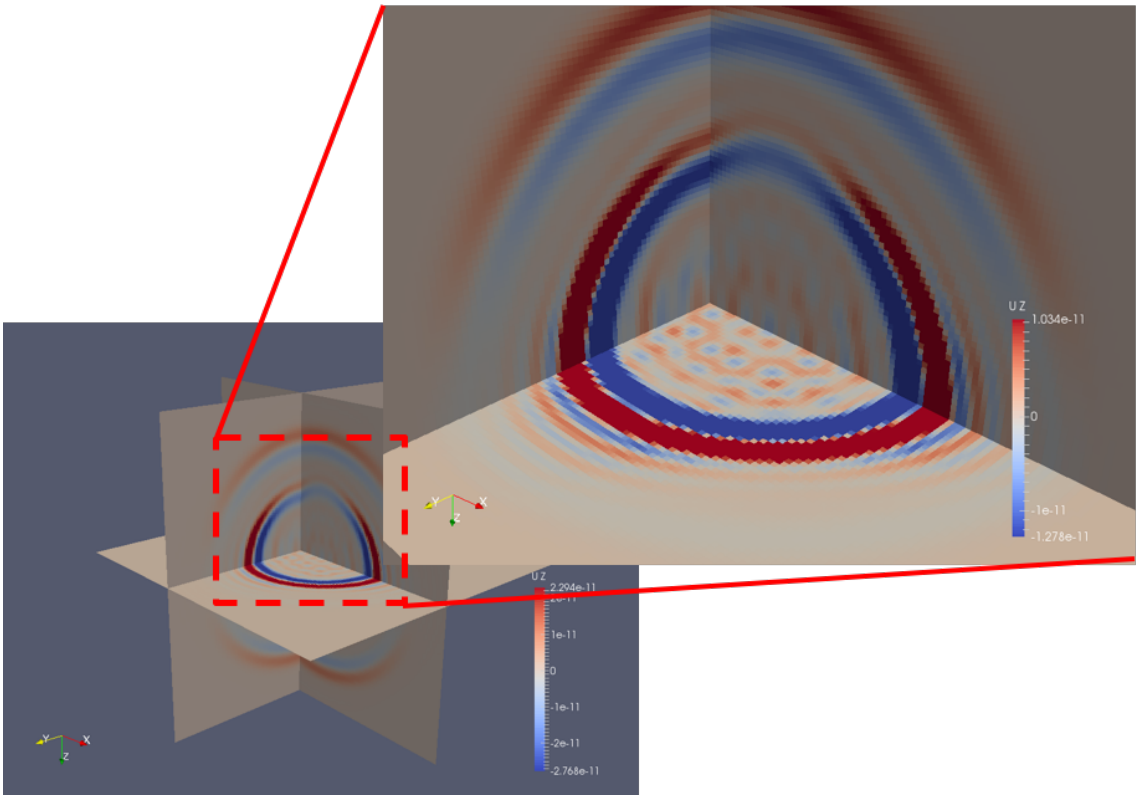

Figure 2.9: Z component for three planes (X-Z, Y-Z, X-Y plane) extracted from the 3D wavefield of a one-layer fractured medium. The P and S- wave scattering energy is obvious in the wavefield.

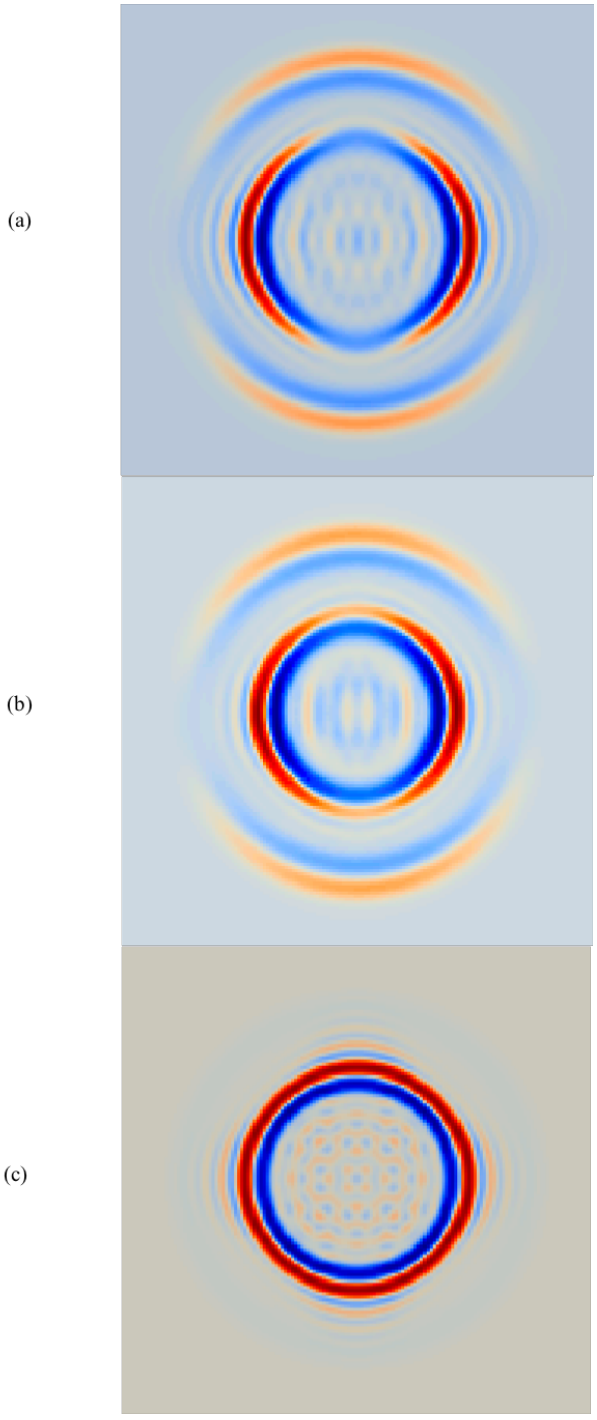

Figure 2.10: 3D displacement fields of z component in a one-layer model containing vertical fractures. a). Displacement field in X-Z plane, b). displacement field in Y-Z plane, and c). displacement field in X-Y plane.

Conversely, when I look into the Y-Z and X-Y planes, the scattered waves appear oriented in one direction. The wavefronts with positive and negative phases interacted due to the phase shift effects. In this case, the fracture spacing and the wavelength are both $200m$. The fracture network significantly scattered the P and S wavefields. However, the scattering pattern varies in different planes, as well as with azimuth. The differences come from the incident angle of the spherical wave when the incident wave reaches the fracture interface. The travel time difference between each axis is difficult to see because of the fracture spacing being large in this case.

A simple reservoir was modeled using a 3D isotropic, elastic discontinuous Galerkin finite element method, which employed 3D 4th order Lagrange polynomials and Gauss nodes. The Gauss basis function is used in this study because it leads to a diagonal mass matrix, and the Gauss nodes are always within the element, which leads to a discontinuity at the element interface. Two adjacent elements are allowed to have different values at the element boundary, and these characteristics satisfy the discontinuous wavefield. The model geometry (Figure 2.11) consists of three horizontal layers, with parameters listed in Table 2. All layers except the middle layer are homogeneous, isotropic, and elastic. The background medium for the middle layer is isotropic and homogeneous. A periodic series of parallel and vertical fractures are inserted into this layer simulated using the linear slip model.

The normal and tangential fracture compliance values were set of $1.8\times10^{-10}m/Pa$ to represent gas-filled fractures. The fracture interfaces are located at grid cell boundary; the fracture openings are assumed to be zero, and the vertical fracture planes are as thick as the middle layer thickness ($100m$), which run the entire width of the

Layer	Thickness (m)	$V_P(m/s)$	$V_S(m/s)$	$Density(g/cm^3)$	Fracture spacing (m)
1	400	3000	1765	2200	NA
2	600	4000	2353	2300	200m
3	1000	3000	1765	2200	NA

Table 2.2: Parameters for a three-layer model

model (i.e., parallel to y=0). I built a model with $200m$-fracture-spacing and used a Ricker wavelet source with a peak frequency of $8Hz$ and a causal time delay of $0.2s$.

The left side of Figure 2.12 shows the shot record for the model without fractures. The middle and right sides of Figure 2.12 show the shot records for the $200m$ fracture spacing case acquired in the direction normal and parallel to the fractures, respectively. The P-wave reflections off the top and bottom of the middle fractured layer arrive at zero offset times of about $0.46s$ (black dashed) and $0.76s$ (red dashed), respectively. The arrival at $0.56s$ (green dashed) at zero offset is the converted PS wave reflected off the top of layer 2. The shot record normal to the fracture network shows high amplitude of the PP reflection off the top and bottom of the middle fractured layer, and the PS reflection off the top of the middle fractured layer.

The effect of using the linear slip condition model to represent a fracture depends on the fracture compliance matrix. The numerical results confirm the reflection and transmission coefficients with the theoretical elastic wave behavior across linear slip interfaces. If the compliance value approaches zero, the fracture is equivalent to a perfectly bonded interface. However, if the compliance value tends to infinity, it will result in extremely small transmission coefficients from the fracture interface. I validated that the discontinuous Galerkin method provides good agreement with

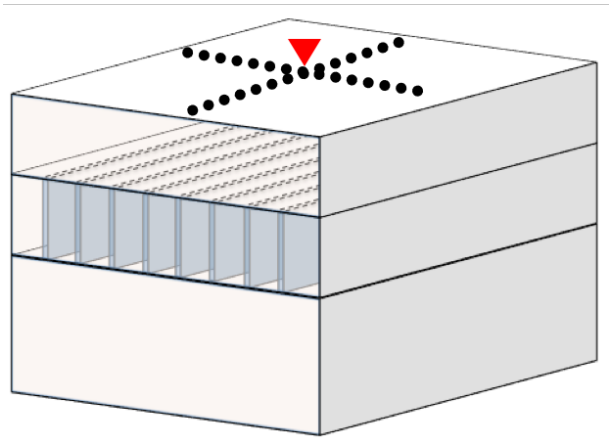

Figure 2.11: Geometry of the 3D DG-FEM model. The layer velocities and densities are shown in Table 2, the source is located in the center top front (triangle symbol), and the receivers are spread out in a cross shape, 2km in the x direction and 2km in the y-direction. The receiver spacing is 10m in each direction.

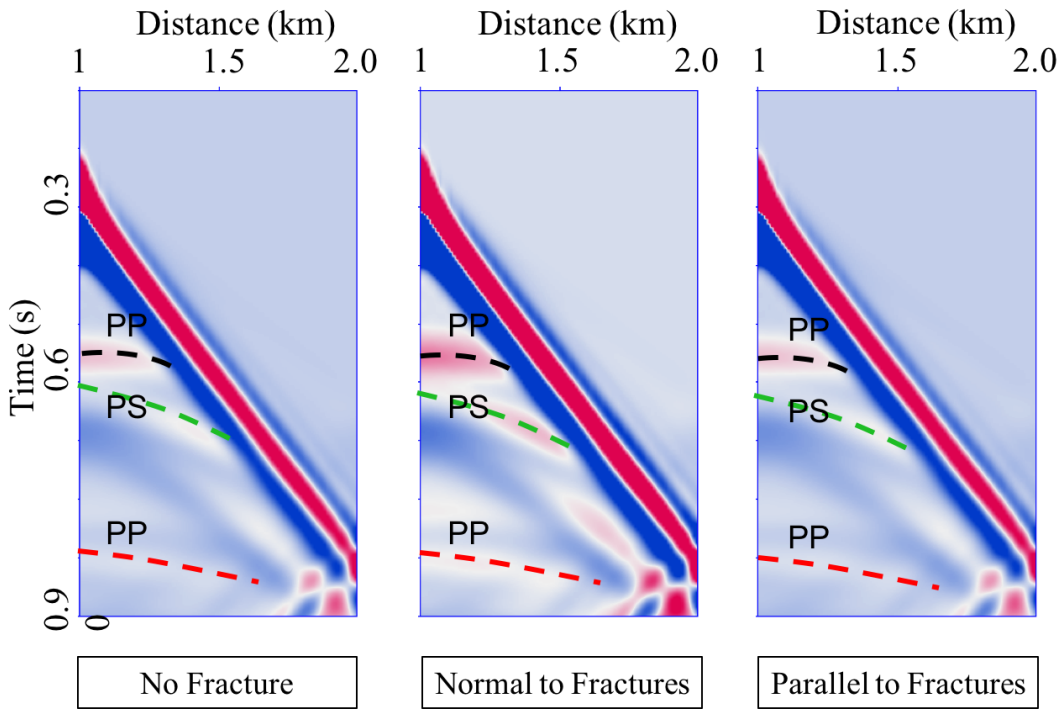

Figure 2.12: The left shot record is from the model without any fractures. The middle and right shot records are from the model with a 200m fracture interface spacing acquired normal and parallel to the fractures, respectively.

analytical solutions of the linear slip condition represented fracture. The amplitude and the phase are consistent with analytical results for both reflected and transmitted waves.

2.4 Limitations on 3D

For the model with a set of parallel-aligned fractures inserted into the middle layer, the scattered waves caused by the reflected and transmitted waves arrive immediately after the reflection off the top of middle layer (Figure 2.12). However, the scattered energy has small amplitude (Figure 2.12) due to the fracture spacing being large relative to the wavelength. Increasing the fracture density requires a finer mesh size, which will increase computational cost. In addition to that, DGM requires high degrees of freedom for a given sampling ratio, especially in 3D. In 3D, the computational cost grows significantly, which makes it much more time consuming.

2.5 Conclusions

In this chapter, I demonstrate that the discontinuous Galerkin method provides good agreement with analytical solutions for a fracture with the linear slip condition. 3D layer models containing both individual fractures and series of fractures were simulated using discontinuous Galerkin method. The results reveal the significance of effects of fractures on the elastic wave field. The variations of reflected and transmitted waves are highly dependent on compliance parameters. The fracture spacing also has significant influence, which will be investigated in chapter 3. These preliminary results also demonstrate the possibility of using the scattering

index function to characterize and quantify fracture attributes.

Chapter 3

Seismic modeling in 3D fractured media with Integral formulation

In this work, I implement a 3D explicit interface scheme with a geometrically irregular mesh following Zhang and Gao (2009). Arbitrarily shaped fractures can be accurately modeled with this discretization. This approach can provide detailed wave-propagation phenomena resulting from spatially heterogeneous fractures. The fractures in this scheme follow the linear slip displacement-discontinuity model (Schoenberg, 1980) by assuming tractions to be continuous while displacements have jumps that are proportional to the local tractions across the 2D fractures. The 2D fractures are modeled using a discretization with tetrahedral grid cells. Arbitrarily shaped 2D non-planar fractures can then be represented in the numerical mesh.

The integral approach used here is derived from the basic ideas of the finite element and finite difference methods. It is flexible in modeling irregular interfaces and surface topography. The memory requirements and computational costs are approximately equivalent to a second order staggered grid scheme (Virieux, 1986). However, unlike the conventional staggered grid scheme (Virieux, 1986), in a 3D case, I only need three displacements and three velocities instead of three velocities and six stresses in each time step.

Parallel computation is necessary to accommodate realistic 3D models. Owing to the numerical algorithm of the integral approach, small data exchanges between the subdomains are needed. The data exchanged between processors are the wavefield on the grids at the contacting boundaries of subdomains. I show several numerical results demonstrating the effect of varying fracture attributes in 3D models.

The compliance of the fractures affects seismic wave propagation primarily in terms of phase shifts and time delays (e.g., Schoenberg, 1980; Schoenberg and Sayers, 1995; DeBasabe et al., 2016). Both reflected and transmitted waves are commonly observed when waves encounter fractures. The phase shift is induced by the discontinuity at the fracture, which is directly affected by the fracture compliance. Higher fracture compliance will introduce larger a phase shift. However, when the fracture compliance reduces, approaching the effective stiffness of the surrounding matrix, the amount of transmitted energy increases. Usually, fractures appear in arrays or groups. This could lead to interference of reflected waves and transmitted waves. The complexity of this interference is directly determined by fracture spacing, orientation as well as compliance. Therefore, it is relatively simple to investigate wave propagation through an array of parallel fractures. In this work, I investigate the effect of fractures on wave propagation with varying fracture properties such as length, spacing, and density while aligning the fractures in the same orientation.

3.1 Integral formulations

The elastic wave equation to describe the propagation of compressional and shear waves in a 3D heterogeneous medium can be expressed in terms of displacements and stress as

$$\frac{\partial^2 u_i}{\partial t^2} = \frac{1}{\rho}\left(\frac{\partial \sigma_{ij}}{\partial x_j}\right), \tag{3.1}$$

$$\sigma_{ij} = \frac{1}{2} C_{ijkl}\left(\frac{\partial u_k}{\partial x_l} + \frac{\partial u_l}{\partial x_k}\right), \tag{3.2}$$

where i, j, k, $l = 1, 2, 3$, and I follow the Einstein summation convention; here, ρ is the density, x_i are the Cartesian coordinate components with x_3 pointing downward, u_i are the components of the displacement, σ_{ij} are the Cartesian components of the stress tensor and C_{ijkl} represents the fourth-order elastic stiffness tensor. The stiffness tensor can contain up to 21 independent parameters. However, for an isotropic medium, only two Lamé coefficients λ and μ are needed to determine the stiffness tensor.

Many numerical algorithms are available for solving the above elastic wave equation in a heterogeneous medium. Examples include finite difference (Virieux, 1986), spectral element (Tromp et al., 2008) and discontinuous Galerkin (De Basabe et al., 2008). Following Zhang and Gao (2009), I aim to simulate explicitly arbitrarily shaped discrete fractures in one medium; therefore, special efforts are needed to incorporate the linear slip model with the elastic wave equation under a discretization of 3D tetrahedral grid cells.

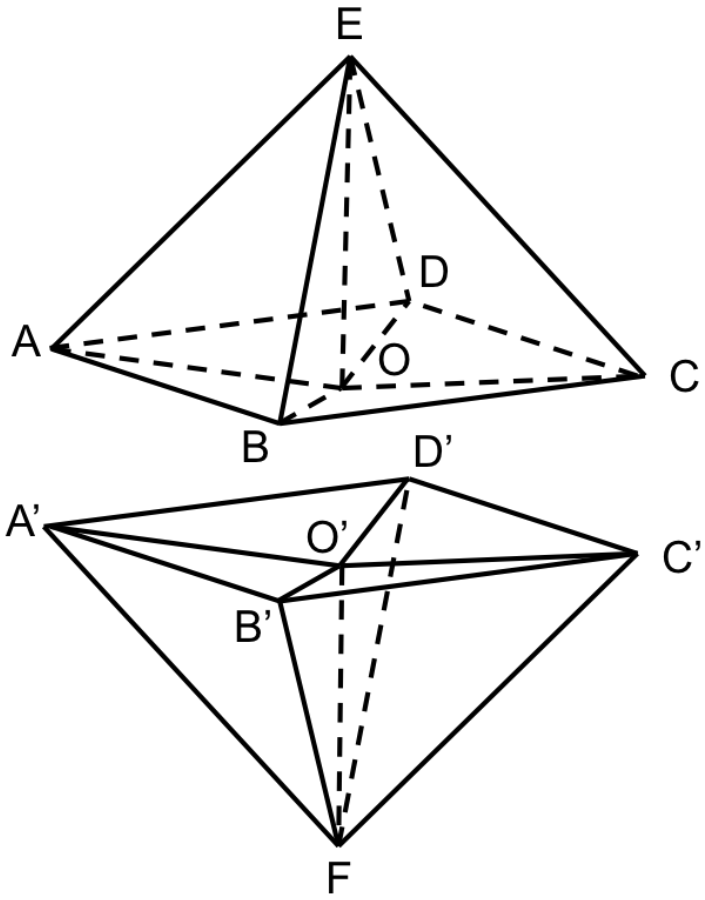

Figure 3.1: Local mesh surrounding a pair of nodes on a 2D non-planar fracture. The non-planar surfaces ABCDO and A'B'C'D'O' denote upper and lower surfaces of the fracture. The displacement components are defined at the nodes of tetrahedrons, as nodes O, A, B. The stress components are defined at the centers of tetrahedrons. The distance between the upper surface and lower surface is created for visualization purpose only. The fracture is assumed to have a vanishing width. A pair of nodes, such as O and O', is defined at the same position on the fracture, but each has a different displacement corresponding to the upper or lower surface of the fracture. Hence, displacement discontinuity can be described from the difference between the pair of nodes (from Zhang and Gao, 2009).

The integral formulation of the 3D elastic wave equations, including the linear slip (LS) model, is derived under the assumption of tetrahedral grid cells. Zhang and Gao (2009) proposed an explicit scheme for solving the elastic wave equation using tetrahedrons. Here I describe their method briefly, for completeness. The problem is formulated in terms of displacements at the nodes and stresses at the center of each tetrahedral grid cell; a pair of nodes instead of a single node is defined at the grid point on the explicit fractures. Figure 3.1 shows an example of local numerical mesh of a 2D non-planar fracture. The local mesh contains six tetrahedral cells that surround a pair of nodes OO' on a fracture. The non-planar interface $ABCDO$ and $A'B'C'D'O'$ denotes upper and lower surfaces of the fracture. In the linear slip model, the fractures have vanishing width. This implies that every pair of nodes, such as O and O', is defined at the same grid point on the fracture and share the same coordinates.

Following the divergence theorem, I integrate both sides of Equation 3.1 over the volume inside the polyhedron V leading to

$$\iiint_V \rho \frac{\partial^2 u_i}{\partial t^2}\, dV = \oint \int_S \left(\sum_{j=1}^{3} \sigma_{ij} n_j \right) ds \approx \sum_{l=1}^{m} \sum_{j=1}^{3} \sigma_{ij}^{l} \left(c_j^O \right)_l + \iint_\Omega \sum_{j=1}^{3} \sigma_{ij} n_j ds, \quad (3.3)$$

where n_j are directional cosines of the outward normal to the surface S, m is the number of grid cells above the surface of the fracture around node O, σ_{ij}^l denote the stress components at the center of the lth grid cell, Ω is the region of the sum of 1/3 region from each facet on the upper surface of the fracture, $\left(c_j^O\right)_l$ denotes the geometrical coefficients of the lth grid cell, that is $\iint n_j^l$ ds. For example, the

coefficients in cell $OCED$ can be expressed as

$$\left(c_1^O\right)_l = \frac{1}{6}\begin{vmatrix} 1 & x_2^C & x_3^C \\ 1 & x_2^E & x_3^E \\ 1 & x_2^D & x_3^D \end{vmatrix}, \left(c_2^O\right)_l = \frac{1}{6}\begin{vmatrix} x_1^C & 1 & x_3^C \\ x_1^E & 1 & x_3^E \\ x_1^D & 1 & x_3^D \end{vmatrix}, \left(c_3^O\right)_l = \frac{1}{6}\begin{vmatrix} x_1^C & x_2^C & 1 \\ x_1^E & x_2^E & 1 \\ x_1^D & x_2^D & 1 \end{vmatrix}, \quad (3.4)$$

where x_j^C, x_j^E, x_j^D, for j=1, 2, 3 are the coordinates of the three nodes of the lth grid cell.

By applying the lumped mass model to the discretized system, which is lumping the mass of the region that is enclosed by a grid cell at its nodes and setting the density (ρ) to zero out of nodes, the left hand side of Equation 3.3 becomes $M_O(\partial^2 u_i/\partial t^2)_O$. M_O is a quarter of the sum of the masses of the grid cells above the surface of the fracture around node O. $(\partial^2 u_i/\partial t^2)_O$ are the second order time derivatives of the displacement components at node O.

Substituting the LS model of Equation 1.9 into the second term on the right-hand side of Equation 3.3 yields the integral formulation of the 3D elastic momentum equations as

$$M_O(\partial^2 u_i/\partial t^2)_O = \sum_{l=1}^{m}\sum_{j=1}^{3}\sigma_{ij}^l\left(c_j^O\right)_l + \sum_{k=1}^{3}\left[\sum_{j=1}^{3}\frac{\overline{\mathrm{T}}_{jk}\overline{\mathrm{T}}_{ij}}{(\eta_{jj})_O}\right]G_O\left(\Delta U_k\right)_O, \quad (3.5)$$

where T_{ij} ,η_{jj} and ΔU_k denote the components of T, Z, and ΔU that are prescribed in Equations 1.8-1.10, and G_O is given by

$$G_O = \sqrt{\sum_{k=1}^{3}\left[\sum_{l=1}^{m_f}\left(c_k^E\right)_l\right]^2}. \quad (3.6)$$

Here m_f denotes the number of the grid cells that have one facet on the fracture and a node at O.

Similarly, by integrating both sides of Equation 3.1 over the volume V', which is a quarter of the volume of all the cells below the surface of fracture, I obtain

$$M_{O'}(\partial^2 u_i/\partial t^2)_{O'} = \sum_{l=1}^{m'} \sum_{j=1}^{3} \sigma_{ij}^{l} \left(c_j^{O'}\right)_l - \sum_{k=1}^{3} \left[\sum_{j=1}^{3} \frac{\overline{\mathrm{T}}_{jk}\overline{\mathrm{T}}_{ij}}{(\eta_{jj})_O}\right] G_O \left(\Delta U_k\right)_O , \tag{3.7}$$

where m' denotes the number of grid cells below the surface of fracture around node O', and $M_{O'}$ is a quarter of the sum of the masses of grid cells below the surface of fracture around node O'. The explicit fracture is expressed in the second term on the right-hand side of Equations 3.5 and 3.7 using continuity of tractions. In a medium where fractures do not exist, the integral formulation in the absence of the LS model is

$$\left(M_O + M_{O'}\right)(\partial^2 u_i/\partial t^2)_O = \sum_{l=1}^{m+m'} \sum_{j=1}^{3} \sigma_{ij}^{l} \left(c_j^{O}\right)_l . \tag{3.8}$$

I use Equation 3.8 when computing the displacement field in the background medium. I use Equations 3.5 and 3.7 when computing the displacement field on the fractures. When the normal and tangential fracture compliances η tend to zero, which implies the fracture is perfectly welded, the displacement discontinuity ΔU vanishes, and the combination of Equations 3.5 and 3.7 yield the same as Equation 3.8.

3.1.1 Point source and explosive source

Elastic body waves can be classified into compressional (P) wave and shear (S) wave. The P wave is defined as the particles in the solid vibrating along the axis of propagation. The S wave is defined as the particles in the solid vibrating perpendicular to the axis of propagation.

The simplest possible source of elastic waves is a point force. It can be easily implemented on a grid point by adding a source function. The commonly used source function in seismic modeling is a Ricker wavelet. The point source is unidirectional; therefore, it can generate both P and S waves from the source location. The amplitude of both P and S waves vary with azimuth. Figure 3.2 (a) shows the wavefield of both P and S wave in Z component that generated by a vector point source placed in vertical downward direction. Because the vector point source is directional, when one side of the source is under compressional stress, the other side is under tensional stress in reversed direction of the compressional stress. This is why, in Z component, the top half of the wavefield on Figure 3.2 (a) has a different polarity with the bottom half.

On the contrary, an explosive source generates equal pressure in all directions in isotropic media. The implementation of this source is achieved by assigning equal displacements at the nearest nodes distributed on the spherical surface. The direction of each assigned displacement follows the vectorial direction between the source and the node. For example, in Figure 3.2, if I assume an explosive source is placed at the centroid of an tetrahedron cell CBEH, nodes A, B, C, D, E, F, G, H are distributed on a spherical surface with the same radius. Equal displacements will be assigned at nodes A, B, C, D, E, F, G, H with direction points outward from source location. The

wavefield comparison between point source and explosive source is shown in Figure 3.3. Similarly to point source, when I plot only the Z component of the wavefield, there is a polarity reverse from the bottom half to the top half in it.

3.1.2 Numerical implementation

I implemented the 3D explicit interface scheme on grid cells consisting of tetrahedral elements. The implementation workflow is flexible to accurately model arbitrarily shaped fractures in the numerical discretization. The displacement field at time $t + \Delta t$ is updated by using the displacement field at time t and $t - \Delta t$. The procedure contains two main loops. The first one loops over all the grid cells in the background medium in the absence of fractures. During this loop, I use the displacement components on each node at time step t. However, the stress components are intermediate variables, so they do not need to be stored in the loop. This leads to a reduction of memory cost. The second one only loops through the node pairs on the fractures and computes ΔU components and the force components caused by the ΔU. I then add the force back to the corresponding pair of nodes. After completing the first two loops, I have finished the computation of the right-hand side of Equations 10, 12 and 13 for all nodes in the domain. This implies that I have obtained the second-order time derivatives of the displacement components for all nodes at time t. The update of the displacement field at time $t + \Delta t$ can then be obtained using central finite differences.

Fractures are implemented on the facets of the grid cells. The space interval controls the fracture spacing and density. The smallest space interval in the mesh

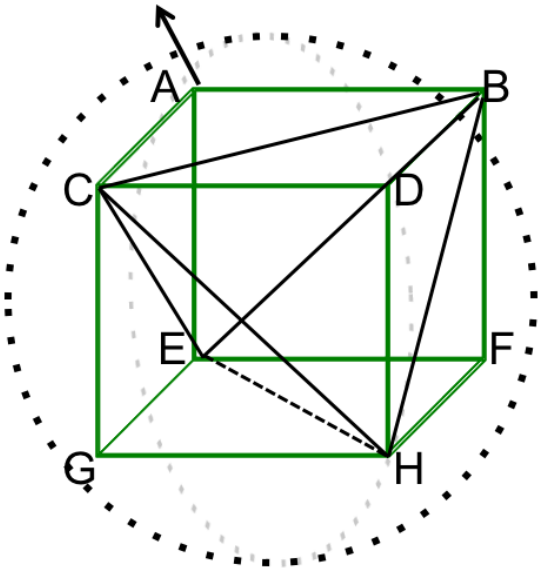

Figure 3.2: Schematic of implementing explosive source in the integral method. If an explosive source is placed at the centroid of an tetrahedron cell CBEH, nodes A, B, C, D, E, F, G, H are distributed on a spherical surface with same radius.

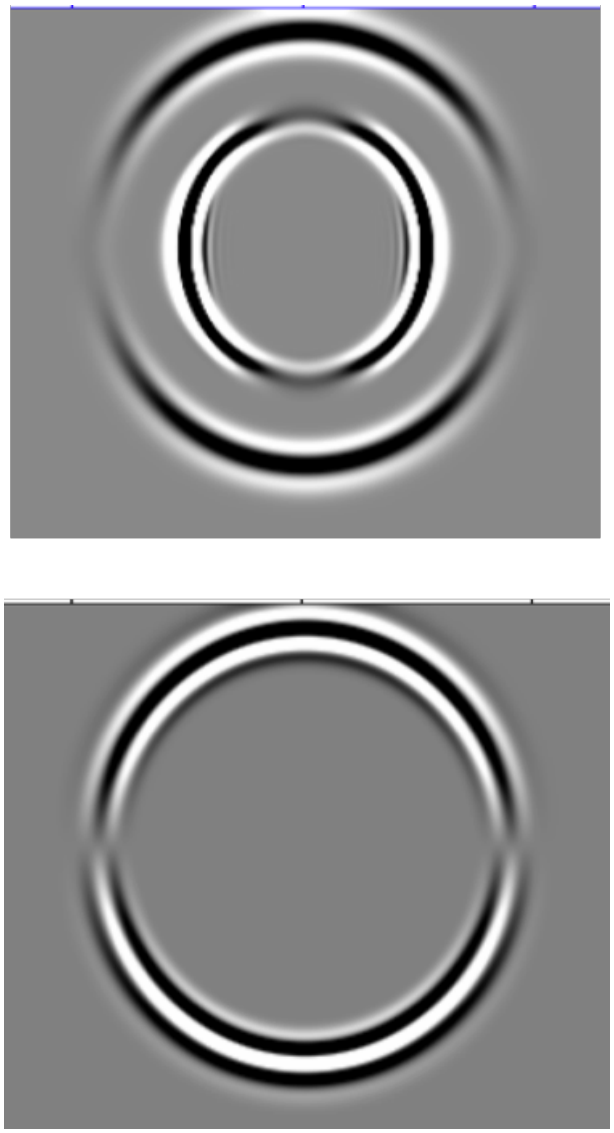

Figure 3.3: The wavefields generated by a point force and an explosive source. The top wavefield is generated by a point force in z direction. The bottom wavefield is generated by an explosive source.

determines the smallest fracture spacing and density. For congruent tetrahedral grid cells in the domain, I only need to store one volume and 12 geometric coefficients based on Equation 9. The nature of arbitrary facets in a tetrahedral grid cell makes it flexible in modeling subsurface fractures in any direction. A transform matrix of the coordinate system is needed for fractures with a normal direction not pointing to the x_1- , x_2-, or x_3-axis.

The parallel implementation of the calculation scheme can be completed by using small additional exchange operations. Because exchanges occur only between the nodes on the contacting boundaries without any internal nodes, this reduces the memory cost during the exchange procedure and can achieve a high speed-up rate. The parallel implementation scheme is achieved by spatial division in combination with the exchange operations. The computing domain is first divided into subdomains with fractures as natural boundaries. The seismic modeling is conducted in parallel within each subdomain. The nodal displacements are exchanged at each subdomain boundary during each time step. In this way, the computational efficiency is increased significantly.

3.2 Model validation

To examine the effect of the integral formula on modeling the seismic response of fractures, validation is necessary of reflection and transmission coefficients across the linear slip boundary condition. The analytical solution of the linear slip condition for a single fracture inserted into the medium is derived by Schoenberg (1980). With the linear slip boundary condition, the reflection and transmission coefficients can be

expressed as

$$R = -\frac{Z_1 - Z_2 - iw\eta Z_1 Z_2}{Z_1 + Z_2 - iw\eta Z_1 Z_2}, \tag{3.9}$$

$$T = -\frac{2Z_1}{Z_1 + Z_2 - iw\eta Z_1 Z_2}, \tag{3.10}$$

where $Z_i = \rho_i \alpha_i$, α_i for compressional wave velocity, w for frequency, and $\eta = \eta_N$ for a normal incidence compressional wave.

I simulate a wave field in a $2km^3$ homogeneous, isotropic, linear-elastic space containing a single horizontal fracture located at a depth of $1km$. The model geometry used in the simulation is shown in Figure 3.4. The elastic medium occupies the entire region, with density $2200g/cm^3$, compressional wave velocity $3000m/s$, and shear wave velocity $1765m/s$. The normal and tangential compliance for the single fracture are both $1.8 * 10^{-9} m/Pa$. The normal incidence compressional wave propagates towards the fracture.

A receiver was placed 200m above and below the fracture. I convolved the incident wave with the analytical reflection and transmission coefficients calculated from Equations 14 and 15. The comparison between the analytical solution and integral solution for reflection and transmission responses are shown in Figure 3.5. The reflection and transmission responses are consistent with the analytical solutions.

I conducted an additional parametric study by varying the fracture compliance. The reflected and transmitted waveforms are compared in Figure 3.6. The reduction in compliance causes the increase in the magnitude of the transmitted wave. However,

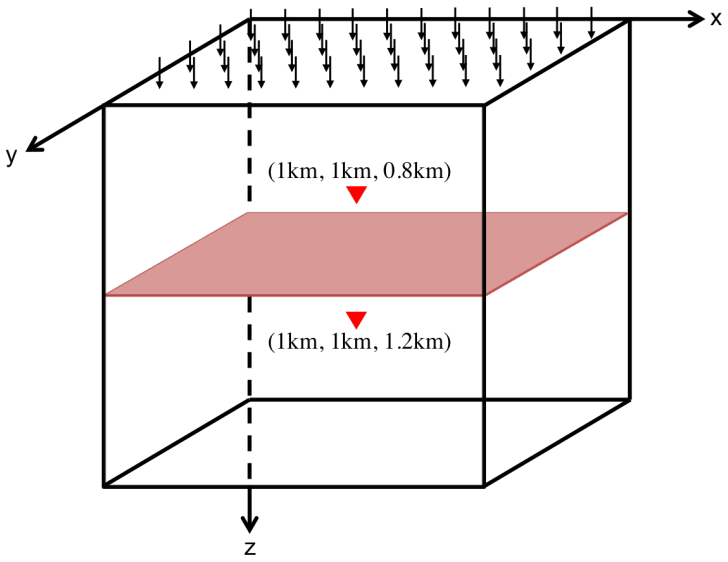

Figure 3.4: Model used for validation: the red plane denotes a 2D horizontal fracture inserted at a depth of $1km$. The black arrows denote the plane wave source applied on the top surface. The two red triangles denote the receivers placed 200m above and below the fracture.

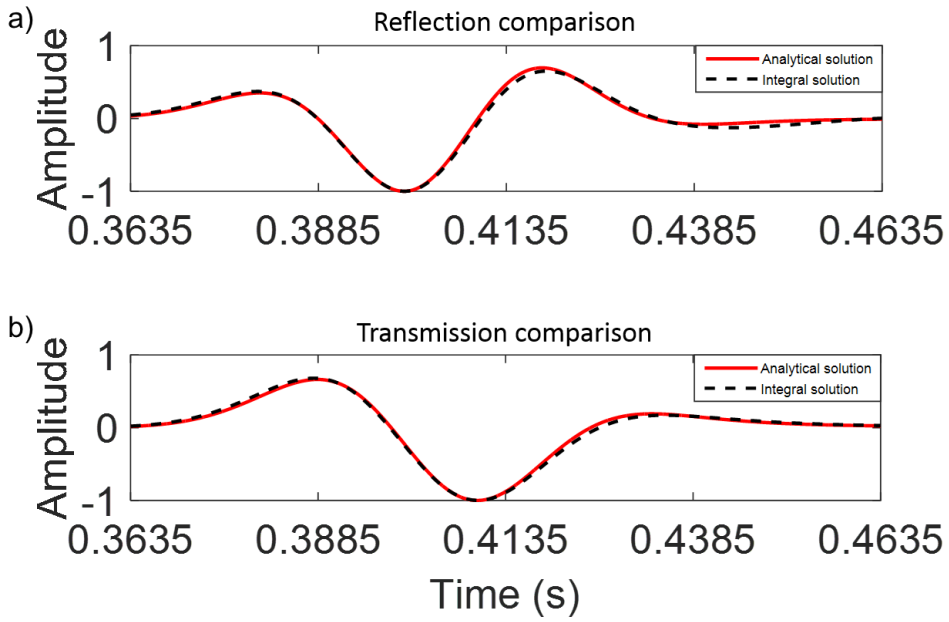

Figure 3.5: a) The red line denotes the analytical solution of a reflected waveform derived from the linear slip condition. The dashed black line denotes the integral method simulated waveform reflected from the fracture represented by the linear slip boundary condition. b) The red line denotes the analytical solution of a transmitted waveform derived from the linear slip condition. The dashed black line denotes the integral method simulated transmitted waveform across the fracture represented by the linear slip boundary condition.

the magnitude of the reflected wave drastically reduces as the compliance decreases. Similar results were reported in Carcione et al. (2012) and Liu et al. (2016).

3.3 Numerical examples on different fracture properties

Single fracture model

A vertical rectangular fracture in the YZ plane, with a height of $400m$ and length of $400m$, is positioned $500m$ away from the source on the right side in a 3D homogeneous medium. The homogeneous background medium has a P-wave velocity of $3km/s$, S-wave velocity of $1.765km/s$, and density of $2200kg/m^3$. A Ricker wavelet point source with a peak frequency of $15Hz$ is used. For the purpose of highlighting the scattered waves, the fracture compliances are chosen to be $1.0 * 10^{-7}mPa^{-1}$ for η_N and η_T, which is higher than natural fractures. This numerical model uses $400*400*400$ discretized grid points with an even spatial spacing of $10m$. The time step is $2ms$. The numerical mesh is made up of tetrahedral grid cells.

Figure 3.7 shows 2D slices of the wavefield snapshots of the vertical component of the displacement at $0.558s$. Three panels display three spatial directions. The transmitted and reflected waves from the fracture and diffracted waves from the fracture edges and tips can be observed clearly in Figure 3.7.

Figure 3.8 shows the 2D slices of the snapshot for the multi-component displacement field of the YZ plane at $0.558s$. The transmitted and reflected waves from the fracture, diffracted waves from the fracture edges and tips, and fracture surface waves (secondary surface wave induced by the fracture) can be clearly seen on each component.

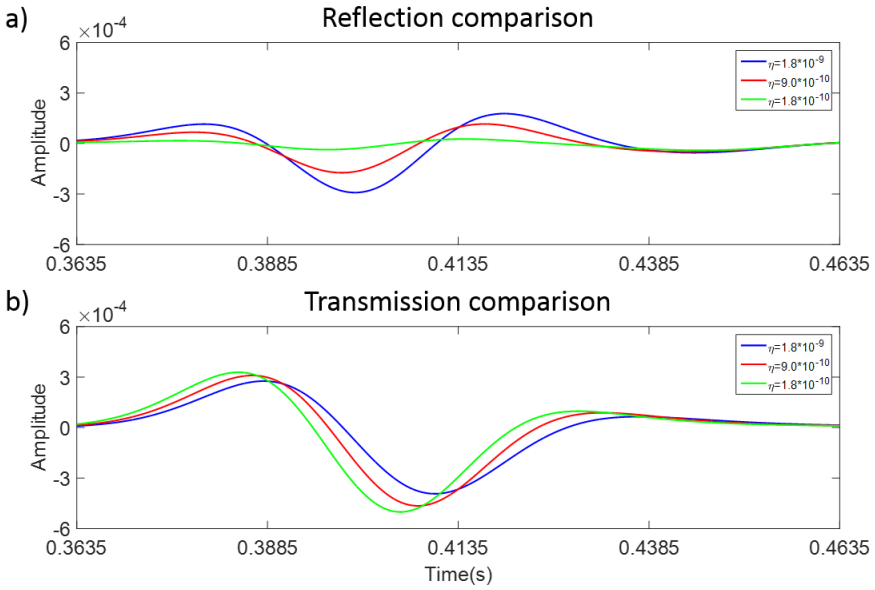

Figure 3.6: a) Reflection Comparison: $\eta = 1.8 * 10^{-9}$ (blue), $9.0 * 10^{-10}$ (red), $1.8 * 10^{-10}$ (green). b) Transmission Comparison: $\eta = 1.8 * 10^{-9}$ (blue), $9.0 * 10^{-10}$ (red), $1.8 * 10^{-10}$ (green).

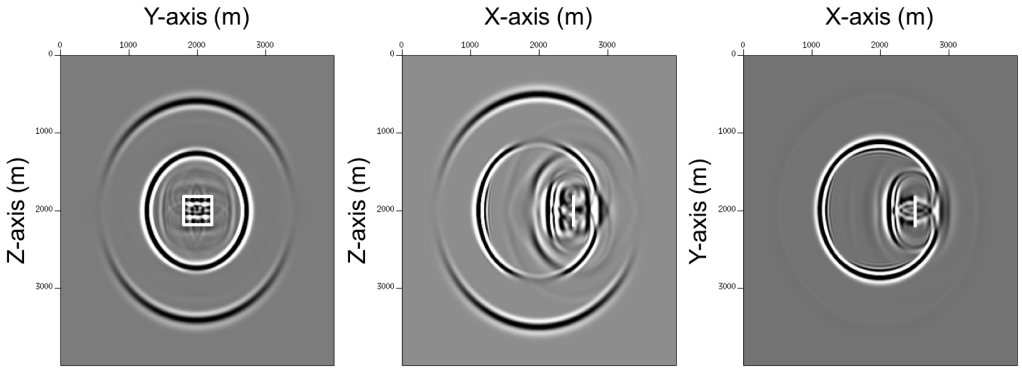

Figure 3.7: 2D slices of the wavefield snapshot of the vertical component of the displacement for a vertical rectangular fracture inside a homogeneous background medium at $0.558s$. Each axis has the same length of $4km$. The fracture is a 2D rectangular plane, with a height of $400m$ and length of $400m$, positioned $500m$ away from the source on the right side. The slices from the left to the right are, respectively, related to the XZ-plane that coincides with the fracture (the white rectangular symbol highlights the fracture position), YZ-plane and XY plane that pass through the center of the fracture. The transmitted and reflected waves from the fracture, diffracted waves from the fracture edges and tips, and fracture surface waves can be seen clearly.

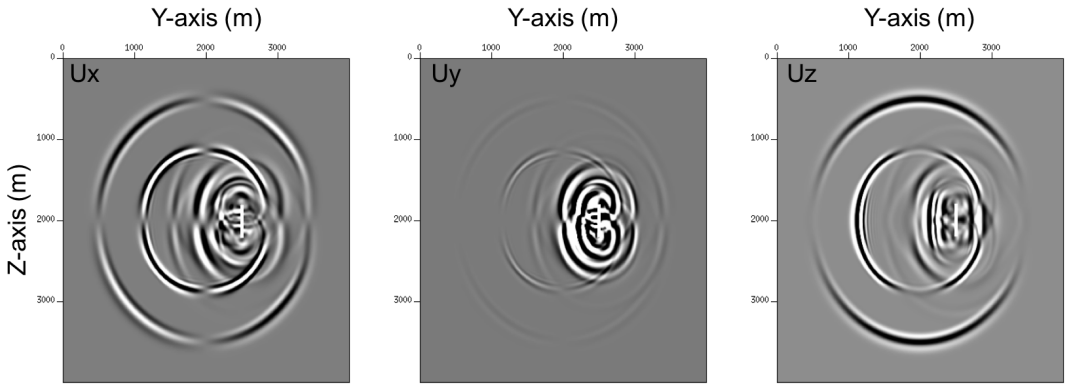

Figure 3.8: 2D slices of the snapshot the multi-component displacement field of the YZ plane at 0.558s. Three slices are, respectively, x, y and z components. The transmitted and reflected waves from the fracture, diffracted waves from the fracture edges and tips, and fracture surface waves can be clearly seen from each components.

Fracture set models

In this numerical modeling, I study the effects of fracture length, spacing, and density on the seismic responses. I consider the medium to be homogeneous, isotropic, and elastic. I assign fractures with compliance η_N and η_T both equal to $1.0 * 10^{-10} mPa^{-1}$, which represent gas-filled fractures (Sayers et al., 2009). Here and after, fracture compliance means both fracture normal and tangential compliances. Different sets of parallel fractures are inserted into the layer. The background medium for the fractured domain is isotropic and homogeneous. The model geometries are shown in Figure 3.9. I show results for four different scenarios: (1) fixed fracture length, spacing, and density, (2) varying fracture length, fixed fracture spacing and density, (3) fixed fracture length, spacing, and density, but smaller fracture spacing than scenario (1), (4) varying fracture density, fixed fracture length and spacing.

In the reference fracture model, fractures with equal length, spacing, and density are normal to the X-axis. The fracture length is $1000m$, spacing is $5m$, and fracture density is $1.2e-5$. Figure 3.10 shows examples of shot records acquired along the Y- and X- axes, parallel and normal to fractures, respectively. Although I see some boundary effect near the right boundary after $0.8s$, these results were not used to show the effects of fractures here or in later analysis.

From the shot gather, I found most of the scattering occurred in the range within the X-offset and Y-offset between 0 to $1500m$. More significant scattering was found in the X-offset plane than in the Y-offset plane. As the fracture spacing was uniform, I observe that the scattering pattern seems to be regular and with uniform spacing. This clear pattern indicates similar phase shifts in transmitted and reflected

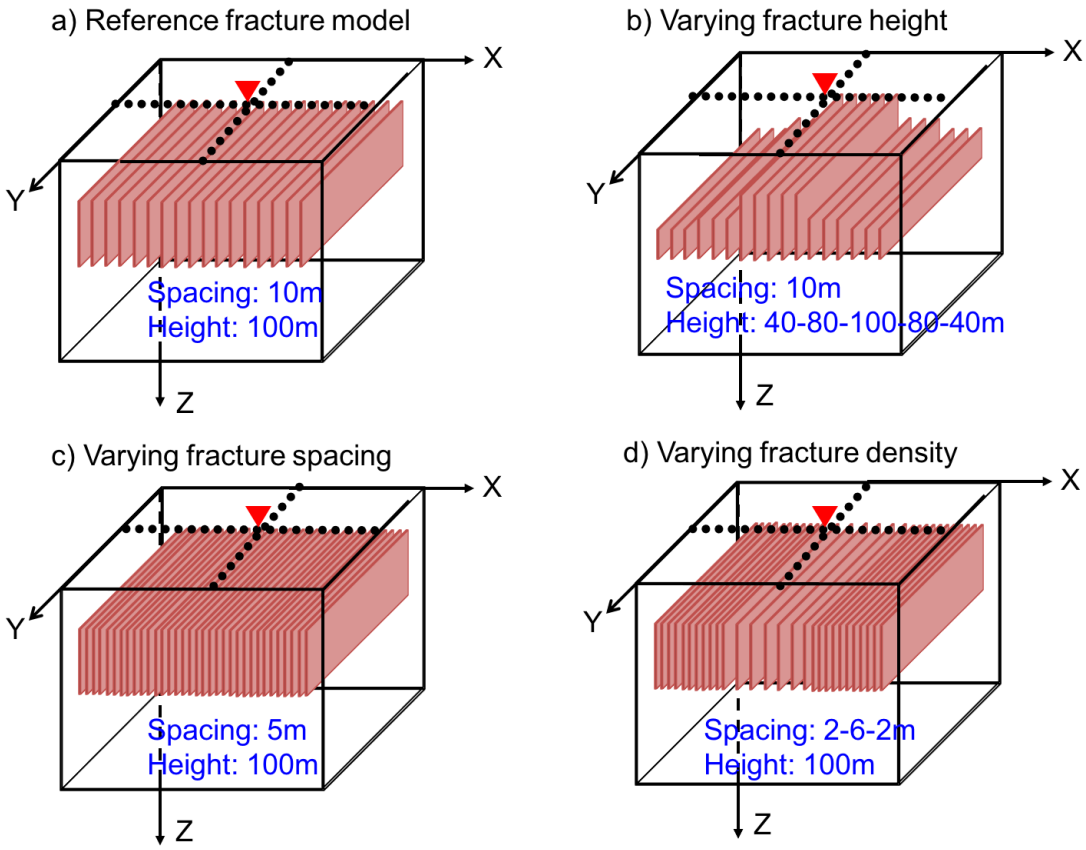

Figure 3.9: Four models used for generating synthetic seismograms: a) Reference fracture model with equal length, spacing, and density; fractures are normal to the X-axis. The fracture length is $400m$, spacing is $5m$, and fracture density is $1.2e-5$. b) Fractures with length of $400m$ for the near X-offset ($0m$ $400m$), $800m$ for mid X-offset ($400m$ $1200m$), $40m$ for far X-offset ($1200m$ $2000m$), spacing of $5m$, and fracture density of $1.2e-5$ normal to the X-axis. c) Factures with equal length, spacing, and density are normal to the X-axis. The fracture length is $1000m$ and fracture density is $1.2e-5$. I change the fracture spacing to $5m$. d) fractures vary laterally along the X-axis, with fracture density of $1.2e-5$ and $2.4e-5$ alternatively occurring for six times. The fracture length is $1000m$. Fracture spacing is $5m$ when fracture density is $1.2e-5$. Fracture spacing is $10m$ when fracture density is $2.4e-5$. The source (triangle symbol) is located in the center top front, and the receivers (black dots) are spread out in a cross shape. The domain is $4km$ in both X- and Y-direction, and $2km$ in the Z-direction.

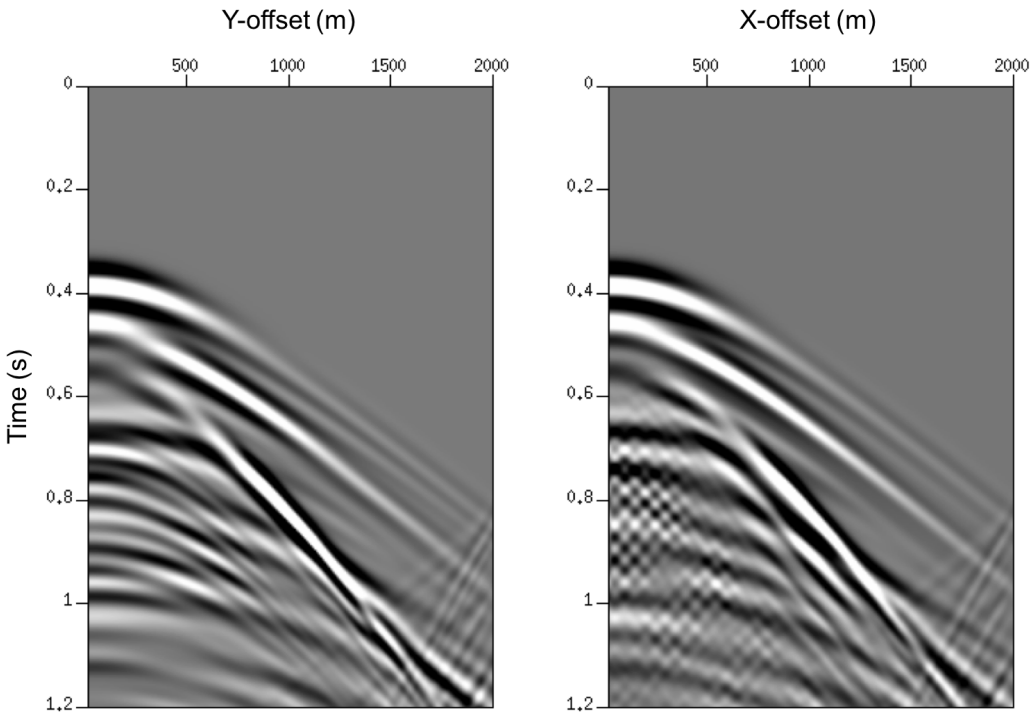

Figure 3.10: Shot records acquired from the reference fracture model along the Y- and X- axes, i.e., the gathers acquired parallel (left) and normal (right) to fractures respectively. Scattered energy is within 0-1500m in X- and Y-offset, during the time period between 0.6-1.2s.

waves due to the equal fracture spacing.

By varying the fracture length, the sources of the scattering change as well. This will disturb the regular pattern in the scattered waves seen previously. In the second model, fractures with length $1000m$ for the near X-offset ($0m - 400m$), $800m$ for the mid X-offset ($400m - 1200m$), $400m$ for the far X-offset ($1200m - 2000m$), spacing of $5m$, and fracture density of $1.2e-5$ are normal to the X-axis. Figure 3.11 shows examples of shot records acquired parallel and normal to fractures.

The shot gather from the second model shows that the scattering mainly occurs in the X-offset plane, which is perpendicular to the fracture plane. However, the scattering pattern is quite blurry. This is caused by the changes in the locations of the scattering sources (which are mainly at the edges of the fractures), which in turn reduces the chances of having constructive or destructive interference from the reflected and transmitted waves.

Similar to the reference model, in the third fracture model, fractures are normal to the X-axis, with equal length, spacing, and density. The fracture length is $1000m$, and fracture density is $1.2e-5$. I change the fracture spacing to $5m$. Figure 3.12 shows examples of shot records acquired parallel and normal to fractures. As the fracture spacing reduces, the fracture compliance in this region increases. With higher compliance, I have more significant phase shifts. Significant disturbance was found by the scattered wave passing through the individual fracture within each array. These cause the reduction in wave interference, which causes the blurry pattern in the shot gather.

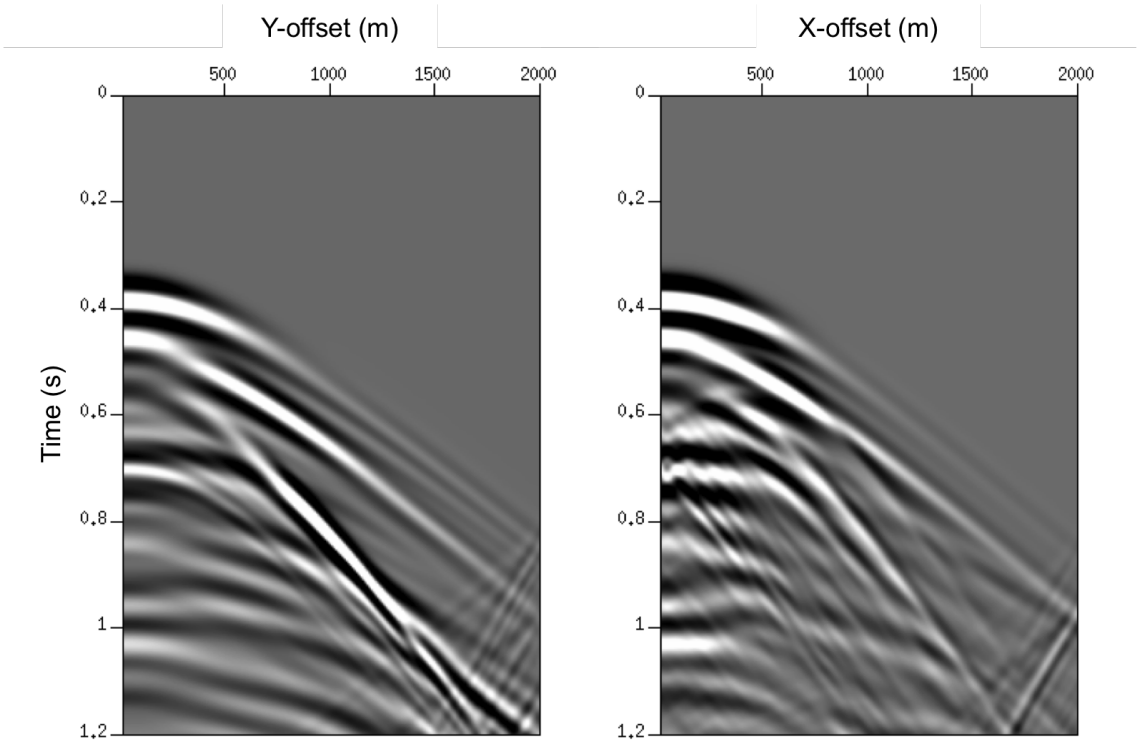

Figure 3.11: Shot records acquired from the fracture model with varying lengths along the Y- and X- axes, respectively, i.e., the gathers acquired parallel (left) and normal (right) to fractures, respectively. Scattering is present within 0-1500m in X- and Y-offset, during the time period between 0.6-1.2s.

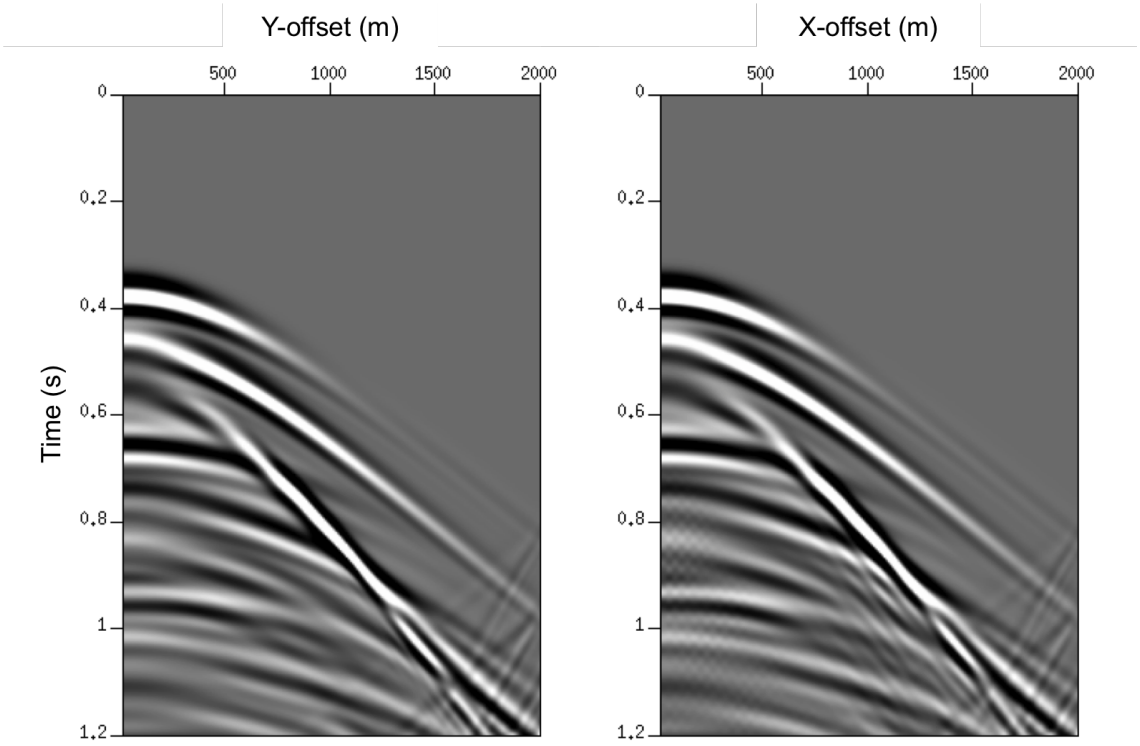

Figure 3.12: Shot records acquired from fracture model with varying spacing along the Y- and X- axes, respectively, i.e., the gathers acquired parallel (left) and normal (right) to fractures, respectively. Scattering is present within 0-1500m in X- and Y-offset, during the time period between 0.6-1.2s.

From the above results, I found that the equally spaced fractures give us regular patterns due to the constructive and destructive interference. The fracture length variation reduced this interference and tended to eliminate clear scattering patterns. Therefore, I changed the fracture distribution into arrays of fractures with different lengths. In this model, fractures are varied laterally along the X-axis, with fracture density of $1.2e-5$ and $2.4e-5$ alternatively occurring six times. The fracture length is $100m$. Fracture spacing is $5m$ when fracture density is $1.2e-5$. Fracture spacing is $10m$ when fracture density is $2.4e-5$. Figure 3.13 shows examples of shot records acquired parallel and normal to fractures. The shot gather from this model shows combined results from both equally spaced fractures and fractures with different spacing. Although I can conclude from the results that equally spaced fractures gives us a clear pattern in scattering, it does not indicate that the total scattering is more in this case compared to the other cases. More detailed discussions are presented in the following section.

3.4 Discussion

The geometrical details of the reference model with equal spacing and the model with varying fracture length are shown in Figure 3.14a. The shot gathers were collected at slices shown in the geometrical details. I selected the zero-X-offset slice (S1) and 500m-X-offset slice (S3) to investigate the effect of fracture spacing, respectively. Figure 3.14b and 3.14c show the shot gather at zero-X-offset for the reference model and the model with varied fracture length. The comparison indicates

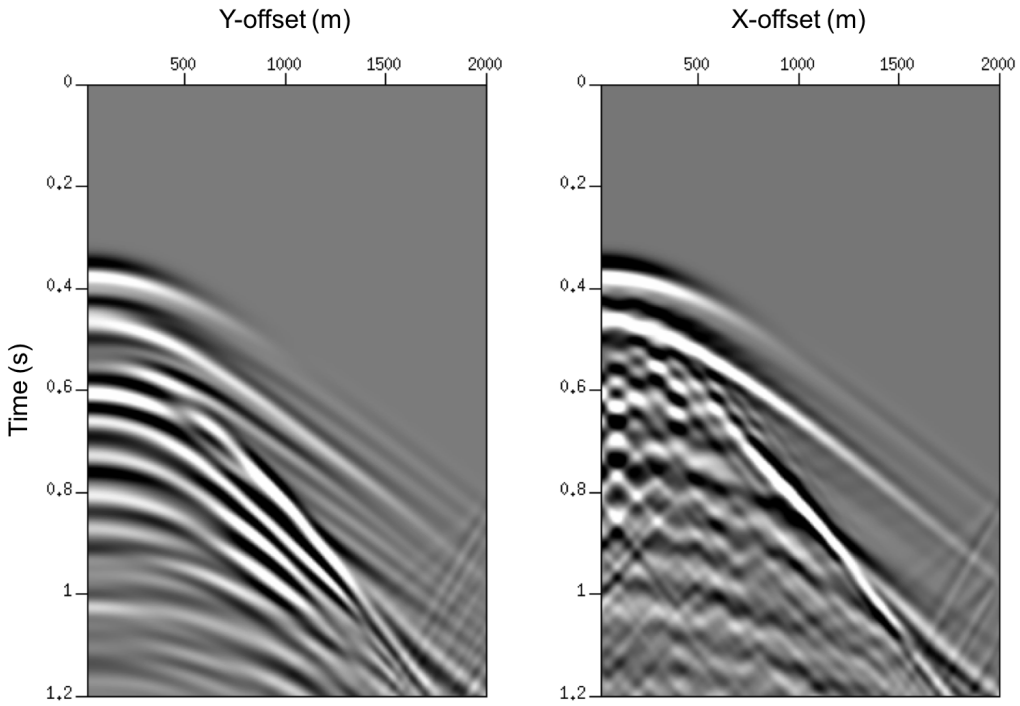

Figure 3.13: Shot records acquired from fracture model with varying fracture density along the Y- and X- axes, respectively, i.e., the gathers acquired parallel (left) and normal (right) to fractures respectively. Scattering is present within 0-1500m in X- and Y-offset, during the time period between 0.6-1.2s.

that the scattered wavelength is shorter for the reference with equal fracture spacing. The shot gathers at 500m-X-offset for the reference model and the model with varied fracture length are shown in Figure 3.14d and 3.14e, respectively. I observe that the magnitude of the scattered energy is larger in the case of the reference model. I compare the results in detail as follows. As shown in Figure 3.15a and 3.15b, there is less scattering for the model with varying fracture length compared to the reference model. This is most likely due to the interference between reflected waves from long and short fractures. For receivers located away from the middle plane, less interference compared to the reference model is observed as expected because the difference in fracture length reduces. Therefore, wave interference reduces, which leads to a similar amount of scattering as observed in the reference model as shown in Figure 3.15c and 3.15d.

Figure 3.16 shows the shot gather for slices of zero (S1), 300 m (S2), and 500 m (S3) away from the center in the x-direction indicated in the schematics as shown in Figure 3.14. Because the receiver location is away from the source, less scattering was observed as the difference in fracture length reduces. Overall, the effect of fracture length was observed in terms of wave interference. With the presence of different lengths of fractures, the constructive/destructive interference reduces scattering in comparison with the case with constant fracture length.

In Figure 3.17, I show the comparison between results from the model with $5m$ fracture spacing and those from the reference model. In Figure 3.17b and 3.17c, I find little scattering after reducing fracture spacing. This is due to the fact that the reduced fracture spacing is much smaller than the seismic wavelength. In this

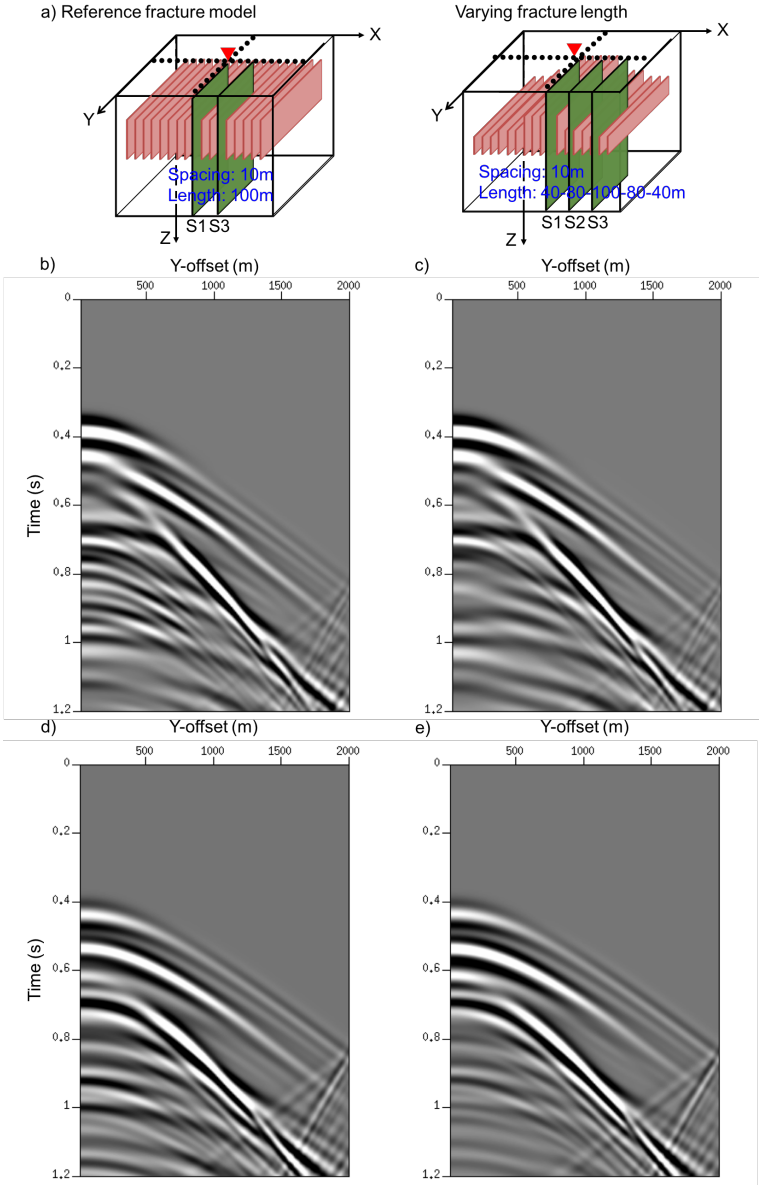

Figure 3.14: Shot gather comparison between the reference model and the model with varied fracture length: (a) geometrical details. S1 denotes zero-X-offset slice; S2 denotes 300m-X-offset slice; S3 denotes 500m-X-offset slice; (b) shot gather at zero-X-offset slice (S1) for the reference model; (c) shot gather at zero-X-offset slice (S1) for the model with varied fracture length; (d) shot gathers at 500m-X-offset (S3) for the reference model; (e) shot gathers at 500m-X-offset (S3) for the model with varied fracture length.

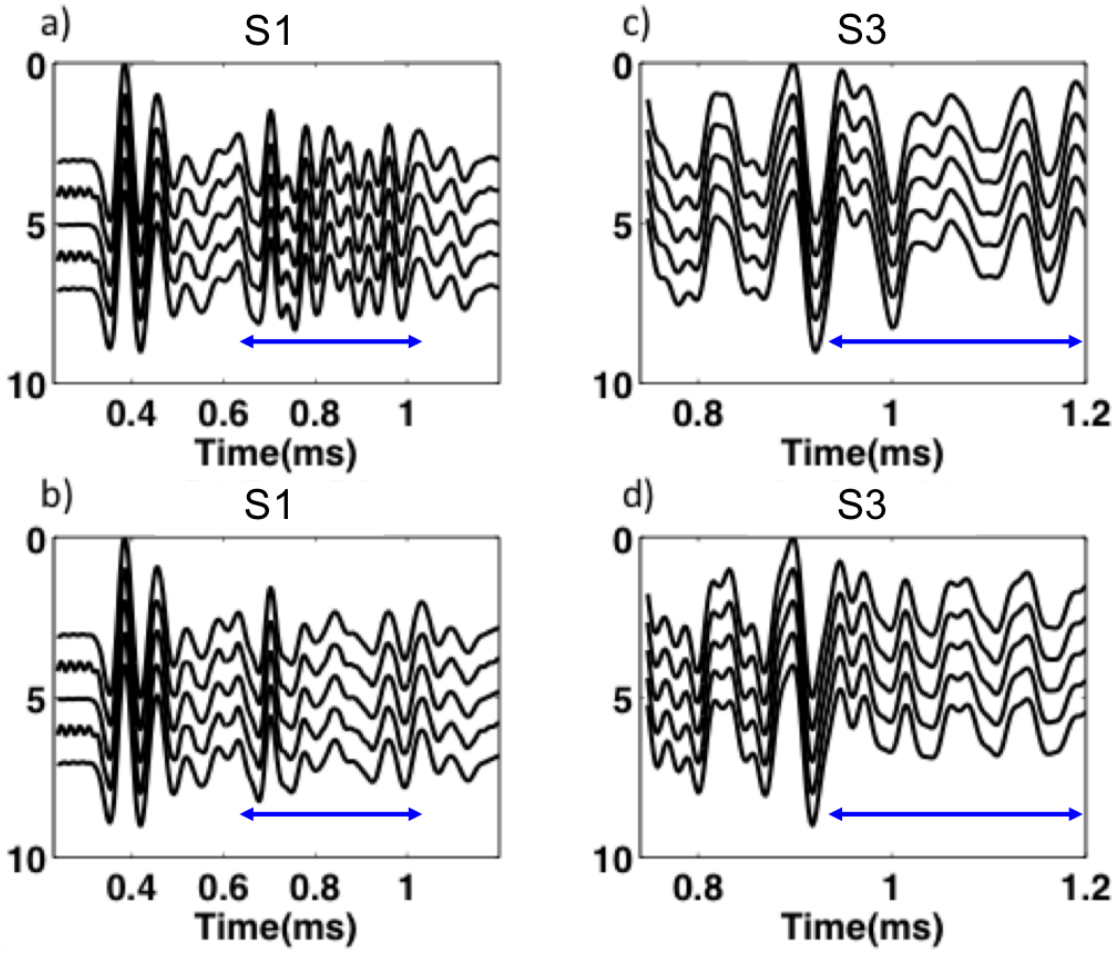

Figure 3.15: Waveform comparisons between the reference model and the model with varying fracture length at near zero-Y-offset of selected sections: (a) S1 in the reference model; (b) S1 in the model with varied fracture length; (c) S3 in the reference model; (d) S3 in the model with varied fracture length. The blue arrow indicates the time range within which the scattering occurs.

case, the fractured medium is equivalent to a horizontal transverse isotropic (HTI) medium. The reduction in compliance perpendicular to the fracture direction causes significant phase shifts in S-waves, which contributes to the change in amplitude as shown at the time range indicated by the blue arrows in Figure 3.17d and 3.17e.

I also compare the results from the reference model and the model with varying fracture density as follows. The geometrical details are shown in Figure 3.18a. I show the shot gather at zero-X-offset and 500m-X-offset in Figure 3.18b - 3.18e for both models. The shot gathers indicate that the wavelength of the scattered wave is longer than that for the reference model. This is possibly due to the constructive/destructive interference caused by the fracture density variation. From receivers located on the zero-X-offset slice, most of the reflected waves have effects on the recorded waveforms that amplify the interference effect as shown in Figure 3.19a and 3.19b. In the 500m-X-offset slice, the scattering is less significant than at zero-X-offset as shown in Figure 3.19c and 3.19d.

3.5 Conclusions

I have implemented an explicit interface scheme for modeling elastic wave propagation in 3D fractured media. The scheme explicitly treats each 2D non-planar fracture without using equivalent medium theories. The fractures are assumed to have vanishing width, and Schoenberg′s linear slip displacement-discontinuity model is used to describe the wave behavior across them. Because of the discretization of tetrahedrons, arbitrarily shaped 2D non-planar fractures can be accurately incorporated into the numerical mesh.

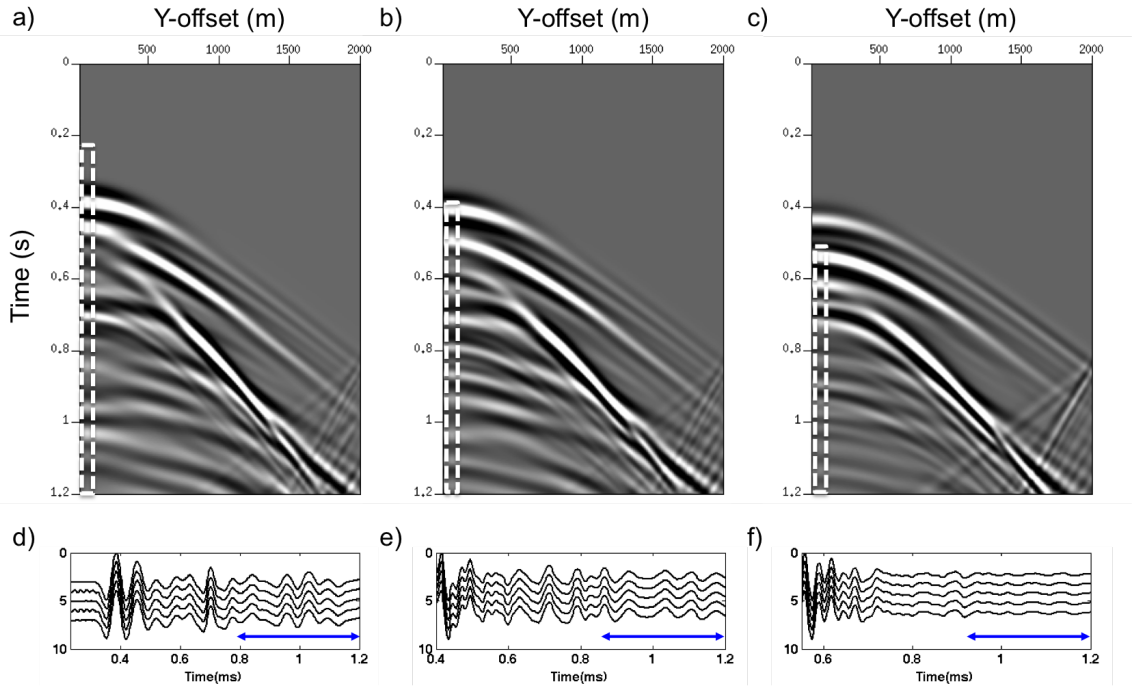

Figure 3.16: Shot gathers and waveforms of selected sections for the model with varied fracture length: (a) shot gather at zero-X-offset slice (S1); (b) shot gather at 300m-X-offset slice (S2); (c) shot gather at 500m-X-offset slice (S3); (d) waveforms near zero-Y-offset of S1 (location of traces are also highlighted by dashed line in (a)); (e) waveforms near zero-Y-offset of S2 (location of traces are also highlighted by dashed line in (b)); (f) waveforms near zero-Y-offset of S3 (location of traces are also highlighted by dashed line in (c)). The blue arrow indicates the time range within which the scattering occurs.

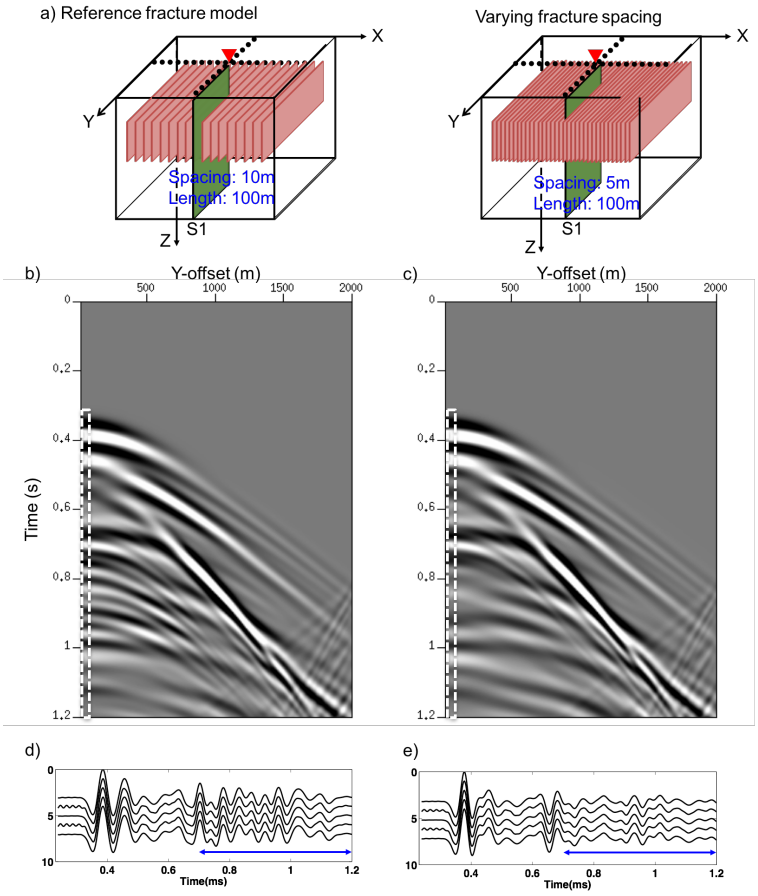

Figure 3.17: Shot gather and waveform comparisons between the reference model and the model with varied fracture spacing: (a) geometric details; (b) shot gather at zero-X-offset slice (S1) for the reference model; (c) shot gather at zero-X-offset slice (S1) for the model with varied fracture spacing; (d) waveforms near-Y-zero offset of S1 in the reference model (location of traces are also highlighted by dashed line in (b)); (e) waveforms near zero-Y-offset of S1 in the model with varied fracture spacing (location of traces are also highlighted by dashed line in (e)). The blue arrow indicates the time range within which the scattering occurs.

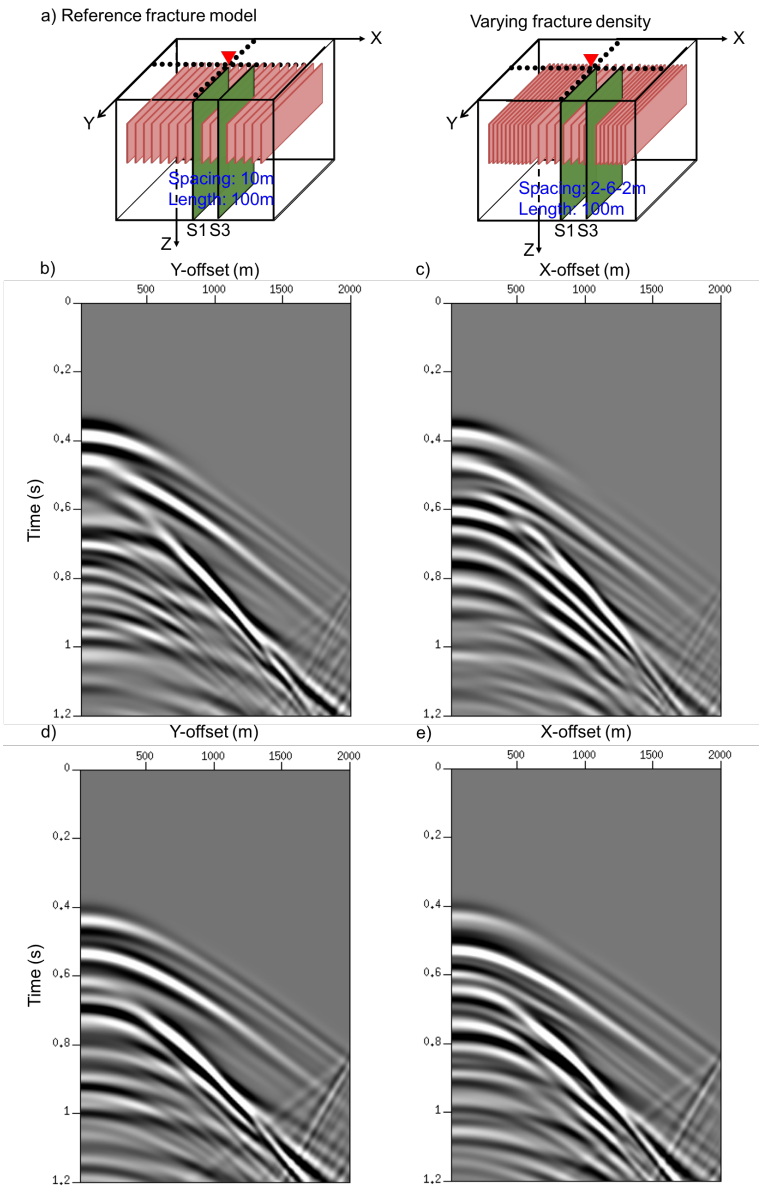

Figure 3.18: Shot gather comparison between the reference model and the model with varied fracture density: (a) geometric details; (b) shot gather at zero-X-offset slice (S1) for the reference model; (c) shot gather at zero-X-offset slice (S1) for the model with varied fracture density; (d) shot gathers at 500m-X-offset (S3) for the reference model; (e) shot gathers at 500m-X-offset (S3) for the model with varied fracture density.

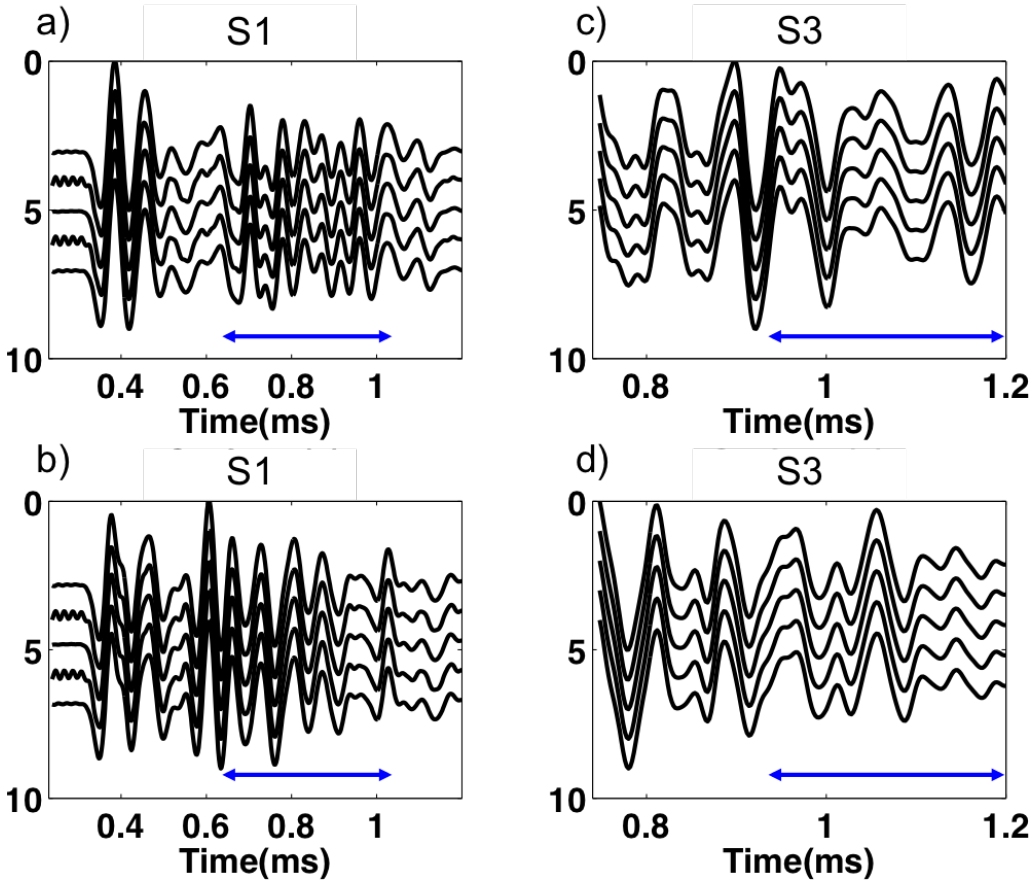

Figure 3.19: Waveform comparisons between the reference model and the model with varying fracture density at near zero-Y-offset of selected sections: (a) S1 in the reference model; (b) S1 in the model with varying fracture density; (c) S3 in the reference model; (d) S3 in the model with varying fracture density. The blue arrow indicates the time range within which the scattering occurs.

The implemented integral approach is flexible for incorporating fractures using only a small number of additional nodes (equivalent to the number of discretized grid points on the fractures). I compared the shot records corresponding to changes in the fracture length, spacing and density in the fracture models. From the vertical displacement data, I found that the tangential compliance of the fractures have significant effects on wave propagation. With non-uniform distributions of fracture length and density, strong interference is often observed. Constant fracture length and spacing tend to reduce such interference and lead to significant scattering effects. The scattering is the results of combined effects of reflection and interference. Hence, it is difficult to evaluate its extent. Therefore, I need a method to quantify this extent. In the next chapter, I will use the scattering index method to quantify the degree of scattering for different fracture distributions.

Chapter 4

Effect of fracture properties on wave scattering

The integral-based numerical method offers an explicit way to model fractures in elastic media. The algorithm has been described in detail in Chapter 3. Here I demonstrate an application of the algorithm and study the effect of variation of fracture properties on seismic data. A quantification method is necessary to describe the extent of wave scattering. I apply the scattering index proposed by Willis (2006) for this purpose. In this Chapter, I show a variety of synthetic seismograms for varying fracture properties attempt to quantify the effect of fracture spacing, patterns, and azimuth using the scattering index (SI) method. Using this I establish a relationship between fracture parameters and the induced wave scattering. I hope that these results will provide a basis for future inversion algorithms for fracture characterization.

4.1 Scattering index method

Although the results reported in chapter 3 demonstrate the effects of different fracture patterns qualitatively, it is still difficult to quantify those using single shot gathers. Willis et al. (2006) first proposed the scattering index (SI) method to describe the effect of fracture spacing on scattering. In their method, the SI value describes the extent of scattering by quantifying the amount of ringing in a trans-

fer function relating the wavelet before and after propagation through a fractured medium.

The transfer function represents the ability of a fractured layer to generate scattered energy. With surface seismic reflection traces, a transfer function quantifies the change of a seismic wavelet before and after propagating through a fractured layer. The transfer function describes how the amplitude and phase of a particular signal are altered by a linear filter. The fractured layer can be considered to be a filter, where the input signal is the reflection from the top of the fractured layer. The fractured layer transforms this signal into an output, which is the reflection at the base of the fractured layer. Thus, this problem can be written in a convolutional form follows:

$$i(t) * f(t) = o(t), \tag{4.1}$$

where $f(t)$ is the time domain transfer function, $i(t)$ is the input signal, $o(t)$ is the output signal, and $*$ represents convolution. Thus to obtain the transfer function, $f(t)$, Weiner devonvolution is performed on $o(t)$ using $i(t)$. The transfer function $f(t)$ completely describes the properties of the medium between the top and bottom of the fractured medium. With the transfer functions for a full range of azimuth of a fracture system, the scattering index can be used to quantify the amount of ringing in transfer functions. The SI is defined as

$$\mathbf{SI} = \sum_{i=0}^{m} |t_i| i^n, \tag{4.2}$$

where i is the time lag in the transfer function, t_i is the transfer function magnitude at lag i, n is an exponent, and m is a lag where the transfer function magnitude vanishes. This expression gives more weight to the transfer function at the large lag times than the small lag times. The scattering index approaches zero if there is no scattering.

4.2 Effect of fracture spacing, density, height

In the present study, I implement this method using the waveforms recorded from receivers distributed on the top surface of the model. Figure 4.1a shows the model details with the locations of the source and receivers. Figure 4.1b shows the contour plot of the scattering index from the receivers. Because our model is symmetric with respect to the central plane, I only show a quarter of data from the top surface. The area selected for the scattering index is within 400m-offset in both X and Y directions to avoid the boundary effect. In this case, I varied the ratio between fracture spacing and wavelength by fixing the fracture spacing at 40m while varying frequency from 5Hz to 25Hz. Figure 4.2 shows the displacement wavefield results for each case.

In Figure 4.2, I observe that the amount of scattering increases as the ratio between fracture spacing and wavelength increases. Frequency increases from 5 to 25 Hz from Figure 4.2a to 4.2i. The ratio between fracture spacing and wavelength increases from Figure 4.2a to 4.2i as does the scattering. However, when I examine results from the contour plots (Figure 4.3) from the SI on the top surface, I note that the total amount of scattering is not proportional to the ratio between fracture spacing

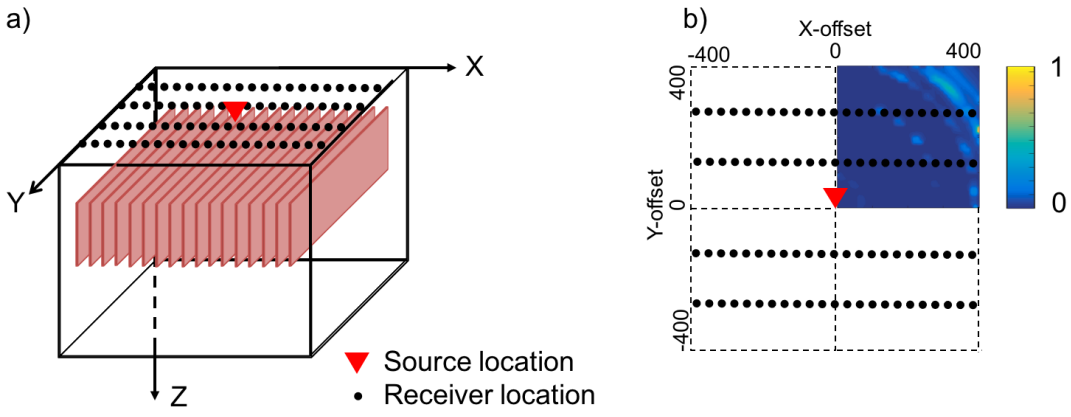

Figure 4.1: a) model details, b) contour plot of SI on top surface for frequency of 7.5Hz (quarter view).

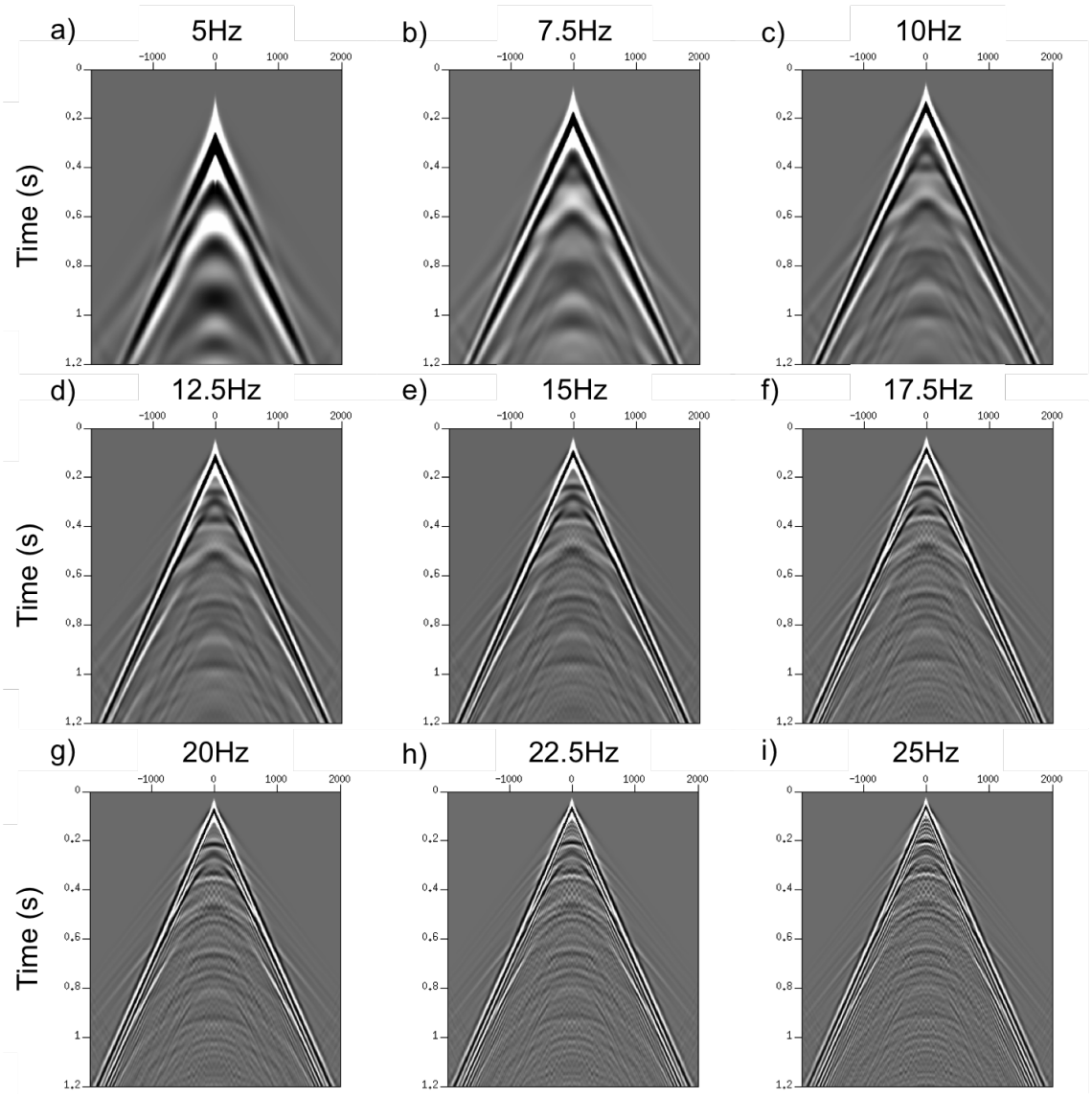

Figure 4.2: Shot gathers for different frequencies recorded at zero Y-offset. Horizontal axes are X-offset in meters. Vertical axes are time in seconds. From a)-i), I varied the ratio between fracture spacing and wavelength by fixing the fracture spacing at 40m while varying frequency from 5Hz to 25Hz.

and wavelength. From these results, I notice that the SI shows a ring type pattern. As the ratio increases I observe an increase in the number of rings with higher intensity. However, when the ratio reaches a certain value, this pattern is lost. Therefore, I use the mean SI value of the entire contour plot. This mean value indicates the overall scattered energy through the entire domain; the mean SI is plotted against each ratio in Figure 4.4. I observe that the SI increases first when the ratio increases from 0.067 to 0.267. After reaching the peak, it shows a rapid drop in SI values.

With this result, I present a relationship between scattering and fracture spacing/wavelength ratio. In practice, if the only unknown parameter to be characterized is the spacing of the fracture arrays, then I can use the obtained SI vs fracture spacing/wavelength ratio curve to estimate its corresponding values. This result also shows that as the fracture spacing increases, the scattering increases to a peak value then decreases sharply. This trend can be attributed to the interference between scattered waves from individual fractures. When the fracture spacing is small, the interference increases as the spacing reduces, producing a significant amount of wave scattering. However, as the spacing exceeds a certain level, the area affected by this interference reduces rapidly causing a significant drop in the scattering index. Therefore, it gives an indication that the correlation between fracture spacing and scattering index should be established for different ranges.

4.3 Azimuthal effects of fractures

To investigate the azimuthal effect, I setup up a model with variations of source-to-fracture azimuth and an explosive source that generates a spherical pressure

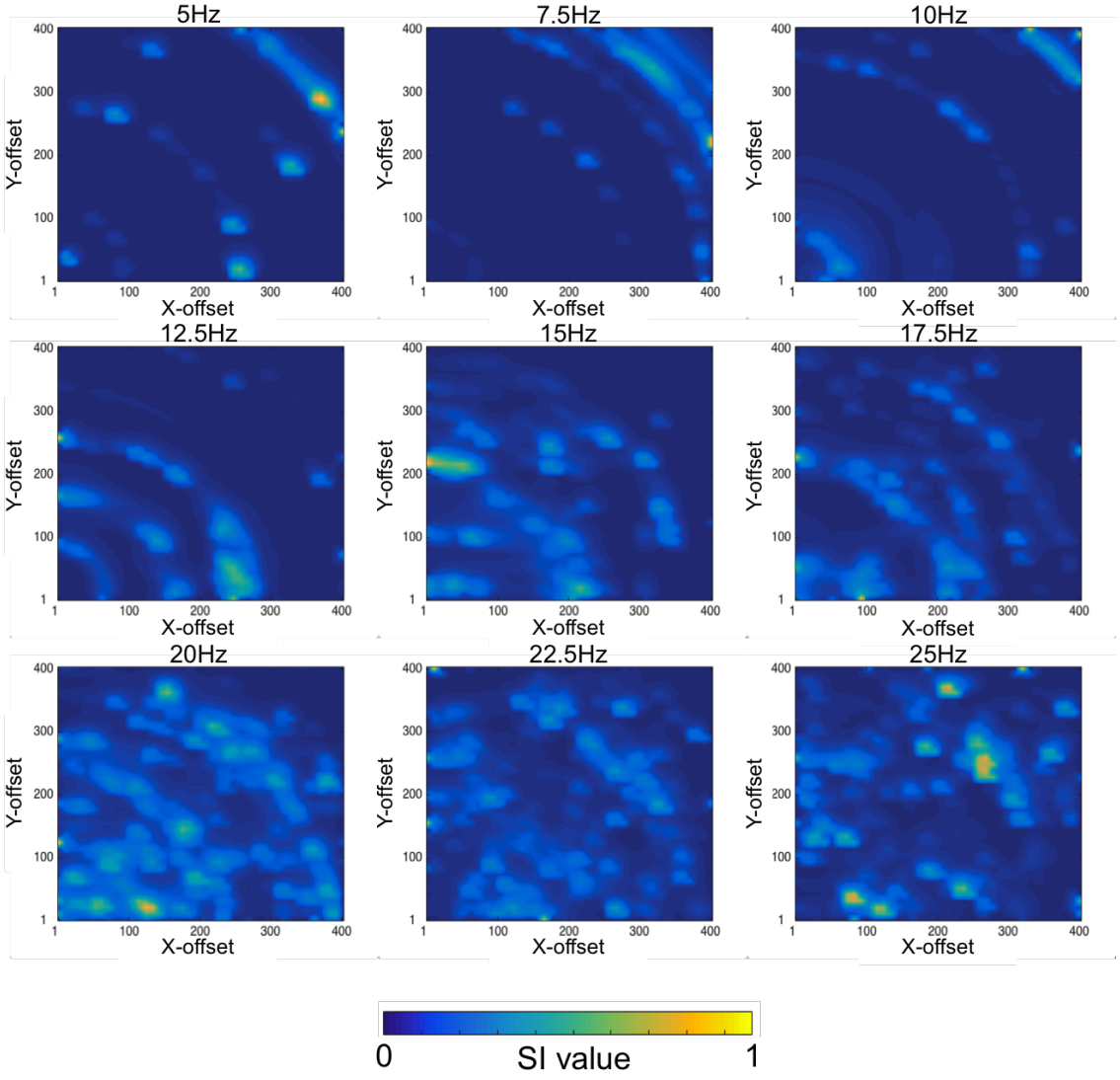

Figure 4.3: Contour plots for different ratio between fracture spacing and wavelength by fixing the fracture spacing at 40m while varying frequency from 5Hz to 25Hz. The color in each plot indicates the normalized SI value.

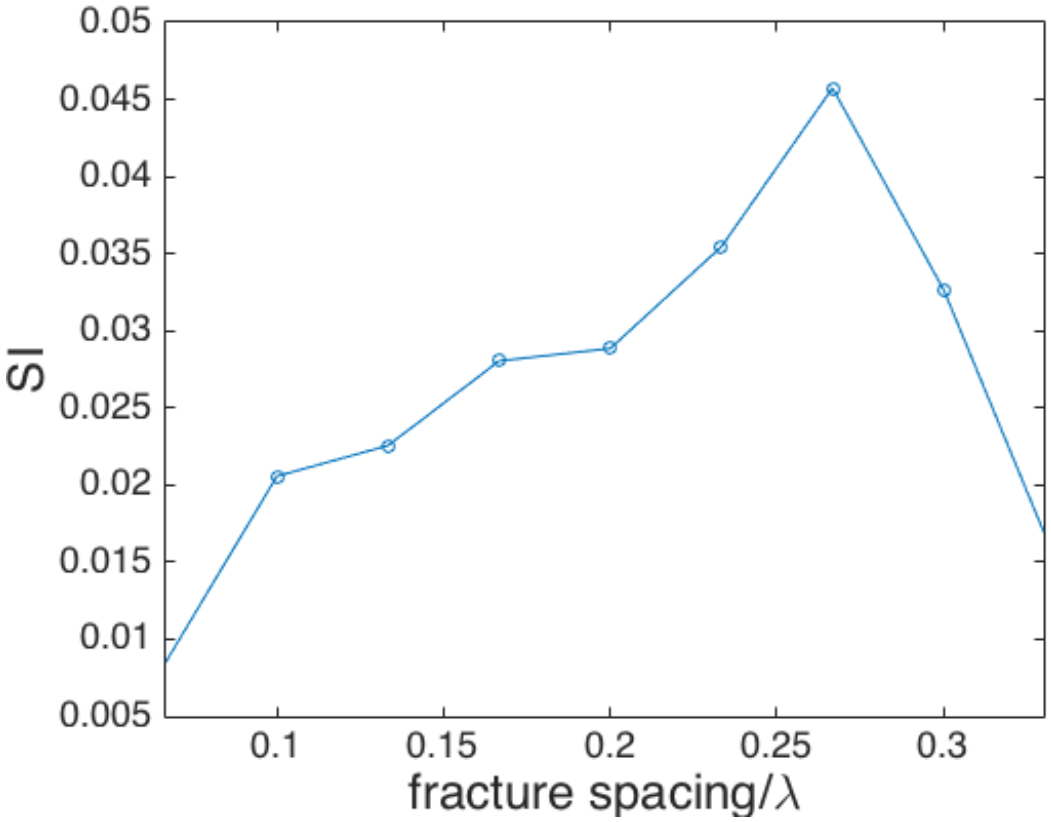

Figure 4.4: SI vs. ratio between fracture spacing and wavelength.

wave-front. The fractures with different properties are placed in the center of the model to maximize the wave-scattering effects. The model geometries are shown in Figure 4.5. The model in Figure 4.5 contains a vertical fracture with 200m height located at the center indicated by the black bar. The red stars denote the source locations at seven source-to-fracture azimuths (0°, 15°, 30°, 45°, 60°, 75°, 90°) . The sources are $500m$ away from the fracture center for all source azimuths with receivers over the entire domain.

4.3.1 Effect of incident angles on single fractures

The displacement wavefields are shown in Figure 4.6. Here, I observe that the wavefront is bent at the location where a line connects the source to the center of the fracture. The bending of the wavefront is caused by the time delay of waves propagating through the fracture. The bending location of the wavefront rotates as we change the source azimuth. The time delay in 0° source azimuth is the most significant. The time delay gradually reduces from 0° source azimuth to the 90° source azimuth. Scattering is observed at both corners of the fracture for almost all cases. On the other hand, because I selected a relatively large compliance value of $1.8 * 10^{-9} mPa^{-1}$ for the fracture, the amount of reflection wave energy is substantial, which gives rise to significant scattering between the source and the fracture line.

Next I quantify the seismic scattering using the scattering index method of Willis et al. (2006). Figure 4.7 shows the scattering index contour plots for seven source azimuths from 0° to 90°. Each value in the scattering index contours is obtained using each trace from the entire receiver field. The azimuthal effect is clearly

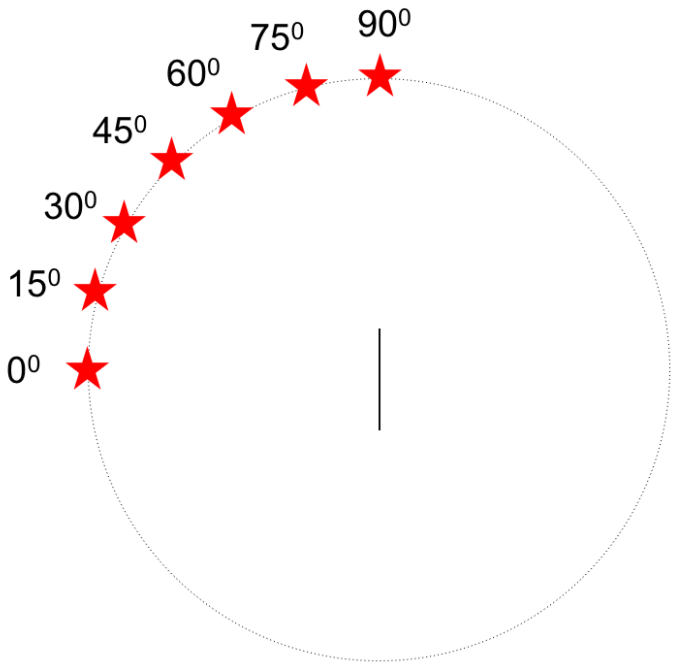

Figure 4.5: A single fracture model containing a vertical fracture with 200m height located at the center, which is indicated by the black bar. The red stars denote the source location at seven incident angles. The sources are $500m$ away from the fracture center for all seven angles. The source to the left of fracture is the 0° incident angle. The source above the fracture corresponds to the 90° incident angle.

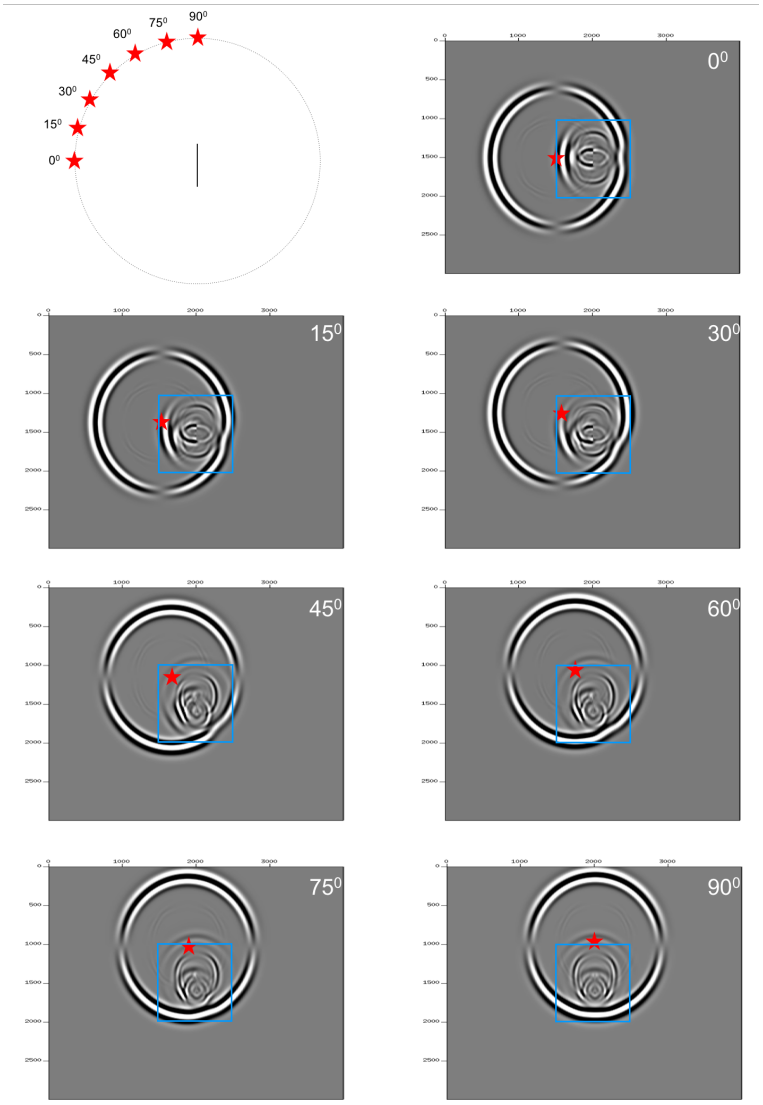

Figure 4.6: Wavefields for a single fracture with source to fracture azimuth varying from 0 to 90 degrees. The source-to-fracture azimuths are labeled on the upper right corner of each wavefield. The red stars indicate the source location. The blue boxes indicate the area selected for scattering analysis.

observable on the scattering index contours. I observe that most of the scattering occurred between the source and the line fracture for 0° source azimuth. However, for 90° source azimuth, most of the scattering occurred on the transmission side. The centroid of the scattering seems to rotate as the azimuth changes. To show the extent of fracture with varying azimuth, I selected receivers at full azimuth θ distributed about 500m away from the center of the fracture shown as the red dashed circle. The scattering indices at these locations are then plotted in polar coordinate in Figure 4.8.

In Figure 4.8, I show the scattering index values with θ from the location of the receivers. The radius represents the values of SI. The angle in polar coordinates represents the full azimuth of the fracture. The connected line shows that the scattering index values are indeed high in the area between the source and fracture. More interestingly, there seems to exist peaks in these plots indicating that the centroids of these patterns are indeed shifted with changes in azimuth.

To describe the wave scattering for each case, an average index is needed. I then seek the definition of mean values in statistics. This mean value is obtained using the first moment of the scattering index in terms of azimuth angle. Based on the theory of the center of mass (Mancosu, 1999), we obtain the weighted central azimuth angle using :

$$\theta_w = \frac{\int_0^{2\pi} f(SI * \theta) d\theta}{\int_0^{2\pi} f(SI) d\theta}, \tag{4.3}$$

where f is a function of SI in terms of θ.

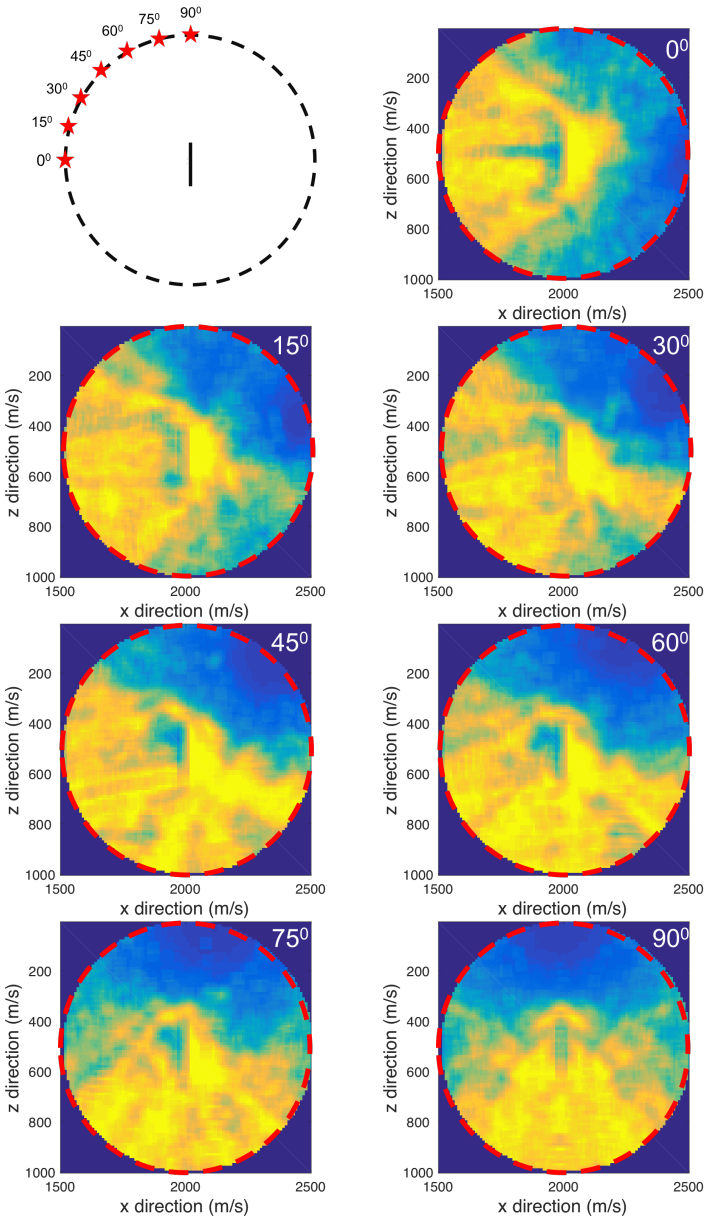

Figure 4.7: SI contour plots for a single fracture with source to fracture azimuth varying from 0 to 90 degrees. The source-to-fracture azimuths are labeled on the upper right corner of each contour plot. The red circles indicate the full receiver azimuth 500m away from the center of fracture.

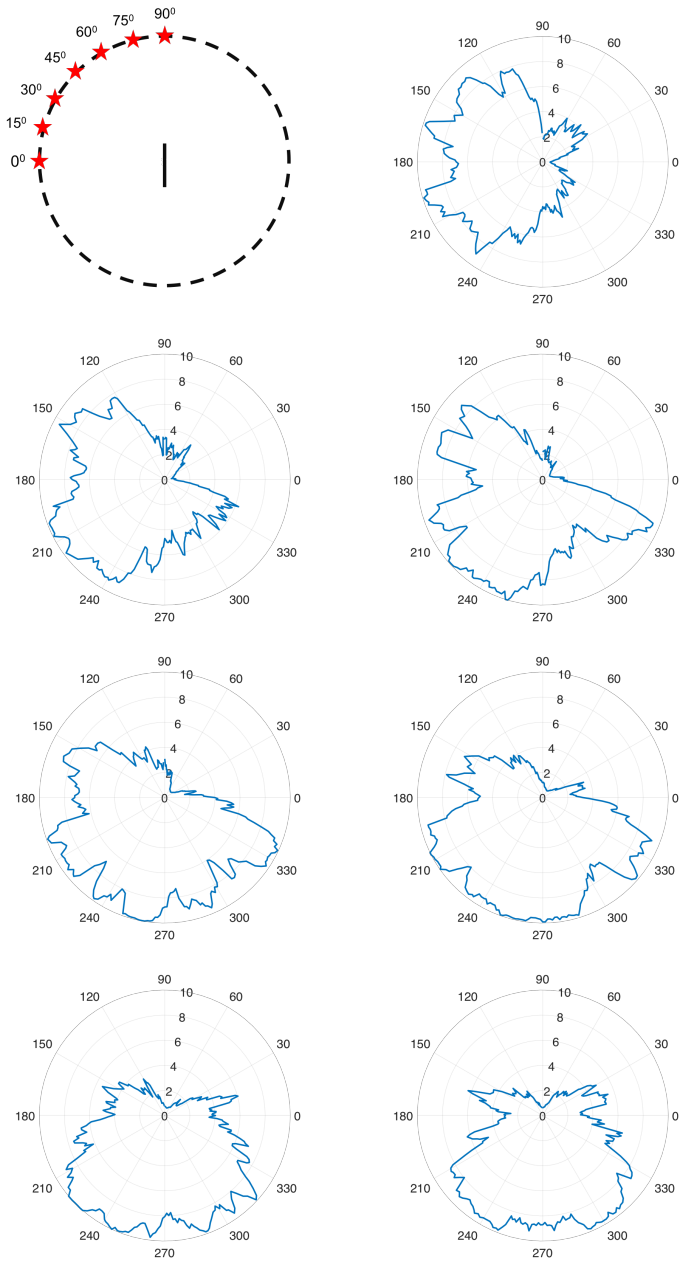

Figure 4.8: SI polar plot for a single fracture with source-to-fracture azimuth varying from 0 to 90 degrees. The SI values are obtained from the full receiver azimuth 500m away from the center of fracture.

If I plot a polar SI for all seven source azimuths together in Figure 4.9a, I notice that the centroid for each SI polar plot seems to rotate with the source azimuth. To confirm this, I plot the average SI against the weighted θ angle from each polar SI plot in Figure 4.9a in Figure 4.9b. From Figure 4.9b, I noticed that, from source azimuth 0° to 90°, the average SI values are about the same. However, the weighted θ gradually rotates from 220° to 270°. The results shown in Figure 4.9b are from one quadrant only (0° to 90°). Because of the symmetry of the model, I complete the remaining three quadrants of the results and plot them all in FIgure 4.9c. Here, I observe that all of the central angles are located around 270 degrees. This indicates that for a single fracture, the scattering indices are usually high in the direction parallel to the fracture.

4.3.2 Effect of incident angles on multiple parallel aligned fractures

Subsequently, I investigate the effect of multiple fractures on wave scattering. The fracture spacing of 40m is selected to be close to the spacing over wavelength ratio of 0.267, which should give the maximum amount of wave scattering in Figure 4.4. The wave-field results are shown in Figure 4.10. In this multiple parallel aligned fractures model, there are more distortions of the wavefront than in the previous single fracture model. The distortion is caused by the interference of the scatter wave with the first wave-front. I also observe more scattering in the reflection wavefield caused by the multiple fractures. This is due to the fact that the effective fracture compliance from the array of fractures is higher than the compliance of the single fracture. Therefore, more reflections are found, which leads to more severe interfer-

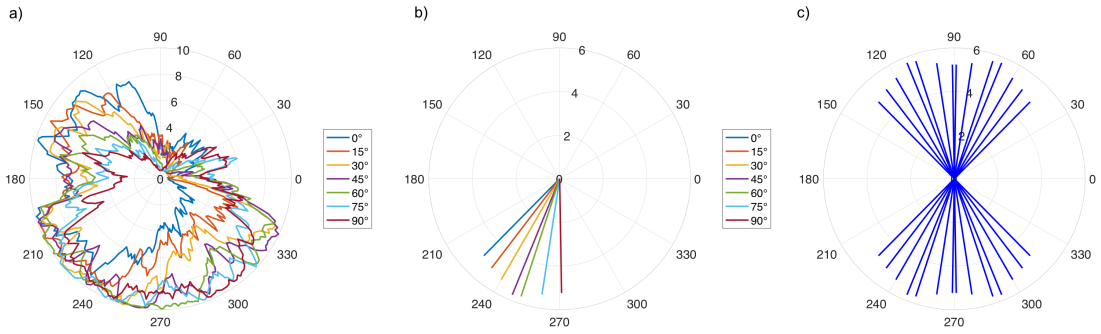

Figure 4.9: a) SI polar plot for a single fracture from seven source to fracture azimuths vary from 0 to 90 degrees. b) average SI and weighted θ in a quadratic polar plot. c) average SI and weighted θ in complete source to fracture azimuth vary from 0 to 360 degrees.

ence giving rise to enlarged areas with high scattering index values as shown in Figure 4.11.

In these contour plots, I observe much larger areas having high scattering index values than those in the single fracture model. More interestingly, I observe valley areas on the side of the array show low scattering index values. This is caused by the destructive interference in the wavefield. In addition, similarly as found in the case of single fracture, the same trend of rotation of the centroid as the azimuth angle varies. The polar plots of the scattering index values from receivers 500m away from the center of fractures are shown in Figure 4.12. The centroid of the SI shape in 0° source azimuth is between the source and the fractures. As the source azimuth rotates from 0° to 90°, the centroid of the SI shape gradually rotates counterclockwise on the transmission side of the fractures. Figure 4.12 also shows that the scattered wave passing the multiple fractures have considerable SI values.

SI polar plots from all seven source azimuths are plotted in Figure 4.13a. I then conducted the weighted average as done for the case of the single fracture from the results in a quarter of source azimuth (Figure 4.13b) and full azimuth (Figure 4.13c). I then observe that the equivalent total scattering values are around 250 degrees. This value is quite close to that of the single fracture case. However, the distribution of these locations are much dispersed compared to the previous case.

4.3.3 Effect of incident angles on intersecting fractures

Considering the direction that the average scattering index points to is close to the parallel direction of the fractures, I also investigate the effect of azimuth an-

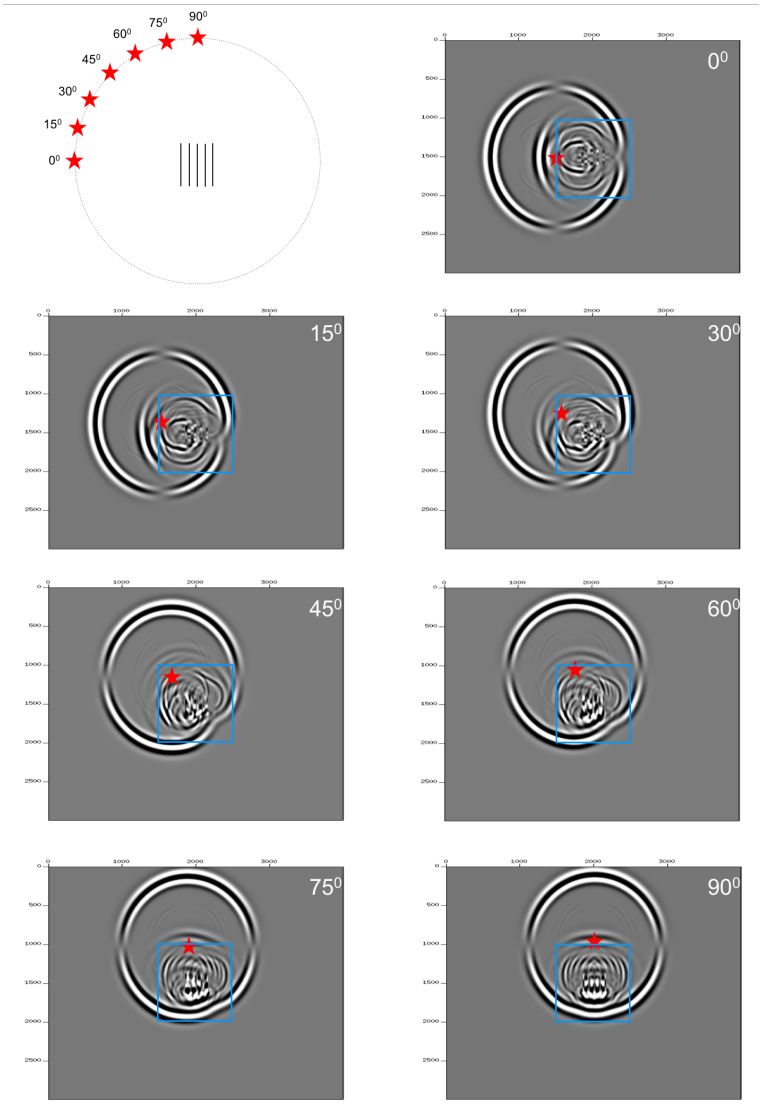

Figure 4.10: Wavefields for multiple fractures with source-to-fracture azimuths varying from 0 to 90 degrees. The source-to-fracture azimuths are labeled on the upper right corner of each wavefield. The red stars indicate the source location. The blue boxes indicate the area selected for scattering analysis.

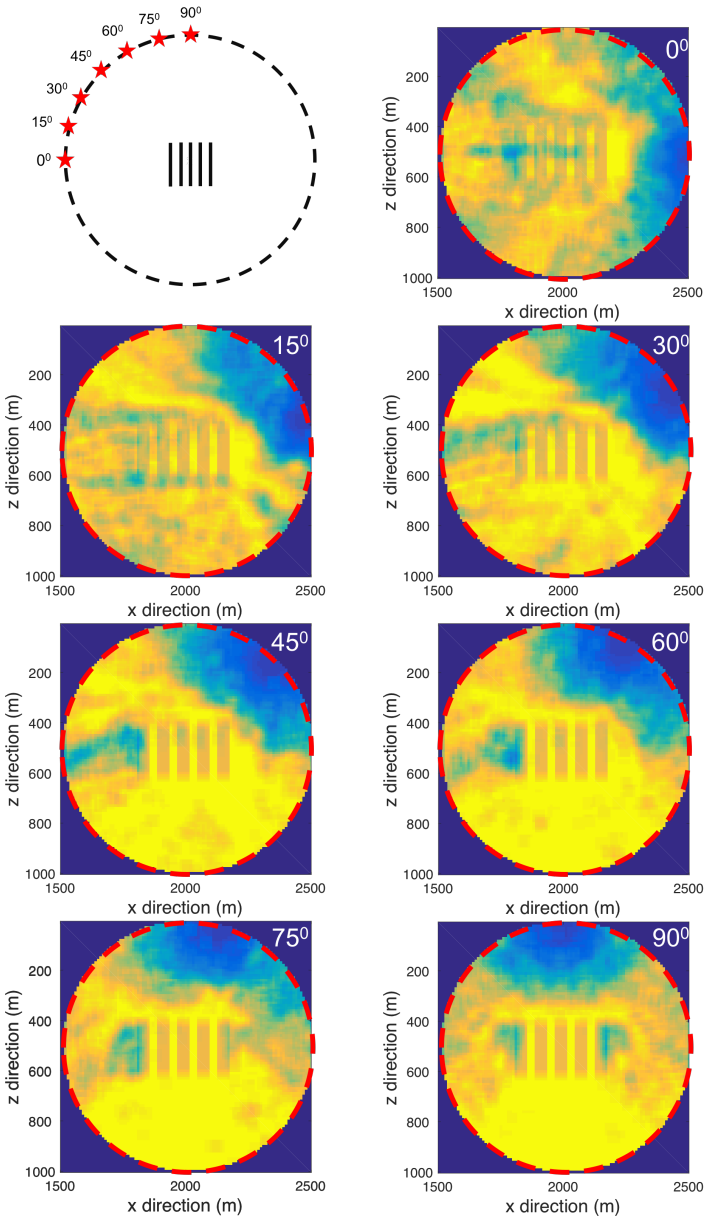

Figure 4.11: SI contour plots for multiple fractures with source-to-fracture azimuths varying from 0 to 90 degrees. The source-to-fracture azimuths are labeled on the upper right corner of each contour plot. The red circles indicate the full receiver azimuth 500m away from the center of fracture.

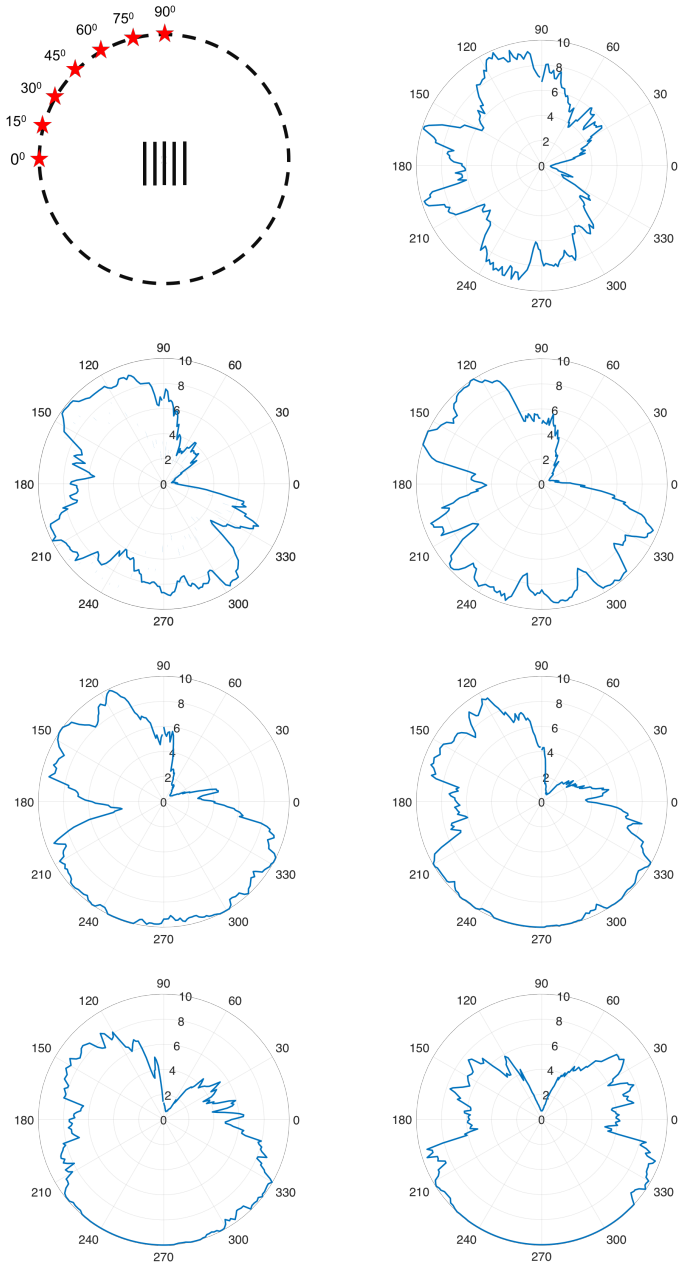

Figure 4.12: SI polar plot for multiple fractures with source-to-fracture azimuths varying from 0 to 90 degrees. The SI values are obtained from the full receiver azimuth 500m away from the center of fracture.

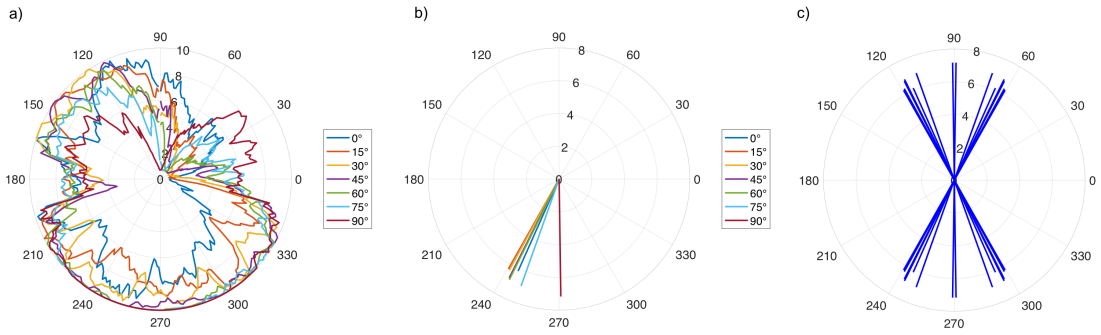

Figure 4.13: a) SI polar plot for multiple fractures from seven source-to-fracture azimuths varying from 0 to 90 degrees. b) average SI and weighted theta in a quadratic polar plot. c) average SI and weighted θ in complete source-to-fracture azimuths varying from 0 to 360 degrees.

gles on intersecting fractures. The two intersecting fractures are selected to have the same length of $200m$ to avoid the influence from different fracture length. From the displacement fields shown in Figure 4.14, I observe significant interference of the transmitted wave with the wavefront. These scattering indices are high but they appear smeared over the entire contour area (Figure 4.15). The destructive interference caused by the intersecting fractures show reduction in SI values in the vicinity of the fractures. The polar plot shown in Figure 4.16 confirms these observations. In addition, these SI polar patterns are symmetric about the axis connecting the source to the center of the fractures. Figures 4.17a and 4.17b show the overlapped SI polar plots and average SI vectors for seven source azimuths, respectively. The total vector scattering indices of full azimuth are shown in Figure 4.17c. These vectors are mainly uniformly distributed in between 240 and 300 degrees. With the intersecting fractures, the reflected and transmitted waves cast severe interference and give rise to significant scattering index values in the fractured region.

4.3.4 Effect of incident angles on multiple intersecting fractures

Next I place multiple intersecting fractures in the center of the domain. In this model, the fracture spacing is selected to be the same as that in the multiple parallel aligned fractures. The length of the horizontal intersecting fracture is the same as that in the single intersecting fracture model. In this fracture pattern, I form a compliant area that reflects most of the incoming waves in the vertical direction (90 degrees). The strong interference is found in the fractured area from the displacement fields (Figure 4.18). Both the contour and polar plots (Figure 4.19 and 4.20) in terms

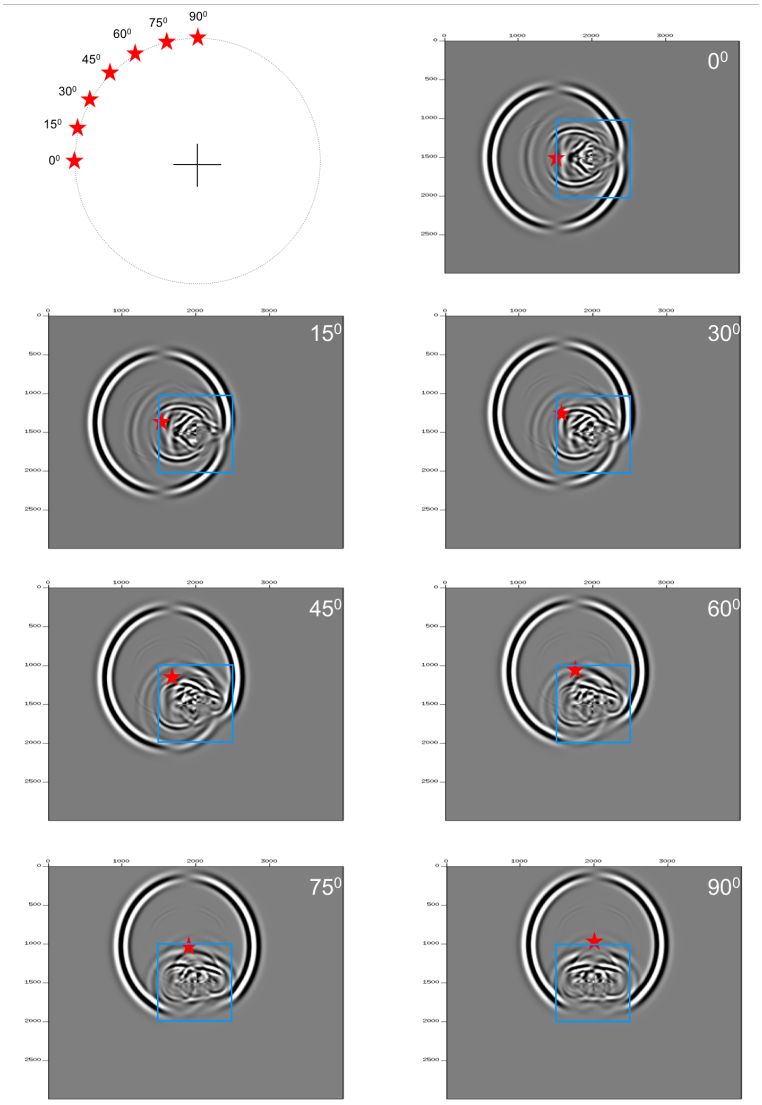

Figure 4.14: Wavefields for a single intersecting fractures with source to fracture azimuth vary from 0 to 90 degree. The source-to-fracture azimuth are labeled on the upper right corner of each wavefield. The red stars indicate the source location. The blue boxes indicate the area selected for scattering analysis.

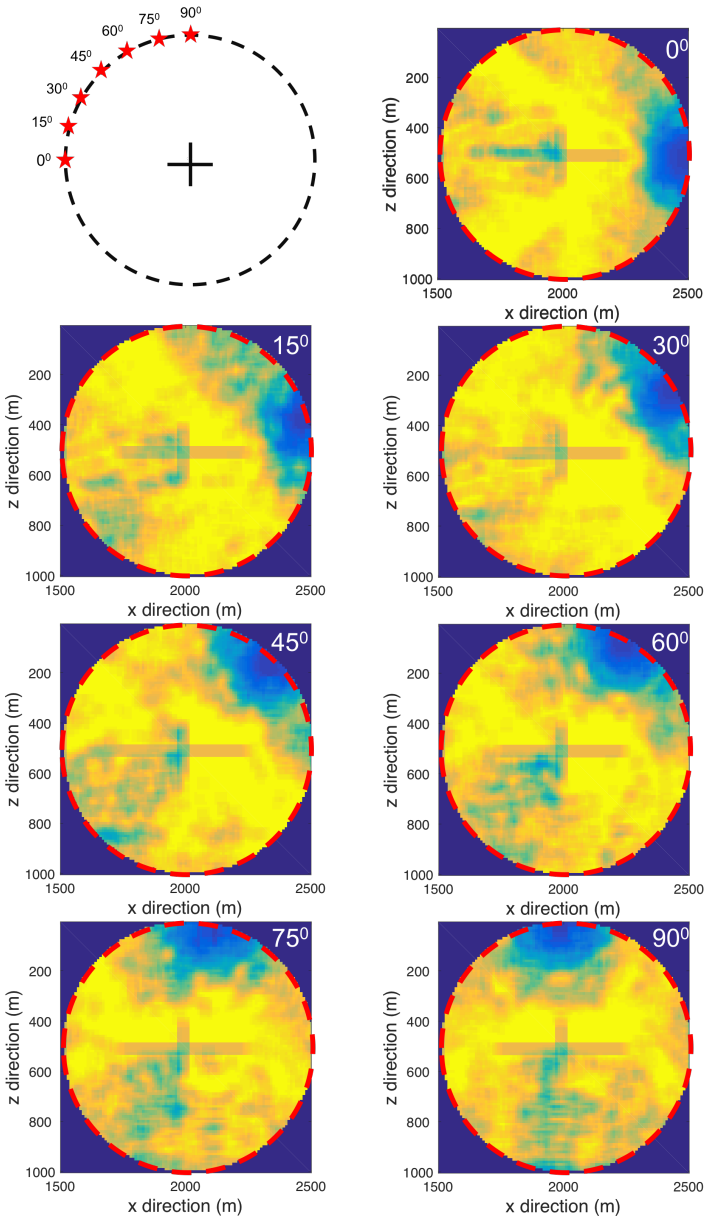

Figure 4.15: SI contour plots for a single intersecting fractures with source-to-fracture azimuths varying from 0 to 90 degrees. The source-to-fracture azimuths are labeled on the upper right corner of each contour plot. The red circles indicate the full receiver azimuths 500m away from the center of fracture.

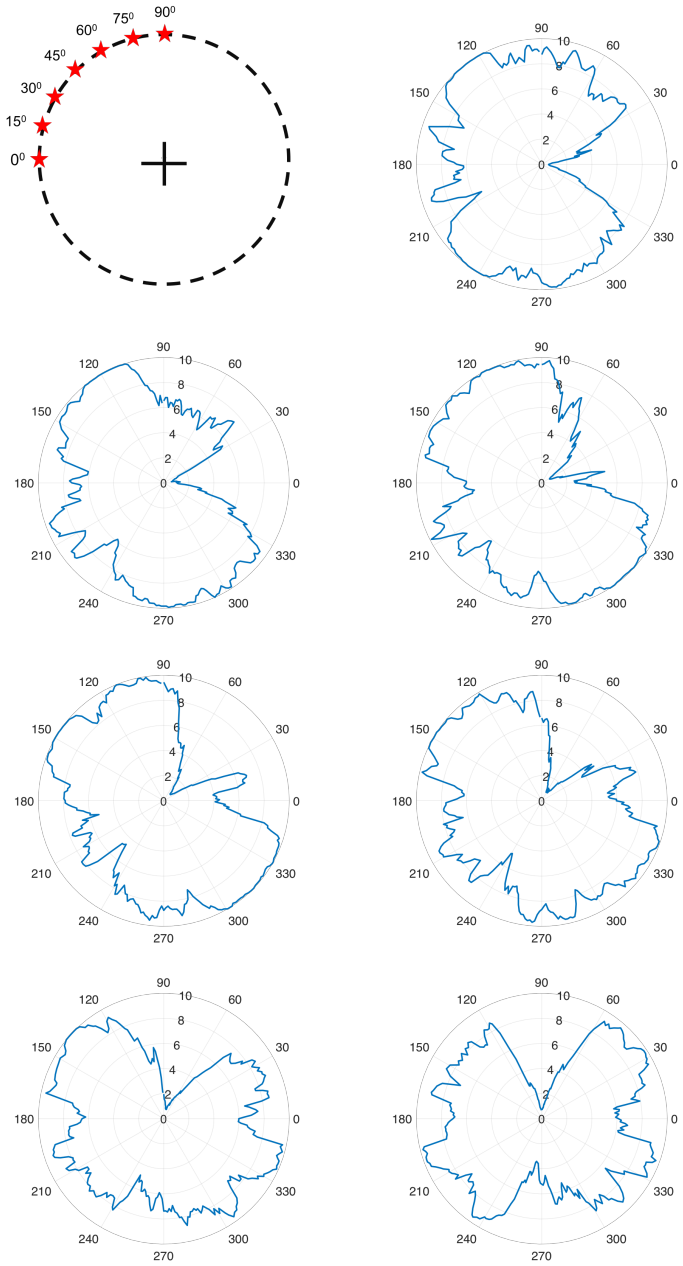

Figure 4.16: SI polar plot for a single intersecting fractures with source-to-fracture azimuths varying from 0 to 90 degrees. The SI values are obtained from the full receiver azimuths 500m away from the center of fracture.

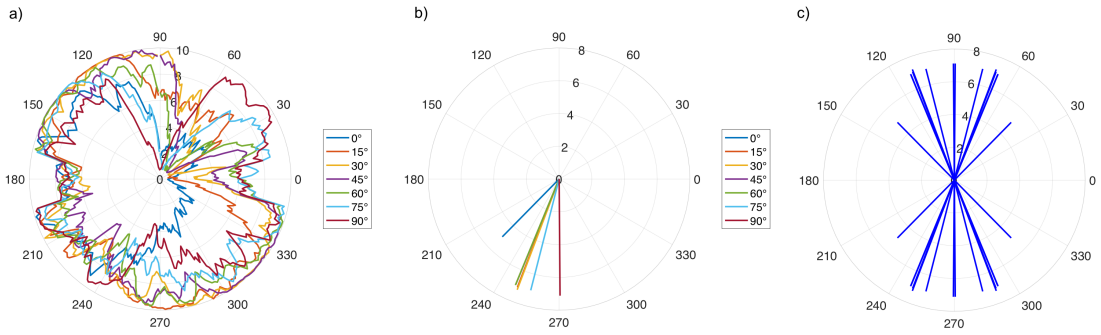

Figure 4.17: a) SI polar plot for a single intersecting fractures from seven source-to-fracture azimuths varying from 0 to 90 degrees. b) average SI and weighted theta in a quadratic polar plot. c) average SI and weighted theta in complete source-to-fracture azimuths varying from 0 to 360 degrees.

of scattering indices confirm the intensified scattering due to the array of intersecting fractures. Figure 4.21a and 4.21b show the overlapped SI polar plots and average SI vectors for seven source azimuths, respectively. The vectors of the polar plot of full azimuth are plotted in Figure 4.21c. With this particular pattern, I found the vectors are mainly distributed in between 240-300 degrees uniformly.

4.4 Correlating fracture properties, incident angles, and scattering index values

The above results show that the scattered wave often points to a direction parallel to the main fracture direction, which is determined by the direction having the highest compliance. The distribution of the fractures results in different distribution of the vectors. I then take another average for the vectors of four fracture models (figure 4.22). The average theta and SI values for four fracture models are listed in Table 1. Clearly all the average vectors are in the range between 240 and 270 degrees. By switching from single to multiple fractures, the average scattering vector increases in values but stays in the same direction. For the case of the intersecting fractures, the total scattering vector increases as the number of fracture increases. The corresponding direction shift closer to 270 degrees.

Based on these findings, it can be concluded that the overall magnitude of the scattering index is related to the compliance of the fractured region. The higher compliance gives rise to more intense scattering. The direction of the overall scattering index is then related to the anisotropy of the fractured region. The scattering direction is generally parallel to the direction of the maximum compliance matrix.

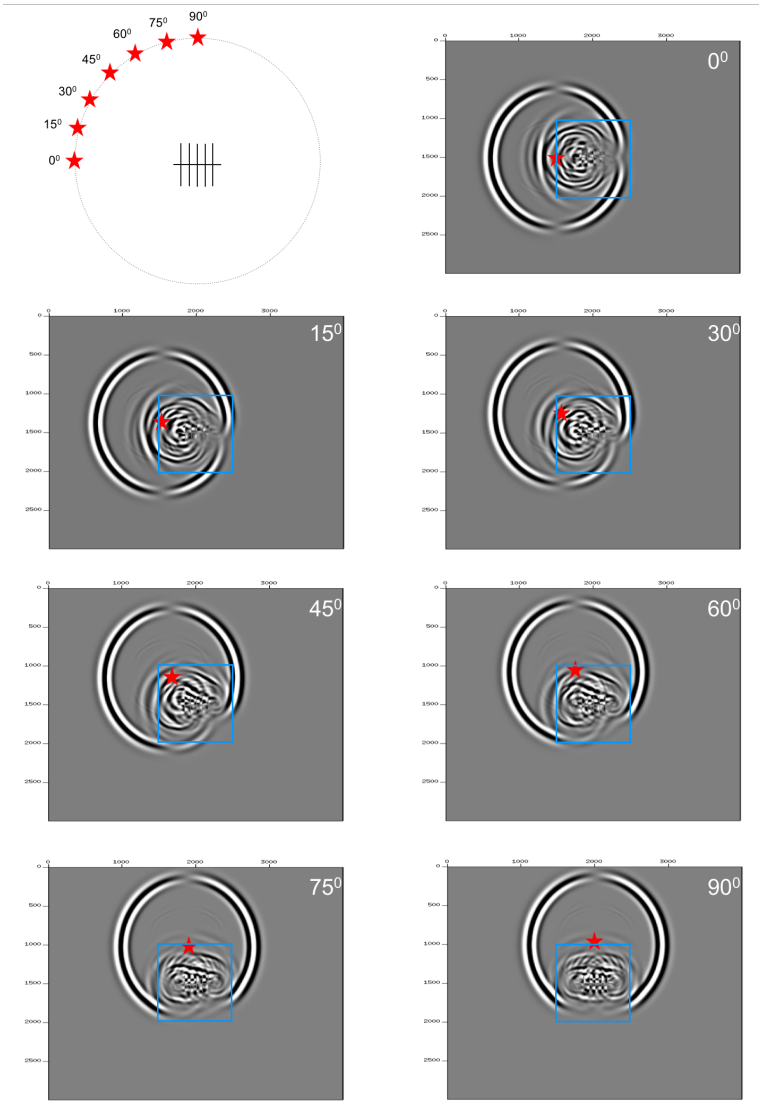

Figure 4.18: Wavefields for multiple intersecting fractures with source-to-fracture azimuths varying from 0 to 90 degrees. The source-to-fracture azimuths are labeled on the upper right corner of each wavefield. The red stars indicate the source location. The blue boxes indicate the area selected for scattering analysis.

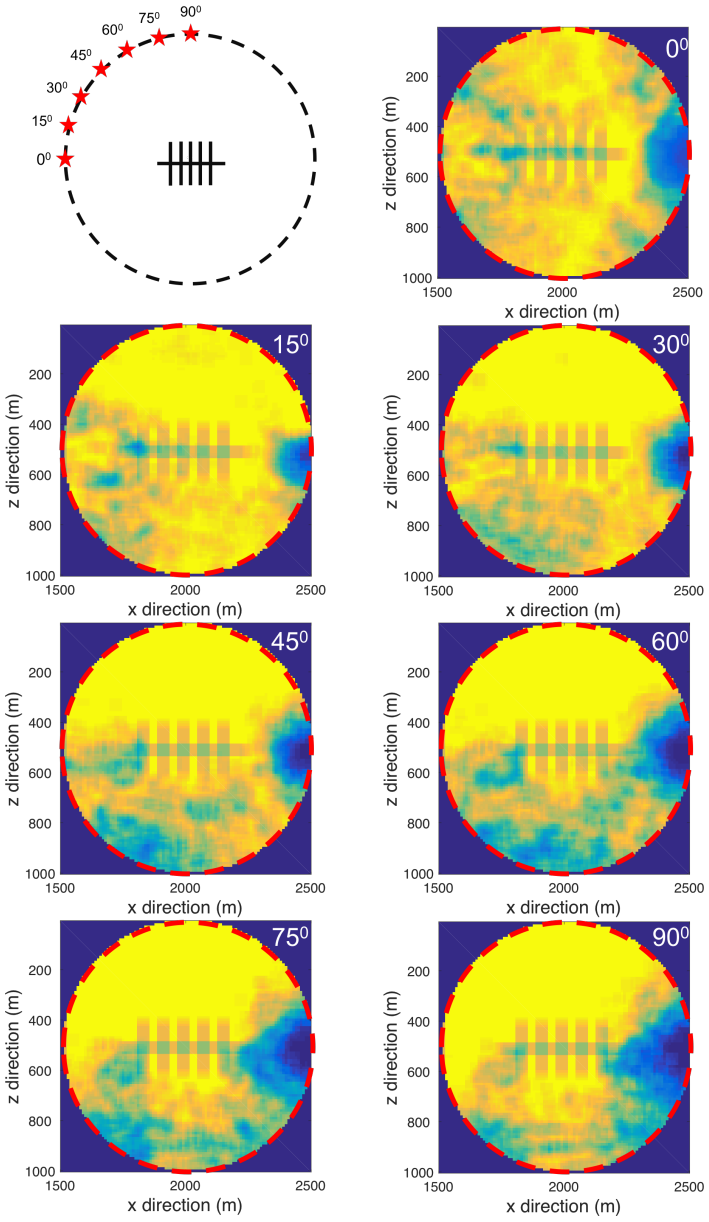

Figure 4.19: SI contour plots for multiple intersecting fractures with source-to-fracture azimuths varying from 0 to 90 degrees. The source-to-fracture azimuths are labeled on the upper right corner of each contour plot. The red circles indicate the full receiver azimuths 500m away from the center of fracture.

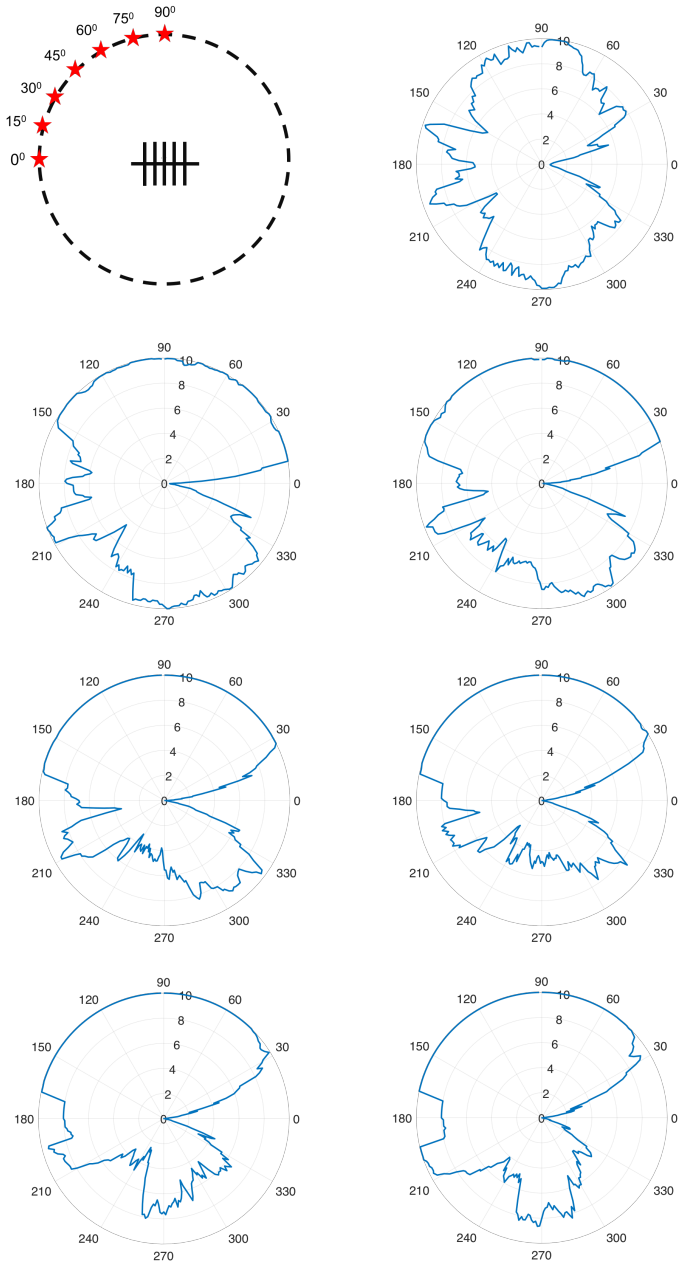

Figure 4.20: SI polar plot for multiple intersecting fractures with source-to-fracture azimuths varying from 0 to 90 degrees. The SI values are obtained from the full receiver azimuths 500m away from the center of fracture.

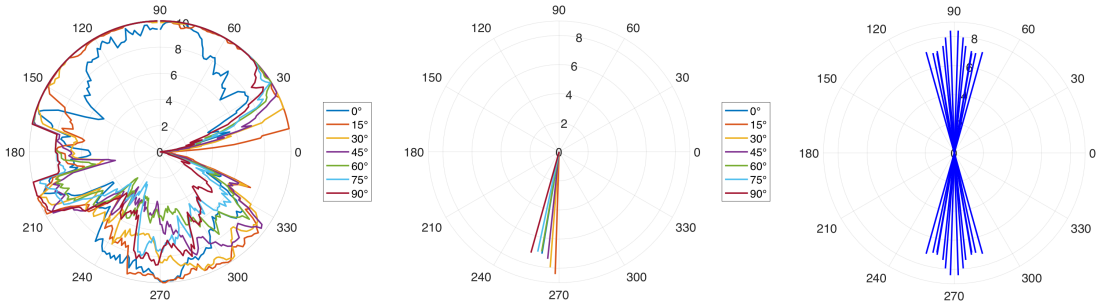

Figure 4.21: a) SI polar plot for multiple intersecting fractures from seven source-to-fracture azimuths varying from 0 to 90 degrees. b) average SI and weighted theta in a quadratic polar plot. c) average SI and weighted theta in complete source-to-fracture azimuths varying from 0 to 360 degrees.

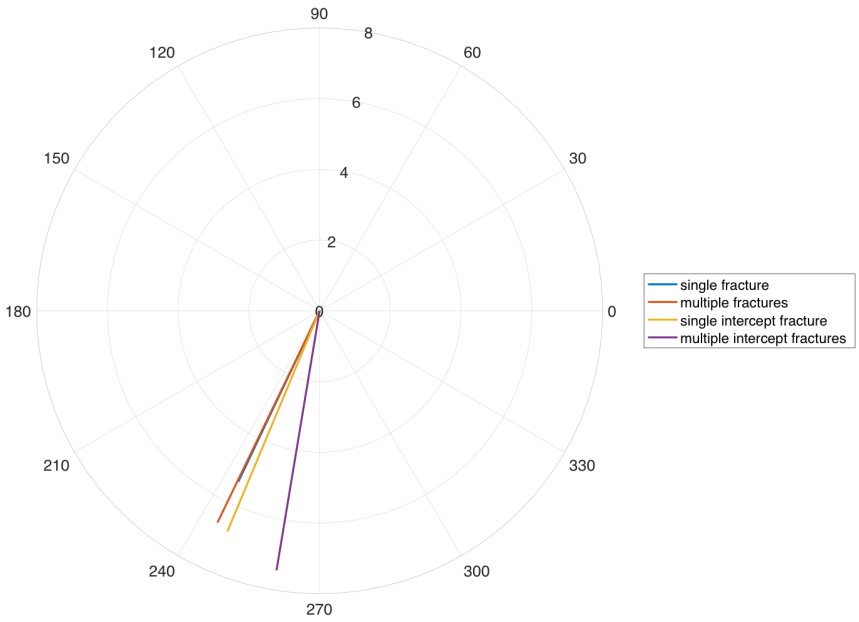

Figure 4.22: Average weighted SI and theta for a single fracture model, multiple fractures model, single intersecting fractures model, and multiple intersecting fractures model. The radius represents the value of SI. The angle represents the θ angle corresponding to the average SI.

	Theta	Scattering index
Single fracture	-2.0145	5.3482
Multiple fractures	-2.02	6.6484
Single intersecting fracture	-1.9665	6.67
Multiple intersecting fracture	-1.7353	7,4361

Table 4.1: Average weighted SI and theta for four types of fracture model: a single fracture model, multiple fractures model, single intersecting fractures model, and multiple intersecting fractures model.

4.5 Conclusions

The scattering index method has been used in this study to quantify the effect of fracture spacing on wave scattering. The mean values of the scattering index for the entire domain provide a correlation between scattering and fracture spacing over wavelength ratio. This relationship can help identify the fracture spacing when other properties of fractures are known. Using both pattern recognition and mean values of the scattering index contour plot, I should be able to characterize fracture properties in a quantified manner.

I also investigated the effect of fracture azimuth by placing an explosive source at different angles toward the center of line or intersecting fractures. The wave-field results were examined, and the scattering effect was characterized using the scattering index method. The average scattering vectors surrounding the fractured domain were computed and discussed. Finally, the total average scattering vectors for different fracture patterns were computed and compared. From the results, I found that the wave scattering is very sensitive to the fracture distribution. For the case of relatively large compliance, the scattering was mainly induced by the interference between the reflected wave and the explosive wave. As the fracture density increases, the scattering

index increases. The intersecting fracture pattern showed more scattering compared to the case of a single fracture. Multiple intersecting fractures seem to intensify such an effect. In terms of the orientation, most of the scattering vectors were close to the direction parallel to the single fracture or the maximum compliance of the fractured region.

Chapter 5

Conclusions and future studies

This dissertation aimed to solve two main issues. The first involved the exploration of a suitable numerical method to explicitly simulate fractures in 3D elastic wave propagation problems. The second issue was to investigate the relationship between fracture properties and assorted seismic signatures. Chapters 2 and 3 mainly focused on addressing the first issue. Chapter 4 focused on addressing the second issue. The results and discussions are concluded in this chapter.

The discontinuous Galerkin (DG) method implemented by De Basabe et al. (2015) was used to simulate the fracture explicitly. I examined the accuracy of the DG method by comparing numerical results with known analytical results. This method offers a direct mathematical description of the displacement continuity at the fracture surface (or boundary). In this way, high accuracy was preserved by assigning different displacement values at the duplicated nodes on fractures. The first gradient of displacement (or strain) was passed along this discontinuous boundary, which maintained the equilibrium at each node. The shape functions were also preserved in each continuous domain leaving the error term unchanged. The additional error term induced by the discontinuity was then bounded as the discontinuity occurred in terms of a step function. The DG method can also easily incorporate the linear-slip

model at the fracture location with the inherited convenience from the displacement discontinuity. However, the disadvantage lies in the relative high computation cost due to the finite element formulation. From the finite element formulation, the accuracy of the solution from the weak form is highly dependent on the mesh size in the form of power function. This means a finer mesh is usually required, which leads to a significantly large size of stiffness matrix in terms of a solver input. This hindered the computation efficiency directly. With this distinct shortcoming, it is quite challenging to conduct parametric studies on fractures in the case of 3D seismic wave propagating in elastic media.

As an alternative, I sought a solution using an integral based approach. In this approach, I no longer solve a weak form in terms of spatial integrals and corresponding discretization. Instead, I integrate the governing equation out and simplify this integrated equation with known conditions from wave equations. In this way, I essentially solve a mixed governing equation using stress based discretization methods. Based on this discretization scheme, I lose accuracy in terms of displacement within each element but preserve the accuracy in strains in the whole field. Compared to DG, the integral method may have a low convergence rate in terms of mesh sensitivity, but it requires less computational cost and provides relatively high accuracy in terms of strain and stress. Therefore, this integral based approach may be better suited to conduct parametric studies on the effect of fracture properties on elastic waves. To ensure the accuracy, validations were confirmed by comparing the results using DG, the integral-based method, and analytical solutions.

To address the second issue of correlating fracture properties with features

from wave propagation in fractured elastic media, I firstly observed the wave field results using both DG and the integral-based method. I found out the wave scattering induced by fractures is the main feature that directly ties the fracture properties to wave propagation. The results also show that the wave scattering is very sensitive to all fracture parameters including spacing, density, patterns, and azimuth. However, the specific correlation requires quantification. The scattering index method (SI) (Willis et al., 2006) was then selected to quantify this effect. This method basically evaluates the energy from the scattered wave induced by fractures. I then conducted numerical simulations with varying fracture properties and obtained the SI contours of the wavefield for different fractures. The results in Chapter 4 indicate that the fracture spacing is critical in correlating fracture properties with wave scattering due to the corresponding interference effect. More interestingly, by investigating the azimuthal effect, I observed that the most scattering occurred in a direction parallel to the direction of the maximum fracture compliance. This confirms some of the general observations by Willis et al. (2006). However, I established the correlation between both fracture density, patterns, and angles and wave scattering. These results provide the first level of estimation in characterizing fracture properties using elastic waves.

To summarize, this work implemented an integral-based method that can accurately simulate fractures explicitly in elastic media undergoing seismic wave propagation. The quantified correlation between fracture properties and wave scattering has been established using this method. The provided results lay a foundation in future development of inversion algorithms in fracture characterization. The following works are suggested for future study:

(1) The effect of fracture compliance should be studied in combination with other fracture properties.

(2) The intrinsic relationship between each fracture parameter should be investigated to identify the specific role of each parameter on wave scattering.

(3) An improved scattering index method should be developed to facilitate the above tasks.

Bibliography

Backus, G.E., 1962. Long-wave elastic anisotropy produced by horizontal layering. Journal of Geophysical Research 67, 44274440.

Carcione, J.M., Herman, G.C., and Kroode, A.P.E., 2002. Y2K Review Article Seismic modeling, Geophyscs, 67, 1304-1325.

Carcione, J. M., S. Picotti and J. E. Santos, 2012. Numerical experiments of fracture-induced velocity and attenuation anisotropy: Geophysical Journal International, 191, 11791191, doi: 10.1111/j.1365-246X.2012.05697.x

Coates, R. T., and Schoenberg, M., 1995, Finite-difference modeling of faults and fractures, Geophysics, 60, 1514-1526.

Cockburn, B., and Karniadakis, G. E., and Shu, C., 2000. The development of discontinuous Galerkin methods: Discontinuous Galerkin Methods, Lecture Notes in Computational Science and Engineering Volume 11, 2000, pp 3-50.

Crampin, S., 1981. A review of wave motion in anisotropic and cracked elastic media. Wave Motion, 3, 343-391.

Crampin, S., 1983, Shear-wave polarizations: A plea for three-component recording: 53rd Annual International Meeting, SEG, Expanded Abstracts, 425428.

Crampin, S., 1985. Evaluation of anisotropy by shear wave splitting, Geophysics, 50, 142-152.

Cruse, T. A. and Rizzo, F. J., 1968, A direct formation and numerical solution of the general transient elastodynamic problem, I : J. Math. Anal. Appl. 22, 244-259.

De Basabe, J. D., Sen, M., and Wheeler, M., 2008. The interior penalty discontinuous Galerkin method for elastic wave propagation: grid dispersion: Geophys. J. Int., 175, 83-93.

De Basabe, J. D. and M. K. Sen, 2009, New developments in the finite-element method for seismic modeling: The Leading Edge, 28(5), 562-567. doi: 10.1190/1.3124931

De Basabe, J. D. and M. K. Sen, 2010. Stability of the high-order finite elements for acoustic or elastic wave propagation with high-order time stepping: Geophys. J. Int. 181, 577590 doi: 10.1111/j.1365-246X.2010.04536.x

De Basabe, J. D., Sen, M., and Wheeler, M., 2011. Seismic Wave Propagation in Fractured Media: a discontinuous Galerkin approach: SEG Technical Program Expanded Abstracts 2011: pp. 2920-2924. doi: 10.1190/1.3627801

De Basabe, J. D., M. K. Sen, and M. Wheeler, 2016. Elastic wave propagation in fractured media using the discontinuous Galerkin method: Geophysics, 81(4), T163-T174. doi: 10.1190/geo2015-0602.1

Fang, X., Fehler, M. C., Zhu, Z., Zheng, Y., and Burns, D. R., 2014. Reservoir fracture characterization from siemsic scattered waves: Geophysical

Journal International. doi: 10.1093/gji/ggt381.

Grechka, V. and I. Tsvankin, 1998. Feasibility of nonhyperbolic moveout inversion in transversely isotropic media. Geophysics, 63, 957-969.

Grechka,V. and Tsvankin, I., 1999. 3D moveout inversion in azimuthally anisotropic media with lateral velocity variation, Theory and a case study. Geophysics 64, 12021218.

Hall, S.A. and Kendall, J.M., 2003. Fracture characterization at Vahall, Application of P-wave amplitude variations with offset and azimuth (AVOA) analysis to a 3D ocean-bottom dataset: Geophysics 68, 11501160.

Haugen, G. U., and M. Schoenberg, 2000. The echo of a fault or fracture: Geophysics, 65, 176189.

Holmes, G. and Thomsen, L., 2002. Seismic fracture detection at a Middle East offshore carbonate field. SPE 78507.

Hudson, J.A., 1980. Overall properties of a cracked solid. Mathematical Proceedings of the Cambridge Philosophical Society 88, 371384.

Hudson, J.A., 1981. Wave speeds and attenuation of elastic waves in material containing cracks, Geophysical Journal of Royal Astronomical Society 64, 133150.

Li, X. -Y. 1999. Fracture detection using azimuthal variation of P-wave moveout from orthogonal seismic survey lines. Geophysics, 64, 1193-1201.

Liu, E., Hudson, J. A. and Pointer, T., 2000, Equivalent medium representation of fractured rock. J. Geophysical Research, 105, No.B2, 2981-3000.

Liu, H., M. Sen and K. Spikes, 2016. Numerical modeling of seismic-wave propagation through fractures with nonuniform height and densityin 3d: SEG Technical Program Expanded Abstracts 2016: pp. 3876-3880. doi: 10.1190/segam2016-13961971.1

Liu, H., M. K. Sen, K. T. Spikes, 2017. 3D simulation of seismic wave propagation in fractured media using an integral method accommodating irregular geometries. Geophysics, submitted.

Lysmer, J. and Drake, L.A., 1972. A finite element method for seismology, Methods Computat. Phys., 11, Academic Press, New York.

Mavko, G., Mukerji, T., and J. Dvorkin, 2009, The rock physics handbook: Cambridge University Press.

Mancosu, P., 1999. Philosophy of mathematics and mathematical practice in the seventeenth century, Oxford University Press.

Rao, Y. and Wang Y., 2009, Fracture effects in seismic attenuation images reconstructed by waveform tomography. Geophysics, 74, R25 - R34, ISSN: 0016-8033.

Ruger, A., 1997. P-wave reflection coefficients for transversely isotropic models with vertical and horizontal axis of symmetry. Geophysics 62, 713722.

Ruger, A., 2002. Reflection coefficients and azimuthal AVO analysis in anisotropic media. Geophysical Monograph Series Number 10, SEG Publication.

Saenger, E.H. and Bohlen T. 2004. Finite-difference modeling of viscoelastic and anisotropic wave propagation using the rotated staggered grid.

Geophysics 69, 583591.

Saenger, E.H., and Shapiro, S.A., 2002. Effective velocities in fractured media: a numerical study using the rotated staggered finite-difference grid, Geophysical Prospecting, 50, 183-194.

Sayers, C.M., A. D. Taleghani and J. Adachi, 2009. The effect of mineralization on the ratio of normal to tangential compliance of fractures, Geophys. Prospect., 57, 439446.

Schoenberg, M., 1980. Elastic wave behaviour across linear slip interfaces. Journal of Acoustical Society of America 68, 15161521.

Schoenberg, M. and J. Douma, 1988. Elastic wave propagation in media with parallel fractures and aligned cracks: Geophysical prospecting, Volume 36, Issue 6, Pages 571590. DOI: 10.1111/j.1365-2478.1988.tb02181.x.

Schoenberg, M. and Muir, F., 1989. A calculus for finely layered anisotropic media. Geophys., 54, 581-589.

Schoenberg, M. and C. Sayers, 1995. Seismic anisotropy of fractured rock. Geophysics, 60, 204-211.

Sheriff, R.E., 2002. Encyclopaedic Dictionary of Exploration Geophysics. SEG Books, Tulsa, Oklahoma.

Shuey, R.T., 1985. A simplification of the Zoeppritz equations. Geophysics 50, 609614.

Singh, Sunil K., Hanan Abu-Habbiel, Badruzzaman Khan, Mahmood Akbar,

Arnaud Etchecopar and Bernard Montaron, 2008. Mapping fracture corridors in naturally fractured reservoirs: an example from Middle East carbonates. First Break, 26, 109-113.

Slawinski, R. A., and E. S. Krebes, 2002. Finite-difference modeling of SH-wave propagation in nonwelded contact media: Geophysics, 67, 16561663.

Thomsen, L., 1986. Weak elastic anisotropy. Geophysics 51, 19541966.

Thomsen, L., 1995. Elastic anisotropy due to aligned cracks in porous rock. Geophysical Prospecting 43, 805829.

Tsvankin et al., 2010, Seismic anisotropy in exploration and reservoir characterization: An overview: Geophysics, 75 , A15-A29.

Tromp, J., D. Komatitsch and Q. Liu, 2008. Spectral-Element and Adjoint Methods in Seismology. COMMUNICATIONS IN COMPUTATIONAL PHYSICS, 3(1), 32.

Varela, I., S. Maultzsch, and X.-Y. Li. 2007. Fracture properties inversion from azimuthal AVO using singular value decomposition. Seg 77th Conference & Exhibition, 26, 259-263

Virieux, J., 1986. P-SV wave propagation in heterogeneous media: Velocity-stress finite-difference method. Geophysics, 51, 889901.

Vlastos, S., 2005. Seismic characterisation of fluid flow in fractured reservoirs. PhD thesis, University of Edinburgh.

Vlastos, S., Liu E.,Main I.G. and Li X.Y. 2003. Numerical simulation of wave propagation in media with discrete distribution of fractures: effects of

fracture sizes and spatial distributions. Geophysical Prospecting, 152, 649668.

Wang, S.X. and Li, X.Y, 2006. Layer stripping of azimuthal anisotropy from P-wave reflection moveout in orthogonal survey lines. Journal of Geophysics & Engineering 3, 111.

Willis, M. E., D. Burns, R. Rao, B. Minsley, M. N. Toksöz, and L. Vetri, 2006. Spatial orientation and distribution of reservoir fractures from scattered seismic energy: Geophysics, VOL. 71, NO. 5. doi: 10.1190/1.2235977

Winterstein, D.W., 1990. Velocity anisotropy terminology for geophysicists. Geophysics 55, 10701088.

Xia, G., L. Thomsen and O. Barkved, 2006. Fracture Detection from Seismic P-wave azimuthal AVO analysis application to Valhall LoFS data: International Symposium on In-Situ Rock Stress, DOI: 10.1201/9781439833650.ch64

Xu, Y., 2011. Analysis of P-wave seismic response for fracture detection: modeling and case studies: Ph.D. Dissertation. The University of Edinburgh.

Zhang, J., and H. Gao, 2009. Elastic wave modeling in 3-D fractured medium: an explicit approach. Geophys. J. Int. 177, 1233-1241. doi: 10.1111/j.1365-246X.2009.04151.x

Zhu, Y., and R. Snieder, 2003. Simulation of waves in fractured media using an extrapolation scheme: 73rd Annual InternationalMeeting, SEG, Expanded Abstracts, 18451848.

Vita

Han Liu was born in China. She obtained the degrees of Bachelor of Science in Geophysics from China University of Petroleum and Missouri University of Science and Technology in 2012. Later in the same year, she came to Austin, TX to pursue the degree of Doctor of Philosophy in Geophysics at The University of Texas at Austin.

Email:hliu198902@gmail.com

This dissertation was typeset with LaTeX[†] by the author.

[†]LaTeX is a document preparation system developed by Leslie Lamport as a special version of Donald Knuth's TeX Program.